

Critical Heat Flux

RELAP5/MOD2 has been criticized for using the Biasi correlation^(4-6,4-7) for predicting the CHF in rod bundles because the correlation is based on tube data. MOD3 uses the 1986 AECL-UO Critical Heat Flux Lookup Table⁽⁴⁻⁸⁾ method by Groeneveld and co-workers. The table is made from tube data normalized to a tube inside diameter of 0.008 m but has factors that are applied to allow its use in other sized tubes or in rod bundles. In addition, it considers both forward and reverse flow, axial power shape, and the effect of boundary layer changes at both the bundle inlet and downstream of grid spacers. The root-mean-squared error at low pressure is generally below 20%. Its accuracy for rod bundles is uncertain.

Minimum Stable Film Boiling Point

The other point which is fixed on the boiling curve is the minimum film boiling point, T_{\min} . In RELAP5 a constant T_{\min} equal to 600 K (620 F) is used.

Transition Boiling

The Chen transition boiling model⁽⁴⁻⁹⁾ considers the total transition boiling heat transfer to be the sum of two individual components, one describing wall heat transfer to the liquid and a second describing the wall heat transfer to the vapor. Radiative heat transfer from the wall to the fluid is neglected. The model was compared to data (4167 points) with a standard deviation of 16%. The calculated heat flux value for transition boiling is applied to post-CHF heat transfer if it is larger than the value for film boiling.

Film Boiling

Film boiling heat transfer is calculated with the Bromley correlation⁽⁴⁻¹⁰⁾. The data were correlated within $\pm 18\%$. In this case a radiation heat transfer model is included to calculate the radiation heat transfer from the wall to the fluid. This model is attributed to Sun⁽⁴⁻¹¹⁾.

Interfacial Heat Transfer

The flow regime determines the bulk interfacial heat transfer correlation to be used. For each vertical flow regime (bubbly, slug, annular-mist, inverted annular, inverted slug and dispersed) a correlation is used to calculate the interfacial volumetric heat transfer coefficient for either superheated liquid, subcooled liquid, superheated gas or subcooled gas. These are generally semi-empirical and/or mechanistic models which have been modified from the original model in the literature^(4-12 - 4-17) to account for numerical stability concerns. The interfacial heat transfer is the product of the interfacial area based on the flow regime and the interfacial heat transfer coefficient.

For each flow regime the interfacial heat transfer coefficient is split into superheated-liquid (SHL), subcooled-liquid (SCL), superheated-gas (SHG) and subcooled-gas (SCG). In the code

metastable states are generally driven rapidly to equilibrium by large empirical exponential functions. A summary of the interfacial areas and heat transfer coefficients is reported in Table 4-2 while the original interfacial heat transfer models are reported in References 4-12 to 4-17.

Quench Front Model

Besides the heat transfer to the fluid another important process during reflood transients is the rod axial conduction at the quench front. The rod axial conduction is considered in RELAP5/MOD3 by a specific reflood heat conduction model which is based on a mesh-rezoning scheme very similar to the one used in COBRA-TF.

Liquid Entrainment

The liquid droplet entrainment process is considered to occur only in the annular-mist flow regime where the Ishii and Mishima^(4-18, 4-19) correlation is used to determine the fraction of liquid flux flowing as droplets. The model gives very accurate results at location where annular mist flow regime existed.

4.2.1.3 Conclusions

The heat transfer correlations are used to provide closure for the energy equations and are based on data which reflects only a subset of thermal-hydraulic conditions. Such correlations are very often applied outside their database. Moreover some of the correlations are based on engineering judgment, due partly to incompleteness of the science and partly to numerical stability requirements. From this perspective, by treating each correlation individually, the critical reviewer will conclude that the models are inadequate. In this case it is recognized that only an integral assessment is realistic where the global response of the code rather than the local response, becomes more meaningful.

For example, the correlation used to calculate the volumetric interfacial heat transfer coefficient in the annular mist flow between the liquid annular film and the gas core is based on the work of Brumfield et al.⁽⁴⁻¹²⁾. This was based on a falling liquid film surrounded by quiescent air, whereas annular-mist involves a turbulent, flowing vapor core. The correlation is also based on the liquid velocity.

The liquid velocity in the code is a single bulk value representing an average of both liquid annular film and the liquid droplets in the vapor core. As such, it is possible for the liquid velocity to be zero when the mass flow of droplets in one direction is balanced by the annular-film flow in the opposite direction. In such case, the code would incorrectly predict zero for the interfacial heat transfer coefficient.

Another example of application of engineering judgment is the calculation of the droplet size in the inverted slug flow and dispersed flow regimes. The characteristic droplet size is calculated by assuming a critical We number equal to 6.0 and bounded by a minimum value

Table 4-2 Summary of interfacial areas and heat transfer coefficients^a.

Flow Type	a_{gf}	$h_{if,SHL}$	$h_{if,SCL}$	$h_{ig,SHG}$	$h_{ig,SCG}$
Bubbly	$\frac{3.6\alpha_{bub}}{d_b}$	Lee-Ryley ^M Plesset-Zwick	Unal ^M	$10^4 f(\Delta T_{sg})$	$10^4 f(\Delta T_{sg})$
Slug:					
Bubbles	$\frac{3.6\alpha_{gs}(1-\alpha_{TB})}{d_b}$	Lee-Ryley ^M Plesset-Zwick	Unal ^M	$10^4 f(\Delta T_{sg})$	$10^4 f(\Delta T_{sg})$
Taylor bubble	$\frac{4.5}{D}\alpha_{Tb}(2.0)$	$3 \times 10^6 f(\Delta T_{sf})$	Sieder-Tate ^M	Lee-Ryley ^M	$10^4 f(\Delta T_{sg})$
Annular mist:					
Drops	$\frac{3.6\alpha_{fd}(1-\alpha_{ff})}{d_d}$	$\frac{k_{ff}}{d_d} f(\Delta T_{sf})$	Brown ^M $xf(\Delta T_{sf})$	Lee-Ryley ^M	$10^4 f(\Delta T_{sg})$
Liquid film	$\frac{4}{D}(1-\alpha_{ff})^{1/2}(2.5)$	3×10^6	Theofanous ^M	Dittus-Boelter ^M	$10^4 f(\Delta T_{sg})$
Inverted annular:					
Bubbles	$\frac{3.6\alpha_{bub}}{d_b}(1-\alpha_B)$	Lee-Ryley ^M Plesset-Zwick	Unal ^M	$10^4 f(\Delta T_{sg})$	$10^4 f(\Delta T_{sg})$
Vapor film	$\frac{4}{D}(1-\alpha_B)^{1/2}(2.5)$	3×10^6	Dittus-Boelter ^M	$\frac{k_{gf}}{D} f(\Delta T_{sg})$	$\frac{k_{gf}}{D} f(\Delta T_{sg})$
Inverted slug:					
Drops	$\frac{3.6\alpha_{dtp}(1-\alpha_B)}{d_d}$	$\frac{k_{ff}}{D} f(\Delta T_{sf})$	Brown ^M $xf(\Delta T_{sf})$	Lee-Ryley ^M	Lee-Ryley ^M
Taylor drop	$\frac{4.5}{D}(\alpha_B)(2.5)$	$\frac{k_{ff}}{D} f(\Delta T_{sf})$	Brown ^M $xf(\Delta T_{sf})$	$\frac{k_{gf}}{D} f(\Delta T_{sg})$	$\frac{k_{gf}}{D} f(\Delta T_{sg})$
Dispersed (droplet, mist)	$\frac{3.6\alpha_{dtp}}{d_d}$	$\frac{k_{ff}}{D} f(\Delta T_{sf})$	Brown ^M $xf(\Delta T_{sf})$	Lee-Ryley ^M $xf(\Delta T_{sg})$	$10^4 f(\Delta T_{sg})$
Horizontal stratified	$\frac{4 \sin \theta}{\pi D}$	Dittus-Boelter $xf(\Delta T_{sf})$	Dittus-Boelter	Dittus-Boelter $10^4 f(\Delta T_{sg})$	$10^4 f(\Delta T_{sg})$
Vertical stratified	$\frac{A_c}{V}$	$h_{if,REG}$	McAdams	McAdams	$h_{ig,REG}$

a. SCL = subcooled liquid; SHL = superheated liquid; SHG = superheated gas; SCG = subcooled gas; M = modified; $f(\Delta T_{sg})$ = function of $\Delta T_{sg} = T^s - T_g$; $f(\Delta T_{sf})$ = function of $\Delta T_{sf} = T^s - T_f$; REG = flow regime when not vertically stratified.

for droplet diameter of 2.5 mm at low pressure, to allow more steam superheat during reflood. This is inconsistent with what observed during FLECHT-SEASET experiments where the Santer mean diameter was estimated to be close to 1.0 mm.

A deficiency in RELAP5/MOD3 when compared to COBRA-TF is that there are not specific models to calculate the entrainment and/or deentrainment at spacer grids. In addition, entrainment and deentrainment is only calculated for annular flow or horizontal stratified flows.

Concerning the RELAP5/MOD3 capabilities to simulate accurately the phenomena involved in reflood transient, a big disadvantage is certainly the two field scheme where a single bulk value represents both the liquid in the continuous phase and droplets.

4.2.2 TRAC BF1 Reflood Model

4.2.2.1 Introduction

The TRAC-BF1 model was developed specifically for Boiling Water Reactors and its development followed the development of the TRAC-PD2 PWR model. The heat transfer models are somewhat more simplified as compared to TRAC-PF1, however, a specific CHAN (channel) component was added to allow more accurate modeling of the BWR fuel channel during a LOCA. Surface-to-surface radiation heat transfer models were added with the CHAN component to calculate the radiation heat transfer expected in the canned assembly for LOCA conditions.

Quench Front Model

TRAC-BF1 uses a fine mesh renodalization model for modeling quench fronts. The fine mesh model inserts additional nodes into the heated wall if significant temperature gradients exist along the wall. In the case of reflood modeling, the use of the fine mesh option allows one to capture the rapid changes in temperature along a fuel rod due to the presence of the quench front. It increases both the accuracy and the robustness of the code. No special heat transfer model is employed in TRAC-BF1 to model the quench front. Instead, both the heat transfer and flow regime map used in all other wall heat transfer calculations is employed.

Fine-Mesh Algorithm

To model the advancing quench front, a numerical technique is employed which allows additional mesh points to be introduced within a region around the quench front. The method allows the resolution of the high thermal gradients encountered near a quench front. The use of the fine mesh allows a more accurate representation of the heat transfer and energy content of the wall. The fine mesh heat transfer nodalization is superimposed on the coarse mesh usually used for the heat transfer analysis. Rows of transitory nodes are inserted whenever the temperature difference, ΔT_{\max} , between adjacent nodes exceeds a user specified value. The number of nodes inserted is also user specified and remain during the entire reflood phase and move with the front. Multiple quench fronts may be modeled.

The model uses two values of ΔT_{\max} , one for the quenching region that is in nucleate or transition boiling and the other to all other heat transfer regimes. The largest wall heat transfer occurs in the former regions.

4.2.3 TRAC PF1 Reflood Model

4.2.3.1 Introduction

The TRAC-PF1 code series is the oldest best-estimate thermal-hydraulic codes developed for safety analysis purposes. The code formulation and interfacial heat, mass and momentum models has had several improvements over the years as the code has been used in a number of applications. TRAC-PF1 models the two-phase flow with two fields, liquid and vapor with three-dimensional capability within the vessel component. The coordinate systems used for the code are cylindrical such that the core region is modeled as a series of connected pie wedges. Specific models used in the code will be discussed below for this version of the code. A more recent version of the code, TRAC-PF1/MOD2 has a new reflood model. A brief review of this code will be added to this section at a later date.

Quench Front Model

TRAC-PF1 uses both fine mesh renodalization and a special heat transfer model for modeling quench fronts. The fine mesh model inserts additional nodes into the heated wall if significant axial temperature gradients exist along the wall. In the case of reflood modeling, the use of the fine mesh option allows one to capture the rapid changes in temperature along a fuel rod due to the presence of the quench front. It increases both the accuracy and the robustness of the code. The heat transfer model in MOD2 is based on Ishii and uses a special flow regime map which inserts additional regimes near the CHF point.

Fine-Mesh Algorithm

To model the advancing quench front, a numerical technique is employed which allows additional mesh points to be introduced within a region around the quench front. The method allows the resolution of the high thermal gradients encountered near a quench front. The use of the fine mesh allows a more accurate representation of the heat transfer and energy content of the wall. The fine mesh heat transfer nodalization is superimposed on the coarse mesh usually used for the heat transfer analysis. Rows of transitory nodes are inserted whenever the temperature difference, ΔT_{\max} , between adjacent nodes exceeds a user specified value. The number of nodes inserted is also user specified and remain during the entire reflood phase and move with the front. Multiple quench fronts may be modeled.

The model uses two values of ΔT_{\max} , one for the quenching region that is in nucleate or transition boiling and the other to all other heat transfer regimes. The largest wall heat transfer occurs in the former regions.

Heat Transfer Model During Reflood

The model for calculating the heat transfer in TRAC-PF1 is based on the void-fraction wall-superheat plane shown in Figure 4-3, and consists of eight different heat transfer regimes, which are listed in Table 4-3. The primary basis for correlation selection in TRAC-PF1 are the void fraction and wall superheat. While some pressure dependence enters the correlations through the properties of the parameters used in the calculations, the choice of correlation for any one particular regime is not based primarily on pressure criteria. The same is true for phasic temperatures and phasic velocities, which are introduced into the correlations through the heat flux equations and the flow correlations, respectively. To avoid any discontinuities in the heat flux, the current version of TRAC-PF1 (MOD 2) evaluates the heat transfer coefficient for both laminar and turbulent natural convection, as well as forced convection, then chooses the maximum value of the heat transfer coefficient to use in calculations.

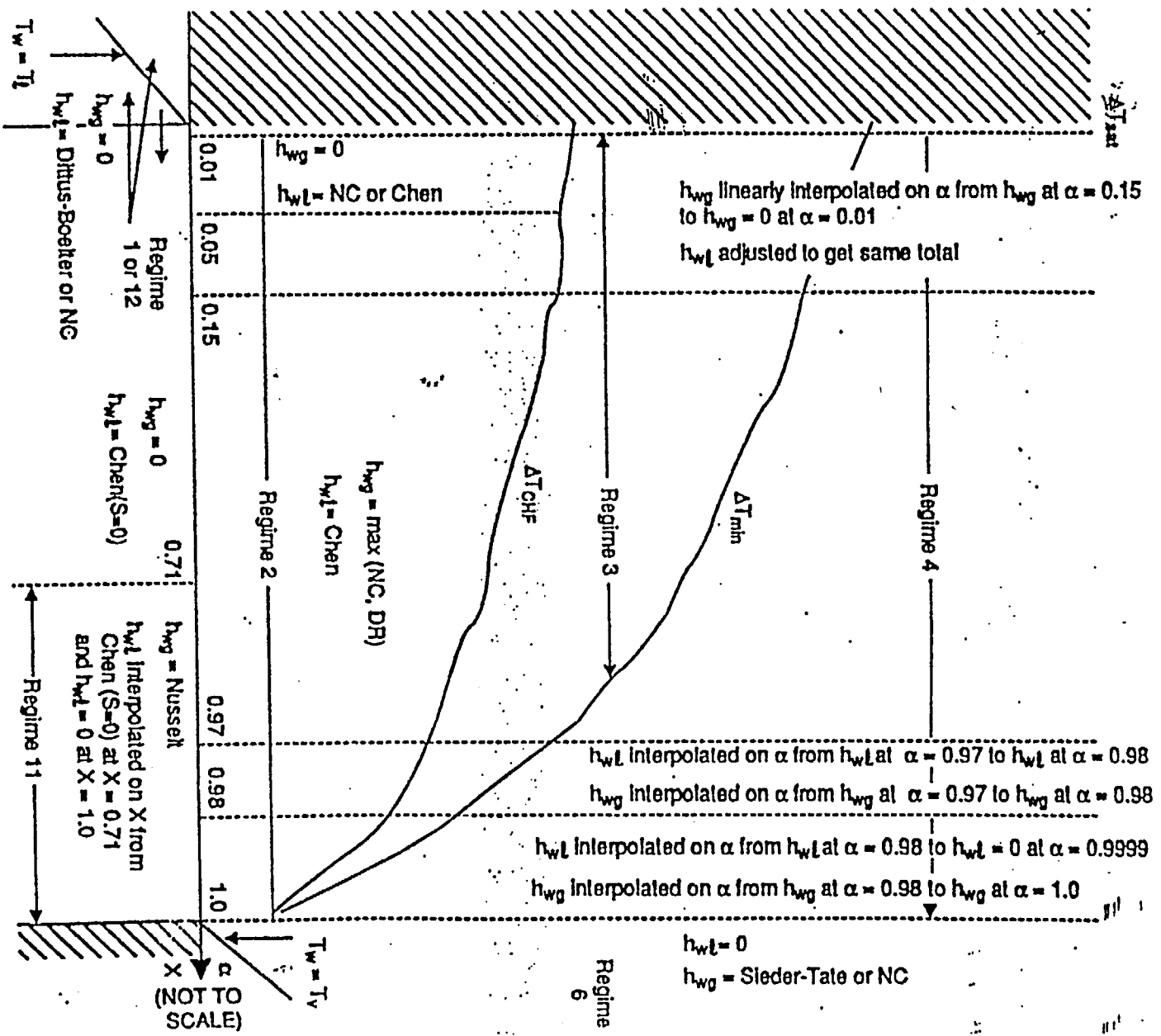


Figure 4-3 Void-fraction superheat plane.

Table 4-3: TRAC-PF1/MOD2 Heat-Transfer Regimes⁴⁻²⁰

Mode	Wall-to-Fluid Heat-Transfer Regime
1	Forced Convection to Single-Phase Liquid
2	Nucleate Boiling
3	Transition Boiling
4	Film Boiling
6	Convection to Single-Phase Vapor
7	Convection to Two-Phase Mixture
11	Condensation
12	Liquid Natural Convection

In each of the heat transfer regimes, the heat transfer coefficients are calculated in the subroutines HTCOR and HTVSSL. HTVSSL is used during reflood. The correlations used in HTVSSL are summarized here in detail. With the exception of the film boiling regime and the transition boiling regime, many of the correlations used in HTVSSL are the same as HTCOR. The post-CHF flow-regimes in HTVSSL are based on the more recent work done by Ishii, which showed that there are four inverted annular flow regimes downstream of the transition boiling regime, as shown in Figure 4-4. The selection logic for HTVSSL is shown in detail in Figures 4-5 through 4-11.

During reflood, TRAC-PF1 employs a special flow-regime map based on the flow-regimes depicted in Figure 4-4. According to Ishii, along the flow channel, various flow regimes occur beyond the point of CHF. These different flow regimes are characterized by different heat transfer conditions requiring different closure relations. The different closure relations are applied depending upon the location of the flow regime within the cell. A weighting factor is applied based on the cell length and the elevation within the cell at which the regime occurs. Table 4-4 shows how the weighting factors are calculated.

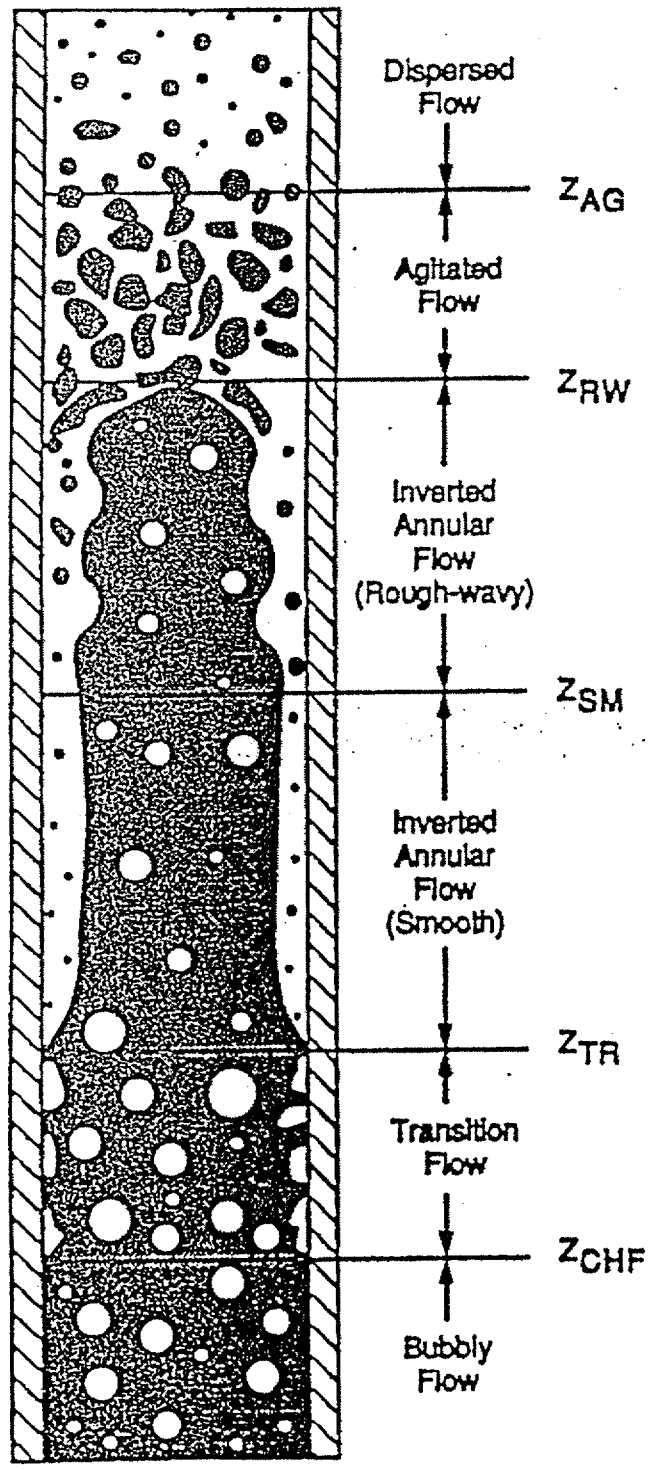


Figure 4-4 Flow-regime map during reflood.

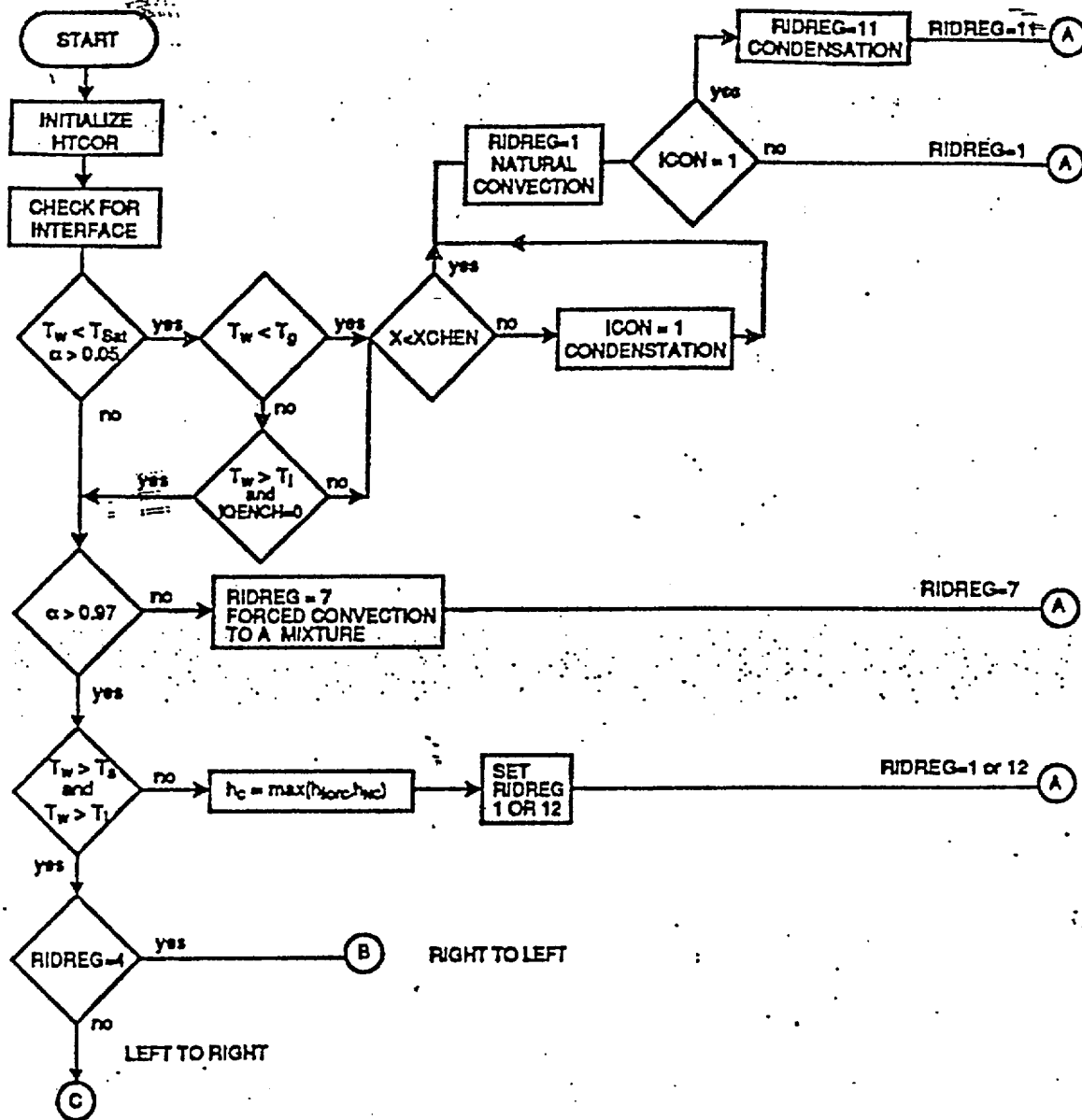
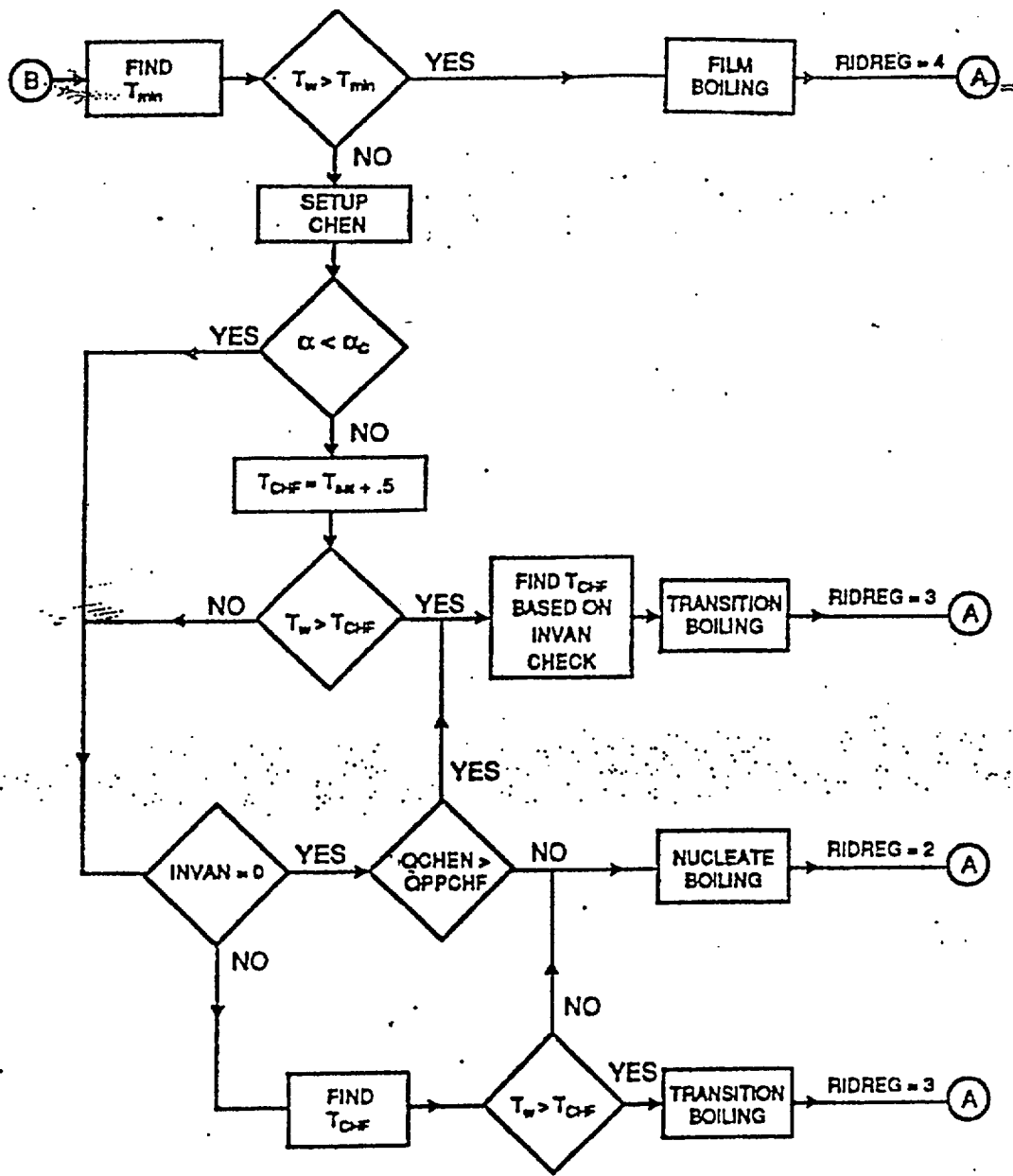
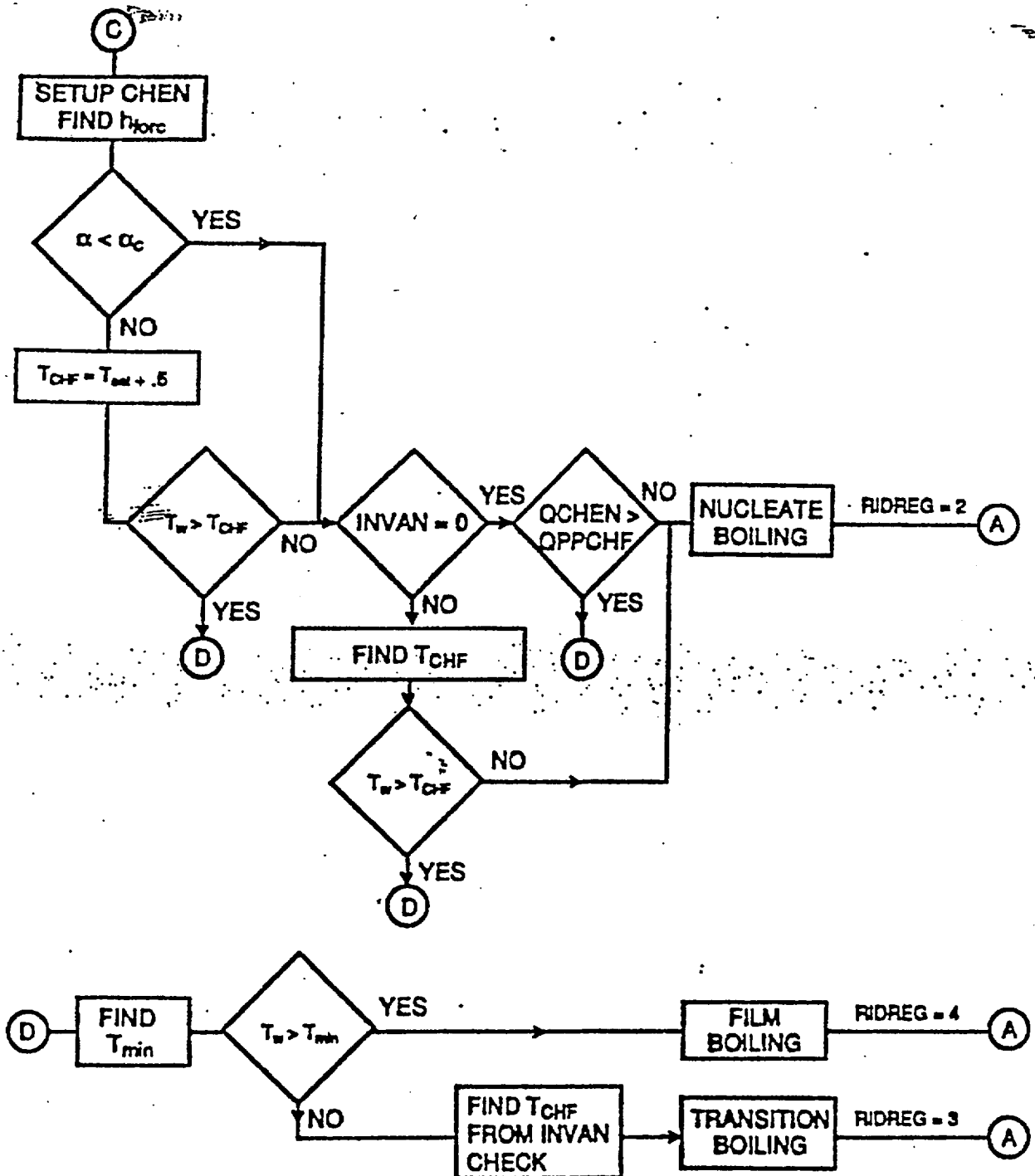


Figure 4-5 HTC correlation selection logic.



RIGHT TO LEFT ON BOILING CURVE

Figure 4-6 HTC correlation selection logic.



LEFT TO RIGHT ON BOILING CURVE

Figure 4-7 HTC correlation selection logic.

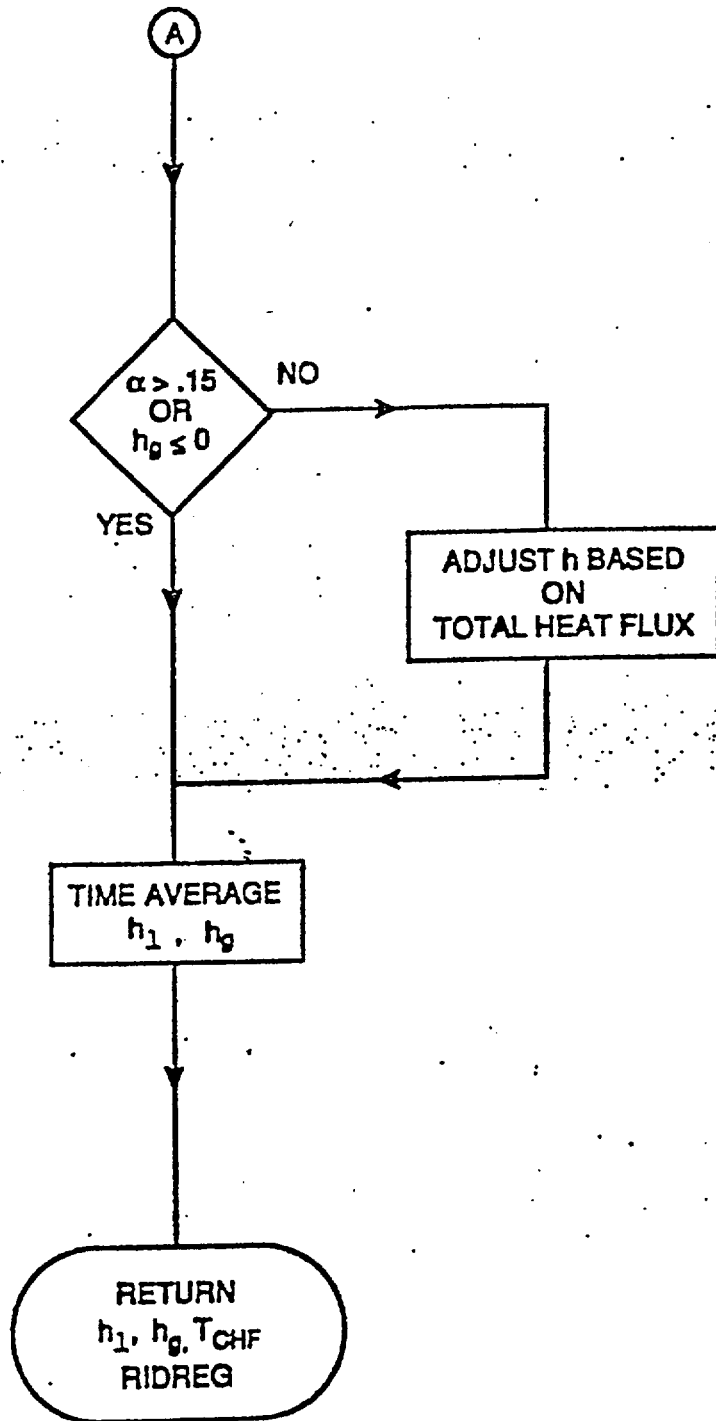


Figure 4-8 HTC correlation selection logic.

LEFT TO RIGHT ON BOILING CURVE

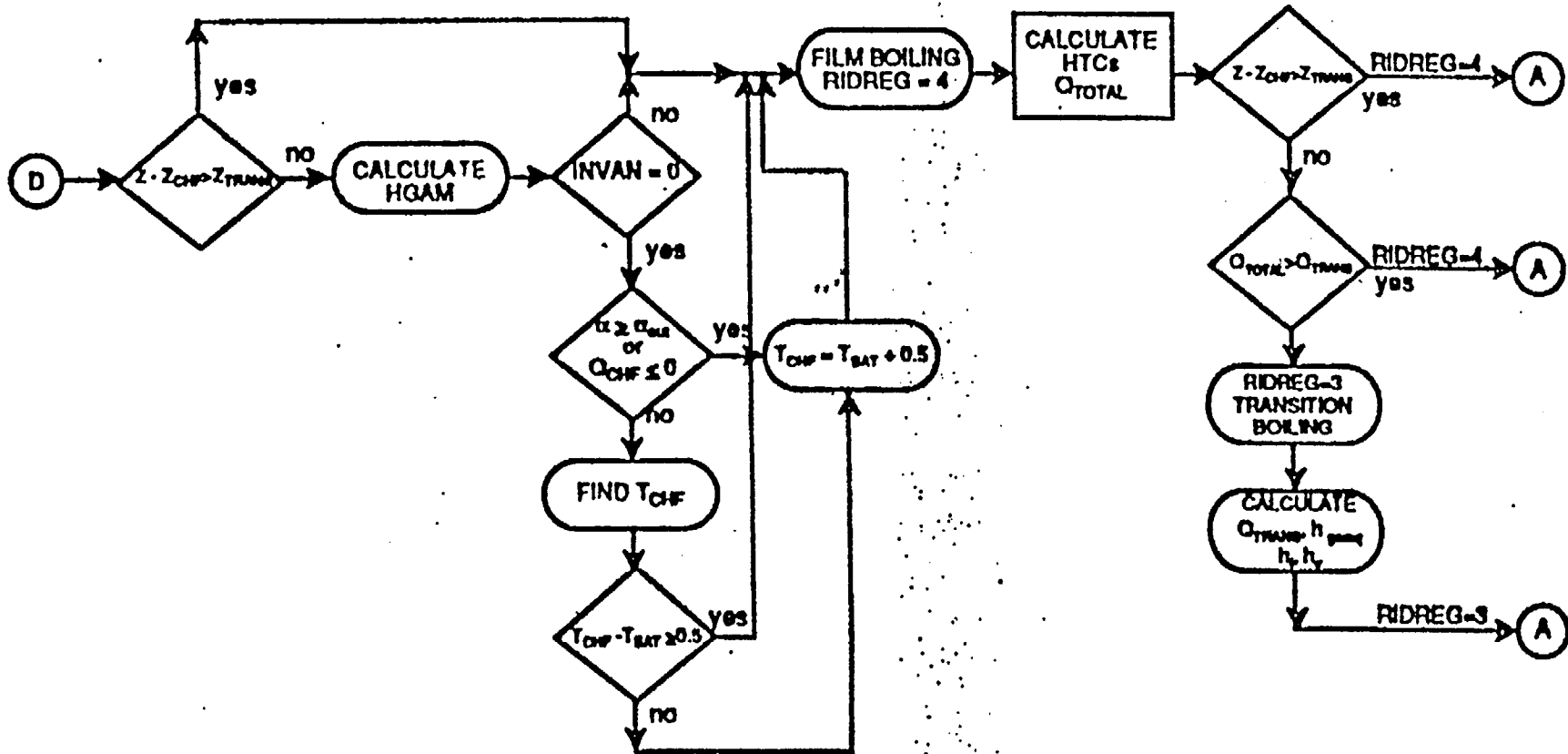


Figure 4-9 HTC correlation selection logic for reflow model.

RIGHT TO LEFT BOILING CURVE
(Page 1)

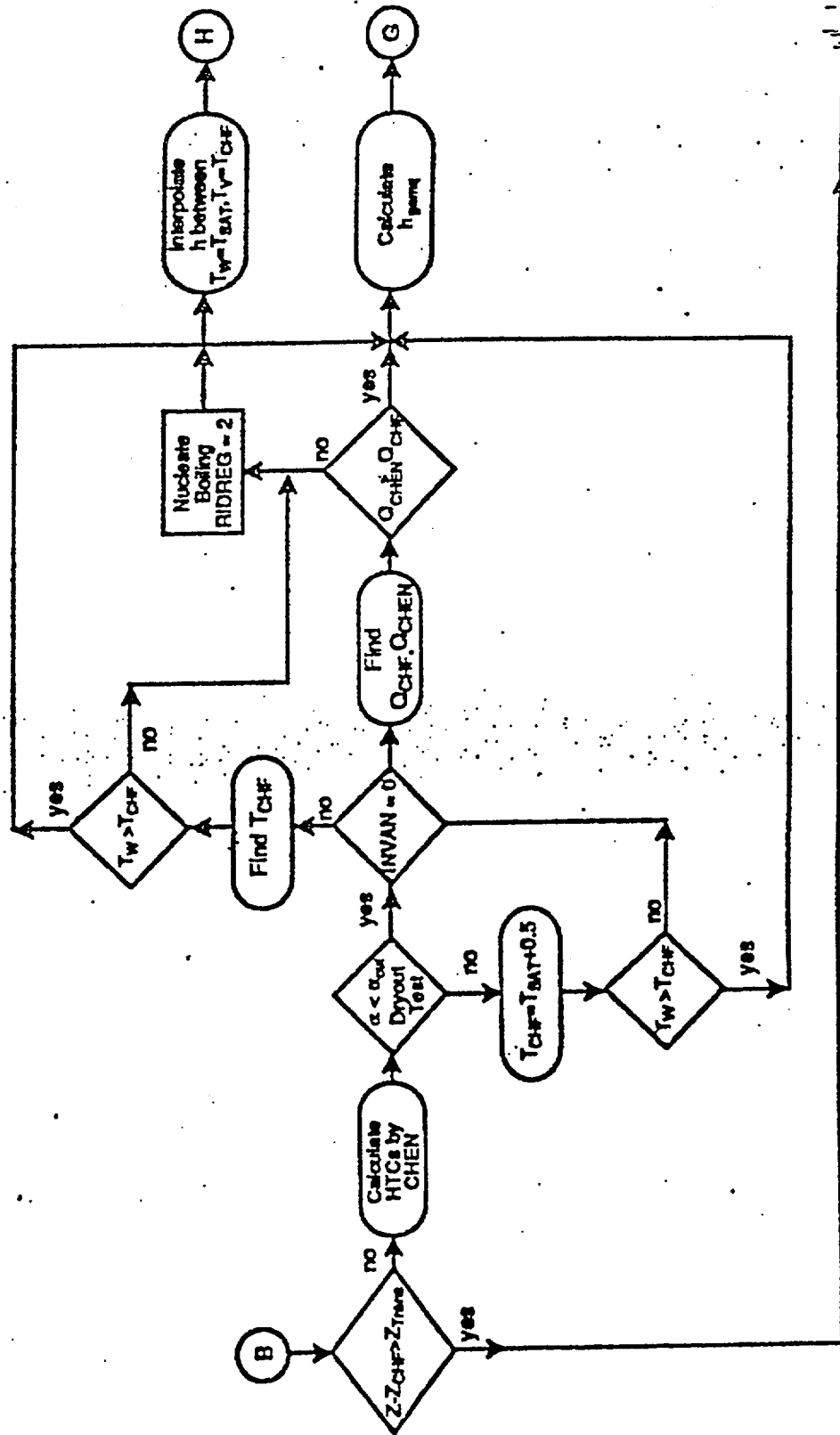


Figure 4-10 HTC correlation selection logic for reflow model.

RIGHT TO LEFT BOLING CURVE
(Page 2)

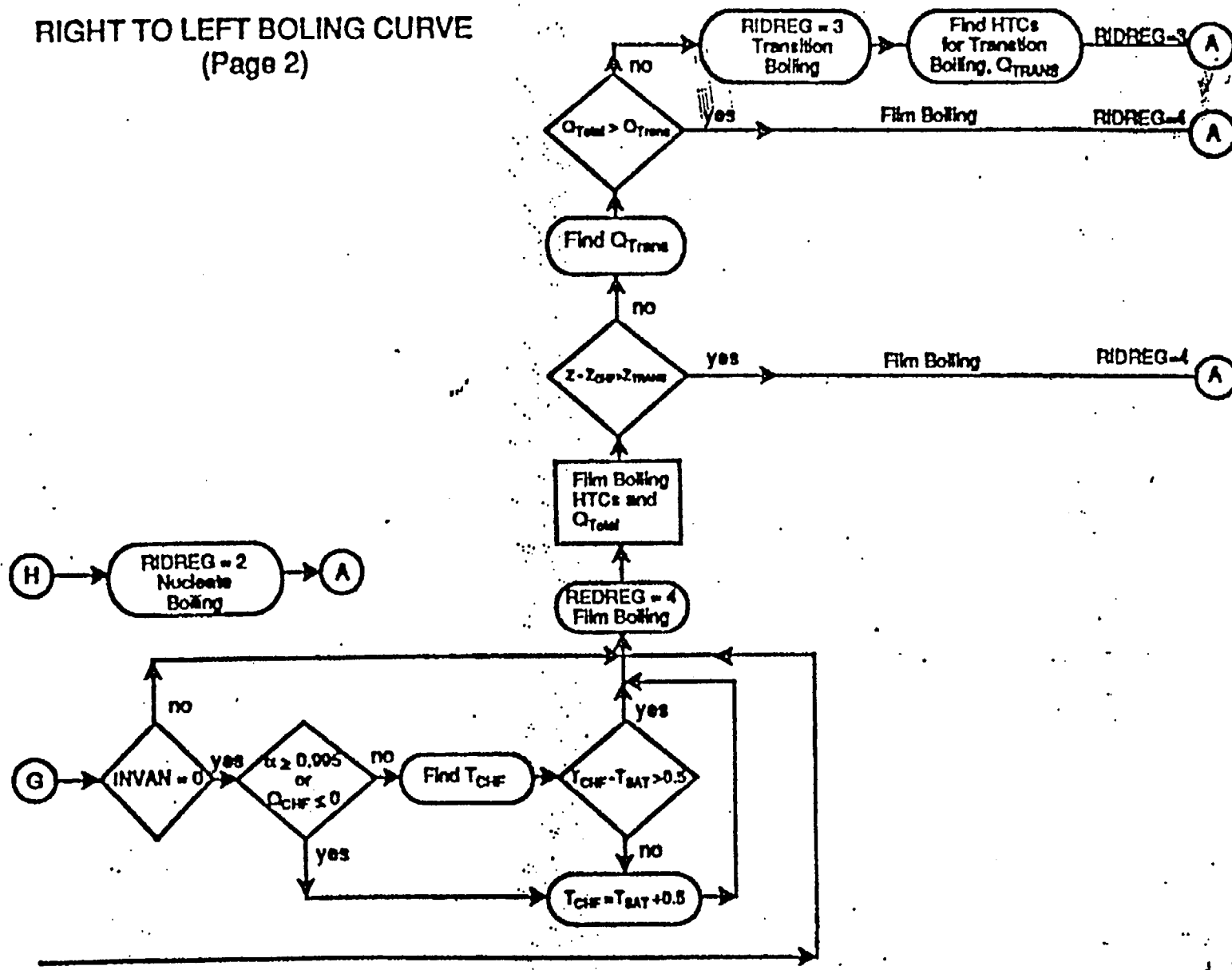


Figure 4-11 HTC correlation selection logic for rehood model.

Table 4-4. Weighting Factors of Reflood Interfacial Heat-Transfer Models

z	W_{sb}	W_{sm}	W_{rw}	W_{ds}	W_{inv}
—					
$z_t \leq Z_{TR}$	1	0	0	0	0
$Z_{TR} < z_t < Z_{SM}$	Eq. (4 - 102)	Eq. (4 - 103)	0	0	Eq. (4 - 103)
$Z_{SM} \leq z_t < Z_{AG}$	Eq. (4 - 102)	Eq. (4 - 103)	Eq. (4 - 104)	0	Eq. (4 - 105)
$Z_{AG} \leq z_t$	Eq. (4 - 102)	Eq. (4 - 103)	Eq. (4 - 104)	Eq. (4 - 106)	Eq. (4 - 105)
$z_b \leq Z_{AG}$	0	0	0	1	0

$$0 \leq W_{sb} \frac{Z_{TR} - z_t}{\Delta x} \leq 1$$

$$0 \leq W_{sm} = \frac{\min(Z_{sm}, z_t) - \max(Z_{TR})}{\Delta x} \leq 1$$

$$W_{inv} = W_{rs} + W_{sm}$$

$$0 \leq W_{rw} = \frac{\min(Z_{AG}, z_t) - \max(Z_{SM}, z_b)}{\Delta x} \leq 1$$

$$W_{ds} = 1 - W_{sb} - W_{rs} - W_{sm}$$

The closure relationship is then calculated according to

$$X_{reflood} = W_{sb} \times X_{bubbly} + W_{ds} \times X_{dispersed} + W_{inv} \times X_{inverted}$$

where X represents either A_i , H_{ALVE} , H_{CHTI} , or H_{CHTA} . For flashing, the maximum value of H_{ALVE} or a special model described in the next section is used. For the case of noncondensables, the value of H_{ALVE} is modified. The exact process is discussed in the references.

Bubbly-Flow Models.

In bubbly CHF upstream of the quench front, the void fraction is restricted to be between 0.05 and 0.30. Slugs are not allowed to be formed. The interfacial area and heat transfer coefficient are identical to those used in HTCOR under similar conditions. If T_1 is greater than T_{sat} then the heat transfer coefficient is not calculated using this method. Instead, the reflood model uses a simple model based on the kinetic theory of evaporation from liquid surfaces. The theoretical maximum evaporation rate predicted by this theory was converted by the code authors to a Heat Transfer Coefficient (HTC). The coefficient of evaporation of 0.4 is modified to predict evaporation rate for each of the flow regimes in nucleate and film boiling. The HTC for flashing is given by:

$$H_{fls} = C_{eva} h_{fls,teo} = C_{eva} \times 0.1857 (\theta_v h_{fg}^2 / T_{sat}^{1.5})$$

The coefficient C_{eva} is defined for bubbly- and mist-annular-flow and is assumed to be void fraction dependent in the bubbly flow when the cell void fraction is between 0.3 and 0.5; otherwise it is a constant. The interfacial areas in bubbly flow are identical to those in HTCOR. The liquid side heat transfer factor during flashing is then given by

$$H_{ALV} = h_{fls} A_{I, bubble}$$

For the mist annular regime, C_{eva} is equal to 0.0002.

If the flow regime is determined as the transition between the bubbly and mist annular flows, an interpolation is used according to

$$H_{ALV,trans} = W \times H_{ALV,mist} + (1-W) \times H_{ALV,bubbly}$$

Dispersed and Post-Agitated Inverted Annular Flows

The flow regimes farthest from the quench front according to Ishii are the dispersed and post-agitated inverted annular flows. In the reflood model, the void fraction is restricted to be between 0.3 and 0.9995. If there is a cold wall in the hydro cell, a thin liquid film can form and is allowed by the model. To evaluate the interfacial area it is necessary to divide the liquid into a film and droplet phase. The liquid is divided by determining a liquid film thickness and equivalent liquid fraction for the film. Once this is determined, a liquid drop fraction may be obtained and the corresponding interfacial areas calculated.

The vapor to interface heat transfer is calculated in the dispersed flow regime by first calculating the mass fraction of liquid. The mass fraction is then used to determine a homogeneous void fraction. If the homogeneous void fraction is greater than 0.75 and the difference between $1 - \alpha_{dd}$ is less than or equal to 0.95, then $H_{CHTI,dispersed}$ is set equal to 10^{-6} W/K. Otherwise a correlation is used according to Unal et al⁴⁻²¹. The correlation was modified to allow its use as a heat transfer coefficient instead of a vapor generation rate. Changes were also made to the constants which appear in the correlation.

If the cell void fraction is less than 0.98, then the flow regime is assumed to be post-agitated inverted annular flow. In that case, the value of H_{CHTI} is calculated using the value for dispersed inverted annular flow with a void fraction weighting according to

$$H_{\text{CHTI,post-ag}} = H_{\text{CHTI,DP}} ((\alpha - \alpha_{\text{SM}}) / (\alpha_{\text{DP}} - \alpha_{\text{SM}}))^{-0.01}.$$

The liquid heat transfer in the reflow model is not calculated using subroutine HTIF when T_1 is less than T_{sat} . Rather, the sensible heat that goes to the sub-cooled liquid is calculated in HTVSSL in the wall-to-liquid HTC. If the liquid is superheated, then the coefficient in the flashing model is set equal to 0.002. The value of H_{ALV} for the dispersed or post-agitated inverted annular flow is calculated as

$$H_{\text{ALV,dispersed (or post-agitated)}} = h_{\text{fls}} A_{\text{I,dispersed (or post-agitated)}}$$

where h_{fls} is calculated according to the flashing model discussed earlier.

Inverted Annular Flow

In inverted annular flow, the void fraction is limited to between 0.05 and 0.95. In this region, the interfacial area and the heat transfer coefficients are calculated according to the following.

The hydraulic area of the liquid core is calculated by adjusting the hydraulic diameter of the channel by multiplying by $1 - \alpha$. The interfacial area is computed as the product of the core hydraulic diameter and the length $\Delta x \pi$. If flashing is occurring, then the interfacial area is recalculated using an expression for the film thickness developed by Ishii⁴⁻²². This is then used to calculate the wall void fraction and the interfacial surface area near the walls. The void fraction for bubbles may then be determined using the interfacial area near the walls and the void fraction. The total interfacial area is then the sum of the wall and bubble interfacial area.

The vapor heat transfer model is a simple product of constant times the interfacial area for inverted flow calculated using the method in the previous paragraph. The liquid side heat transfer coefficient is not calculated in subroutine HTIF for the inverted annular flow regime when T_1 is less than T_{sat} . The sensible heat is calculated in HTVSSL in the wall-to-liquid heat transfer coefficient. As is the case for post-agitated flow, the coefficient for evaporation is set equal to 0.002. The H_{ALV} uses the same formula as used in dispersed and post-agitated flow.

Spacer Grid Model

If grid spacers are present, an attempt is made to correct for the cooling effect of the grid spacers. The vapor-to-liquid heat transfer coefficient is modified to account for the temperature of the grid spacer.

Noncondensables

An attempt to account for the presence of noncondensables is also made.

4.2.4 COBRA-TF Code

4.2.4.1 Introduction

The COBRA-TF code was developed by Pacific Northwest Laboratory under the sponsorship of the Nuclear Regulatory Commission to provide a best-estimate calculational capability for transient and accident analysis. The version of the COBRA-TF⁽⁴⁻²⁴⁾ code which is being used in the RBHT program was refined from the original version of the COBRA-TRAC code⁽⁴⁻²⁵⁾ as part of the FLECHT-SEASET 163 Blocked Bundle Test and analysis program.

COBRA-TF has several differences as compared to the TRAC and RELAP codes which make it more suitable for analyzing rod bundle reflood tests. COBRA-TF uses a separated flow model for the two-phase region conservation equations which model three distinct fields. The three fields which are modeled include: the continuous liquid field for low void fraction flow and falling or climbing films; vapor field for the steam flow, and the entrained droplet field. Using two liquid fields is a more accurate and convenient method of representing the liquid phase over a wide range of two-phase situations which would occur during reflood of a hot bundle. Flow regimes such as inverted annular, churn-turbulent, and droplet flow can be modeled more accurately. One can also model the flow regime transitions more accurately as well as countercurrent flow in which a liquid film falls and the entrained droplets are carried upward. In addition in the FLECHT-SEASET version of the COBRA-TF code, a fourth field exists which models the effects of a non-condensable gas.

Mass conservation equations are written for each field, continuous liquid, vapor, entrained liquid, and non-condensable gas. The energy equations are more simplified in that the continuous liquid and the entrained liquid are assumed to have the same liquid temperature within the same computational cell. Also, a combined energy equation is used for the vapor and non-condensable gas. There are three momentum equations solved for the vapor, continuous liquid, and the entrained liquid. The momentum equations are three dimensional such that they can represent a rod bundle array with the smallest computational cell being a single subchannel. When the code is used in the subchannel formulation, some of the higher order momentum flux terms which represent the cross products of the lateral velocities are ignored.

In the FLECHT-SEASET flow blockage program⁽⁴⁻²⁴⁾, the capabilities of COBRA-TF were expanded to include a small droplet field which is used to model the smaller micro-droplets which are generated as larger drops shatter when they impact structures in the rod bundles such as spacer grids and flow blockages. There were some simplifications used for the small droplet field model. The small droplet field was not directly coupled to the hydrodynamic solution matrix, the interface of the small droplet field occurred as source and sink terms in the equation

such that the mass of the entrained liquid was preserved. It was also assumed that there was no lateral flow of the small droplets, and the model was not valid for negative top down flow.

COBRA-TF is also unique in that in addition to the conservation equations, the code uses a interfacial area transport equation which calculates the total droplet interfacial area in a computational cell considering the sources and sinks of interfacial area such as entrainment and deposition of the drops on to a liquid film.

One of the differences of COBRA-TF from the other systems codes is that it has both "hot" wall and "cold" wall flow regimes. The hot wall regime is used when the wall temperature exceeds $T_{\text{sat}} + 42 \text{ }^\circ\text{C}$ (75°F). The hot wall regimes include subcooled inverted annular flow, saturated liquid churn or slug flow, dispersed droplet-vapor flow, falling film flow, and top-down liquid deluge flow. The hot wall flow regimes and logic selection are shown in Figures 4-12 and 4-13. For bottom reflood when the reflood flow is subcooled, an inverted annular flow regime is assumed. If the liquid is saturated, the liquid churn or slug flow regime is assumed and the liquid is treated as very large droplets surrounded by vapor.

4.2.4.2 COBRA-TF Heat Transfer Package

The heat transfer package in COBRA-TF consists of a library of correlations and a selection logic which allows the code to predict a boiling curve as a function of the computational cell void fraction, pressure, mass flow and the heated surface temperature. Figure 4-14 shows the boiling curve and regions of interest and Figure 4-15 shows the heat transfer regime selection logic in a simplified fashion. The heat transfer package which is used by the code calculates both the wall-to-fluid heat transfer as well as the interfacial heat transfer between the phases (Table 4-5). Since separate energy equations are used for the phases, a non-equilibrium flow will be calculated in some cases. Therefore, the interfacial heat transfer and the interfacial heat transfer area are calculated to determine the temperature of each phase. Both will be discussed below with the emphasis on reflood heat transfer.

Single Phase Vapor

COBRA-TF calculates the local Reynolds number within the computational cell and determines if the flow is laminar or turbulent. If the flow is turbulent, it uses the maximum of the Dittus-Boelter correlation⁽⁴⁻²⁾ or the correlation developed from the FLECHT-SEASET 161-rod bundle tests⁽⁴⁻²⁶⁾. If the flow is calculated to be laminar, the code uses a Nusselt number of 10, which is based on the FLECHT-SEASET data.

Single Phase Liquid

In a similar fashion, the code calculates the Reynolds number of the cell and if the flow is turbulent, the code uses the Dittus-Boelter correlation for the convective heat transfer. If the flow is calculated to be laminar, the heat transfer correlation by Sparrow et al⁽⁴⁻²⁷⁾ is used which has a maximum Nusselt number equal to 7.86.

Table 4-5
Interfacial Heat Transfer Area Per Unit Volume

Mode of Heat Transfer	Correlation (Btu/hr-ft ² -°F)	Flow Regime
H_{SHV}	$\frac{f_I}{2} \rho_v C_{p_v} U_{v\ell} Pr_v^{-2/3}$	Film
	$\frac{(2.0 + 0.55 Re_d^{0.5} Pr_v^{1/3}) \frac{k_v}{2r_d}}{1 + 0.5 (h_v - h_g)/h_{fg}}$	Drop(a)
	$\frac{(2.0 + 0.55 Re_v^{0.5} Pr_v^{1/3}) \frac{k_v}{D_H}}{1 + 0.5 (h_v - h_g)/h_{fg}}$	Liquid chunk, inverted annular
H_{SCV}	1.0×10^4 (b)	All regimes
H_{SHL}	1.0×10^5 (b)	Large bubble, liquid chunk and inverted annular
H_{SHL}	<p style="text-align: center;">The maximum of</p> $1.925 \rho_\ell C_{p_\ell} U_\ell / [Re_f^{2/3} Pr_\ell^{2/3}]$ <p style="text-align: center;">for $Re_f \leq 1000$</p>	Film(c)

a. Rowe, P. N., et al., "Heat Transfer From a Single Sphere in an Extensive Flowing Fluid," Trans. Inst. Chem. Engin. 43, 1965, T14-T31.

b. A constant large value is used to drive toward phase equilibrium.

c. From Colburn analogy using friction factors of Hughmark^(e)

Table 4-5
Interfacial Heat Transfer Area Per Unit Volume (cont.)

Mode of Heat Transfer	Correlation (Btu/hr-ft ² -°F)	Flow Regime
H _{SCL}	$0.2701 \rho_l C_{p_l} U_l / [Re_f^{0.38} Pr_l^{2/3}]$ <p>for $1000 \leq Re_f$</p> <p>and</p> $2.0 k_l / \delta$	Drop(d)
	$C \frac{\pi^2 k_l}{3 r_d} \quad (C = 2.7)$	
	$1.925 \rho_l C_{p_l} U_l / [Re_f^{2/3} Pr_l^{2/3}]$ <p>for $f Re < 1000$</p>	Film(c)
	$0.2701 \rho_l C_{p_l} U_l / [Re_f^{0.38} Pr_l^{2/3}]$ <p>for $1000 \leq Re_f$</p>	Drop, liquid chunk, inverted annular(d)
	$C \frac{\pi^2 k_p}{3 r_d} \quad (C = 2.7)$	

- d. Andersen, J. G. M., REMI/HEAT COOL, A Model for Evaluation of Core Heatup and Emergency Core Spray Cooling System Performance for Light-Water Cooled Nuclear Power Reactors, "Heat Transfer in a Spherical Droplet," Report 296, Riso National Laboratory, Denmark, September 1973.
- e. Hughmark, G. A., "Film Thickness, Entrainment, and Pressure Drop in Upward Annular and Dispersed Flow," J. Amer. Inst. Chem. Engin. 14, 1973, 1062.

Table 4-5
 Interfacial Heat Transfer Area Per Unit Volume (cont.)

Flow Regime	Interfacial Area, A''_I
Film	$\alpha_v P_w/A$
Liquid chunk	$N_d \pi D_H^2$ (a)
Inverted annular	$\alpha_l P_w/A$
Drop	Drop interfacial area transport equation

a.
$$N_d = \frac{\alpha_l}{\frac{\pi D_H^3}{6}}$$

Nucleate Boiling

When the wall temperature exceeds the saturation temperature but is less than the wall temperature at the critical heat flux point, the Chen⁴⁻⁴ correlation is used to calculate the wall heat transfer. The Chen correlation applies to both saturated nucleate boiling and forced convection evaporation and will automatically transition into single phase convection at low wall superheats and into pool boiling at low mass flow rates. The Chen correlation regards the wall heat transfer as consisting of a combination of forced convection heat transfer as well as pool boiling heat transfer. In this fashion both extreme limits of forced convection and pool boiling are preserved.

Subcooled Nucleate Boiling

The Chen correlation can also be extended into the non-equilibrium regime of subcooled nucleate boiling. Again, the Chen correlation combines a forced convective heat transfer contribution and a boiling contribution to calculate the total wall heat transfer. For the subcooled case, the "F" factor used in the Chen correlation is set to unity but the remainder of the correlation is applied as in the nucleate boiling case.

In subcooled nucleate boiling, there exists thermodynamic non-equilibrium between the voids which are formed and the bulk liquid temperature which is subcooled. Therefore, there is heat transfer between the vapor and the liquid such that the vapor condenses and the liquid temperature increases along the channel. The heat transfer processes of interest include:

- Forced convection to the liquid
- Vapor generation at the wall
- Condensation near the wall
- Bulk condensation in the liquid core.

The partition of the vapor generation and the forced convection portions of the wall heat flux are calculated by the Chen correlation for the given set of conditions. The interfacial heat transfer processes are directly calculated in the fluid energy equations as part of the fluid conditions for the cell. The near wall condensation was calculated using the Hancox-Nicoll correlation⁽⁴⁻²⁸⁾ which was then subtracted the nucleate boiling heat transfer to obtain the net vapor generation. There were further refinements which accounted for the fraction of the subcooled liquid which would penetrate the saturated liquid layer on the wall using the Rouhani and Axelsson correlation⁽⁴⁻²⁹⁾. Using this approach, the net amount of vapor generation at the wall can be calculated and the remainder of the vapor will then be mixed in to the bulk flow through the liquid energy equation and will condense,

Critical Heat Flux

COBRA-TF calculates the critical heat flux and the wall temperature superheat at the CHF point to fix this location on the boiling curve as shown in Figure 4-14 . For reflood heat transfer, the

Zuber⁽⁴⁻³⁰⁾ pool boiling correlation is chosen for the critical heat flux since the liquid flow velocities are small.

Minimum Stable Film Boiling Point

The other point which is fixed on the boiling curve is the minimum film boiling point, T_{\min} . This location denotes the boundary between stable film boiling and transition boiling. COBRA-TF uses the larger of a modified version of the homogeneous nucleation temperature which is curve-fit as a function of the difference between the critical pressure and the local pressure, and which has also been modified to account for wall properties; and the Henry⁽⁴⁻³¹⁾ modification of the Berenson correlation. In addition, for reflood, COBRA-TF limits the value of T_{\min} to be

$$426 \text{ }^{\circ}\text{C} (800 \text{ }^{\circ}\text{F}) < T_{\min} < 650 \text{ }^{\circ}\text{C} (1200 \text{ }^{\circ}\text{F})$$

Transition Boiling

The transition region is viewed as a mixture of film boiling with a vapor layer contacting the wall and nucleate boiling or wetted wall in which liquid contact with the wall is possible. The wetted wall portion of the wall heat flux is calculated using Ganic and Rohsenow⁽⁴⁻³²⁾ which uses the McCoy and Hanratty model⁽⁴⁻³³⁾ for determining the droplet migration to the wall. Once the droplet contacts the wall a droplet efficiency is calculated which is a function of the wall temperature and the liquid temperature. At high wall temperatures, the efficiency becomes very small as the drops will not contact the hot wall. The wetted wall portion of the heat flux is added to the dry wall film boiling heat flux calculation to give the total transition boiling wall heat flux.

There are separate models for top down quench in which the heat transfer is enhanced below the top down quench front location which is used as a multiplier on the critical heat flux.

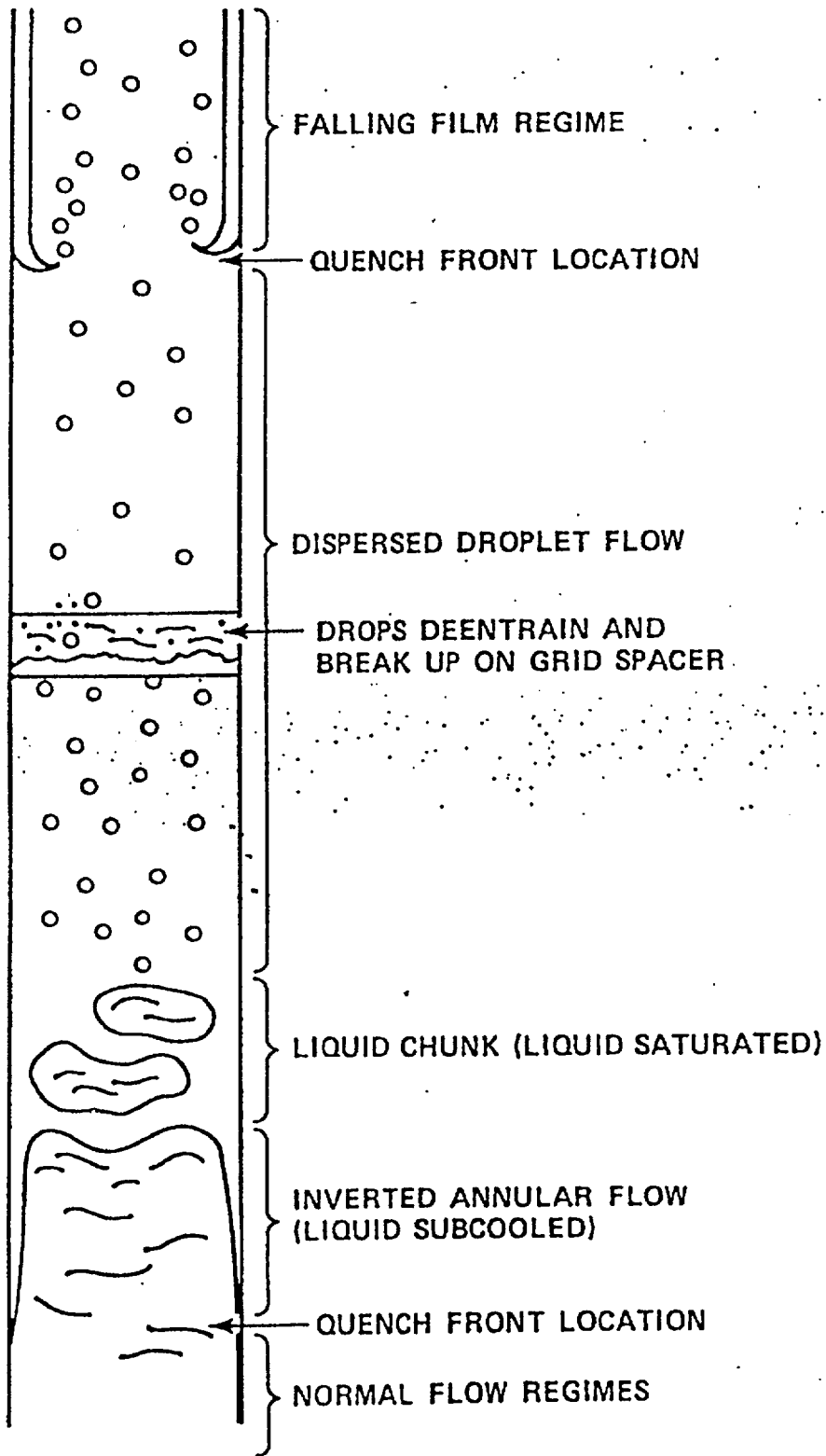


Figure 4-12 Hot Wall Flow Regimes.

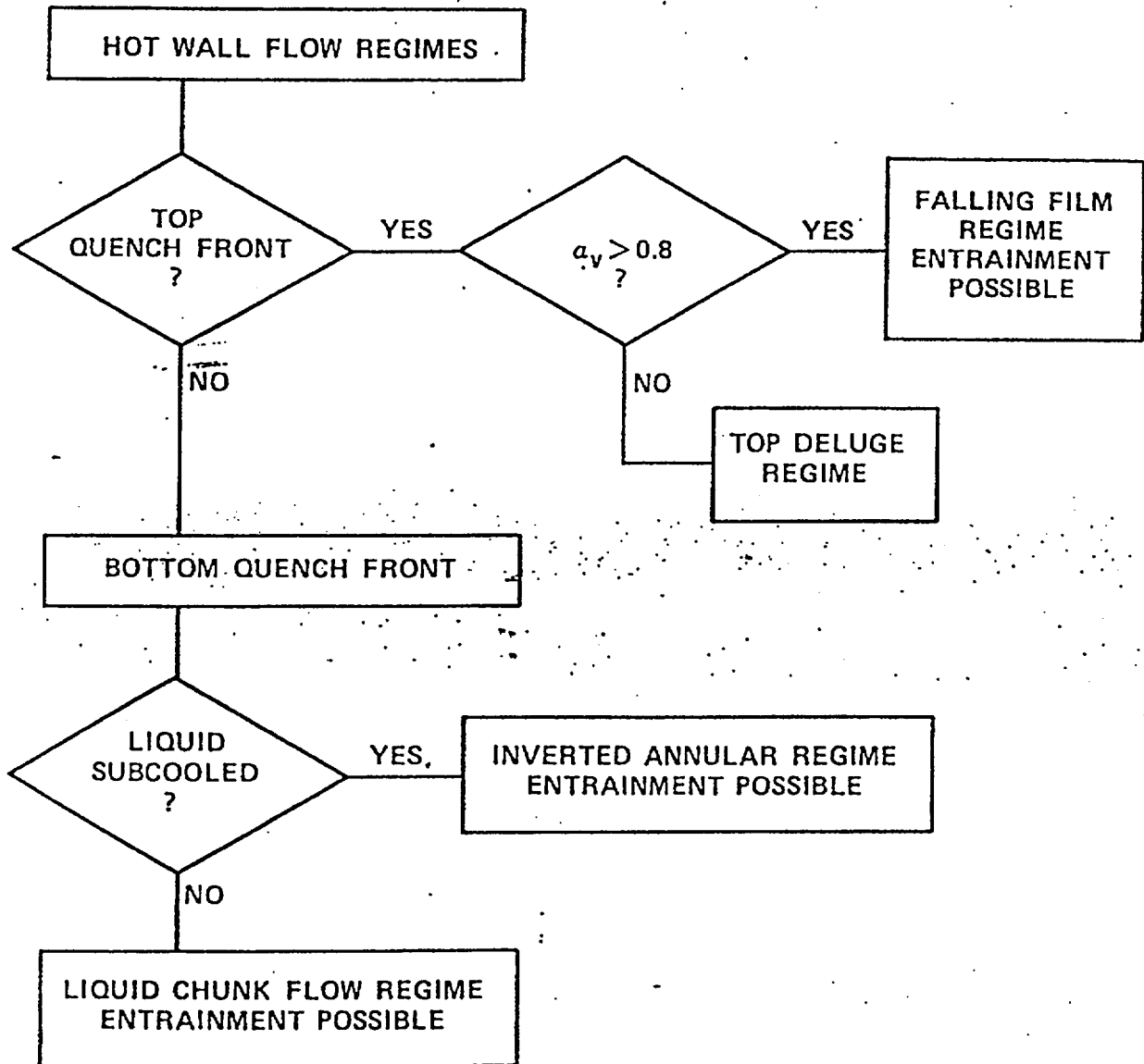


Figure 4-13 Hot Wall Flow Regime Selection Logic.

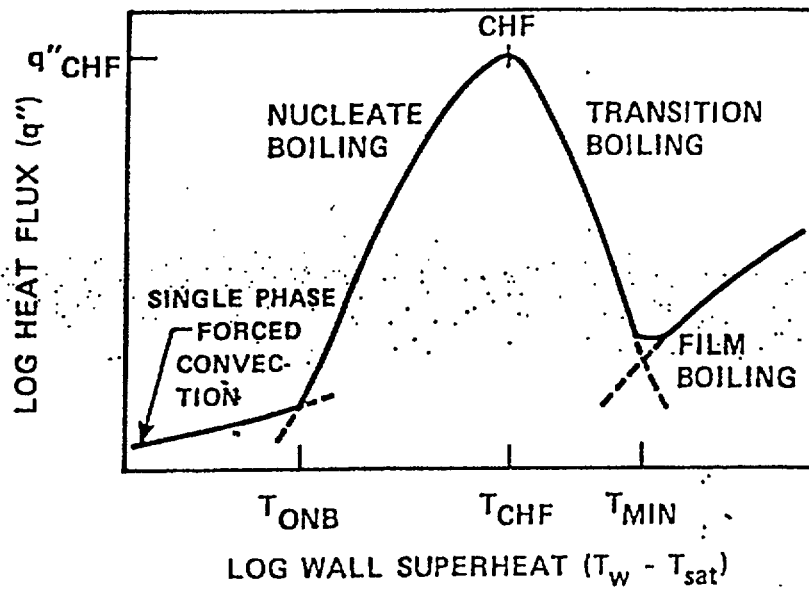


Figure 4-14 Schematic Representation of Boiling Curve.

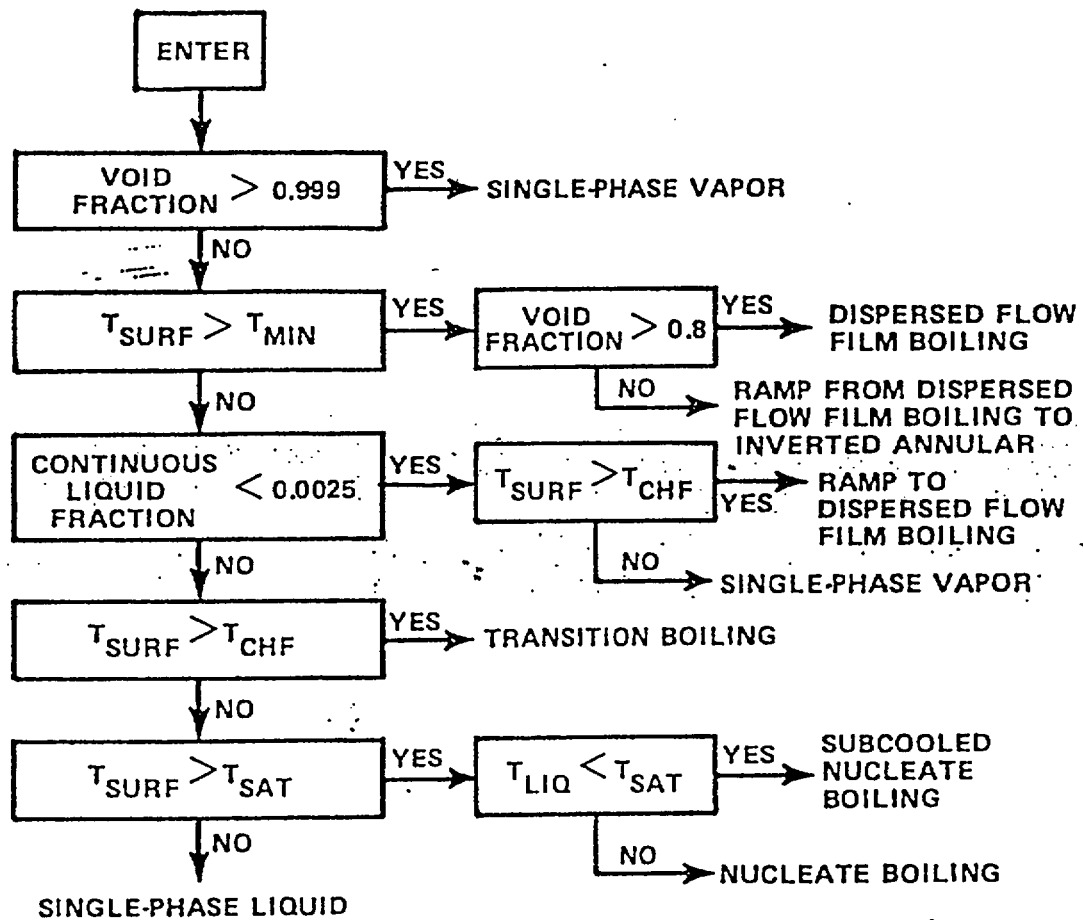


Figure 4-15 Heat Transfer Regime Selection Logic.

Inverted Annular Film Boiling

COBRA-TF assumes the wall heat transfer is in inverted annular film boiling if the wall temperature is greater than T_{\min} , and the void fraction is less than 0.4. The modified Bromley correlation⁽⁴⁻¹⁰⁾ is used for the film-boiling portion of the wall heat flux. The radiation heat transfer from the wall to the liquid is also accounted for as well as the droplet contact heat transfer using the Ganic and Rohsenow correlation as described earlier. Therefore:

$$q''_{\text{IAFB}} = q''_{\text{Brom}} + q''_{\text{R}} + q''_{\text{W-D}}$$

When the cell void fraction is greater than 0.4 and less than 0.9, the wall heat flux is linearly interpolated between the value for inverted annular film boiling and dispersed flow film boiling. There are also interfacial heat and mass transfer models in the inverted annular film-boiling regime which include estimates of the interfacial area between the vapor and the liquid such that the proper liquid and vapor temperatures can be calculated. The heat flux behavior as a function of void fraction is shown in Figure 4-16 .

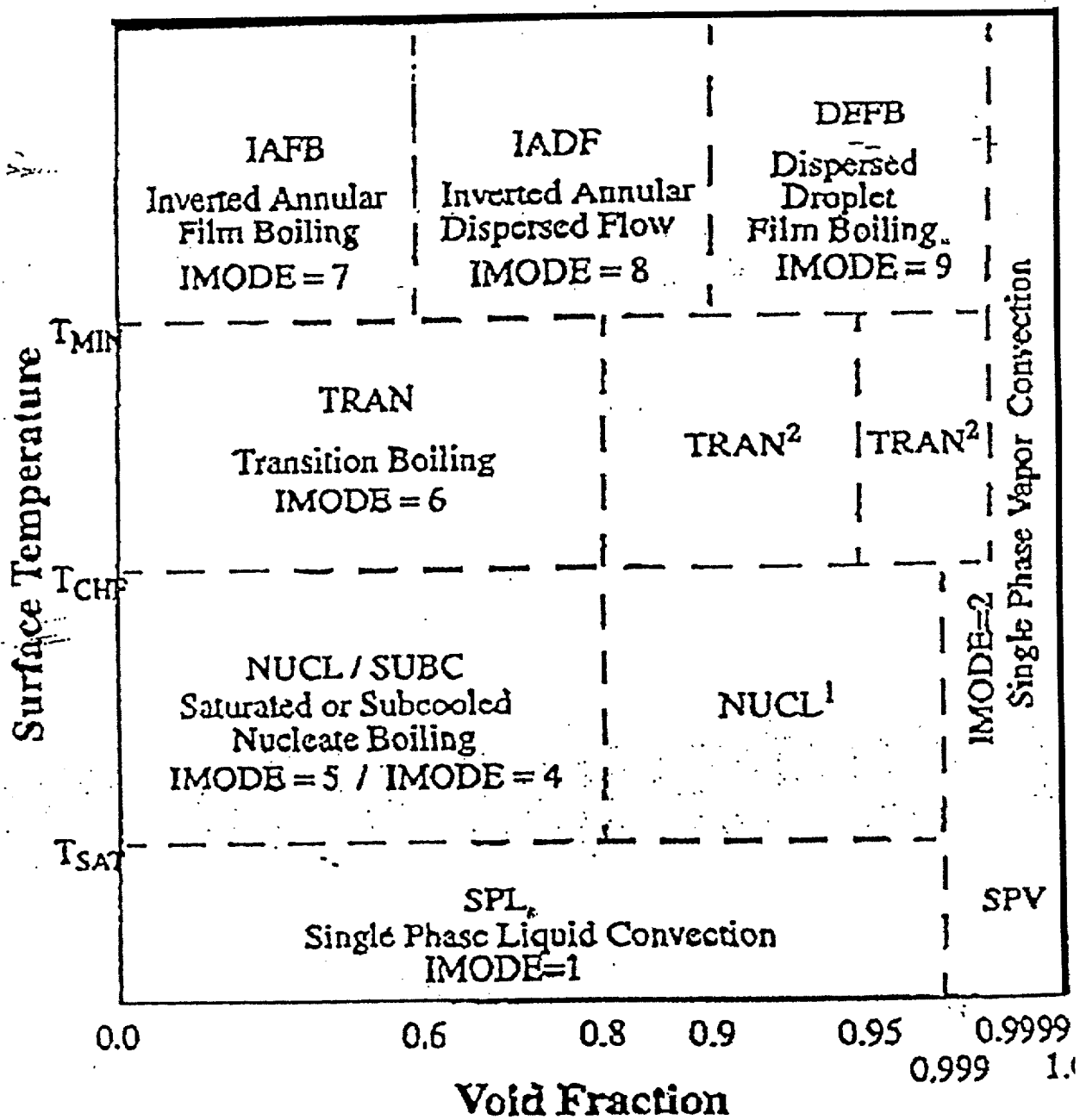


Figure 4-16 WCOBRA/TRAC Heat Transfer Regime Map.

Dispersed Flow Film Boiling

The dispersed flow film boiling is assumed to occur when the wall temperature exceeds T_{\min} and the void fraction is greater than 0.9. The dispersed flow film boiling heat transfer mode received the greatest amount of attention and refinement as part of the FLECHT-SEASET program. The wall heat flux in dispersed flow film boiling is comprised of three different heat transfer mechanisms which are summed to give the total wall heat flux:

Then is:

$$q''_{\text{DFFB}} = q''_{\text{FC}} + q''_{\text{R}} + q''_{\text{w-D}}$$

where:

q''_{FC} is the vapor convective heat flux (either laminar or turbulent),

q''_{R} is the radiation heat flux, and

$q''_{\text{w-D}}$ is the droplet impinging heat flux or droplet contact heat flux.

The vapor convective heat flux is enhanced by a factor "psi" which experimentally accounts for the effect of the entrained droplets increasing the convective heat transfer. Data for the enhancement factor was obtained from the FLECHT and FLECHT-SEASET programs and has been compared to data obtained by Drucker and Dhir⁽⁴⁻³⁴⁾. The two-phase enhancement factor can be shown to be an extension of the basic analogy theory between heat transfer and momentum transfer as given in Kays⁽⁴⁻³⁵⁾. Figure 4-17 shows the scatter of the data for the enhancement value psi. Note the scale on the plot. It is relatively easy for value for the single-phase convective heat transfer to be enhanced by 100% in a two-phase dispersed flow.

The radiation heat transfer q''_{R} , consists of two separate models. The surface-to-surface radiation is solved on a subchannel basis⁽⁴⁻¹⁾ such that small test facilities with colder housing can be modeled more accurately. In a separate calculation, the radiation heat transfer to the droplets and vapor are calculated using the Sun et al model⁽⁴⁻¹¹⁾ for the fluid radiation component.

The droplet impingement heat flux term is the same as that described earlier. However, this term is very small or negligible in the dispersed flow film boiling since the wall temperatures are much higher and the heat transfer efficiency of droplets hitting the wall is nearly zero.

Above a void fraction of 0.999, the heat transfer becomes single-phase vapor.

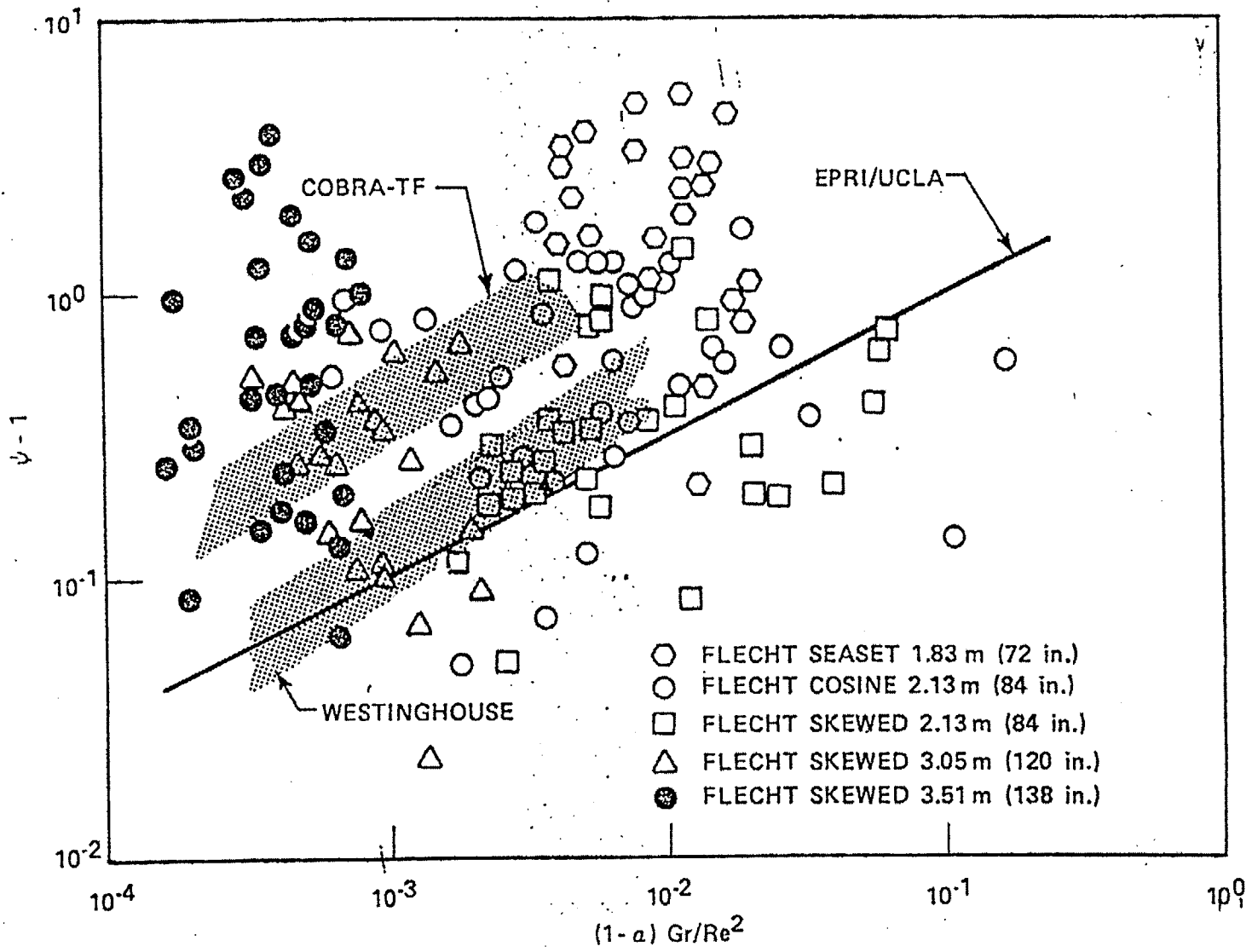


Figure 4-17 Two-Phase Enhancement: Comparison of Models and Reflood Data.

Quench Front Model

COBRA-TF uses fine variable mesh ⁽⁴⁻³⁶⁾ which will insert additional nodes into the heated structure if significant axial temperature gradients exist. This allows a more accurate representation of the true localized energy release from a localized portion of a heater or nuclear rod rather than the energy release from all the structures within the fluid node. Fine mesh heat transfer cells for axial and radial conduction in the structure are superimposed on the coarser hydraulic computational cells. The heat transfer package described above is applied to each of these smaller structural nodes to obtain the local heat transfer. In this fashion, the energy release at the quench front is smoother, and the effects of axial conduction in the quench front region are simulated.

Spacer Grid Heat Transfer Models

One of the major additions to the COBRA-TF code was the inclusion of heat transfer models for the dispersed flow film-boiling regime (void fraction greater than 0.9) which represented the experimental observations on the effects of rod bundle spacer grids. Spacer grids result in three additional heat transfer mechanisms in the rod bundle flow, namely:

Convective heat transfer enhancement downstream of the grid,

Rewetting of the grid structure,

Entrained droplet breakup caused by the grid structure.

Convective enhancement downstream of the spacer grids was observed in several single phase experiments and is due to the thinning of the thermal and velocity boundary layers on the rods as well as the additional turbulence introduced by the grid in the flow. Data from these experiments were correlated in terms of the grid blockage area in the rod bundle and an exponential multiplier, which diminishes downstream of the grid, according to Yao, Hochreiter, and Leech⁽⁴⁻³⁷⁾. This correlation is used in COBRA-TF as a multiplier on the vapor convective heat transfer calculation described above for the dispersed flow heat transfer regime.

Spacer grids can be either dry, that is, with grid temperature which exceed T_{min} , or wetted with temperatures which are close to the saturation temperature. If a fraction of the grid is at the saturation temperature, it is assumed that a liquid film is present on that surface area. Since the grids are stationary, they have significant surface area; if the grid wets, a significant amount of interfacial heat transfer area added to the interfacial area transport equation as an area source term. The result of this is more rapid de-superheating of the vapor flow in the rod bundle. As the vapor de-superheats, the driving temperature for the rod heat flux increases ($T_{ROD} - T_v$), and the rod wall heat flux increases and the rod cools.

There is a two zone detailed spacer grid model in COBRA-TF which calculates the location of the quench front on the grid, and the dry and wet grid temperatures considering the radiation heat transfer from the heater rods, convective heat transfer from the superheated vapor as well as the

quenching of the spacer grid. The model for the spacer grid is shown in Figure 4-18. In this fashion, the fraction of the grid which is either dry or wet can be calculated as a function of the thermal-hydraulic conditions within the channel to determine the amount of grid area which should be added to the interfacial area transport equation. The additional steam generation due to the evaporation of the liquid film on the grid is also added into the hydrodynamic solution.

The third spacer grid model indicates that when high velocity entrained liquid droplets impact the grid structure, the drops can shatter producing a range of smaller "micro droplets" which are more easily evaporated. As the micro droplets are evaporated, the vapor de-superheats due to the increased surface area for interfacial heat transfer as well as the addition of saturated vapor due to the droplet evaporation. Both heat transfer effects reduce the vapor temperature and result in a larger temperature difference between the vapor and the rod surface which increase the rod heat flux promoting improved cooling.

Figure 4-19 indicates the droplet breakup behavior. The parameter which was found to correlate the ratio of the shattered drop size to the initial drop size was the droplet Weber number for flow normal to the spacer grids as seen in Figure 4-20. For low Weber numbers, the change in the drop size is not significant, at most a factor of two. For these drops, the interfacial area of the larger shattered drops was added to the interfacial area transport equation as an additional source term. For the very small drops which were generated at higher drop Weber numbers, these drops are put into the separate small-drop field described earlier. In addition, if there are small drops upstream of a spacer grid, they are also broken-up by the downstream spacer and the resulting small drop populations are then merged preserving the droplet mass, interfacial area and momentum.

COBRA-TF heat transfer models, which are similar to the spacer grid models, have also been developed for flow blockage in rod bundle arrays and are described in Reference 4-24 .

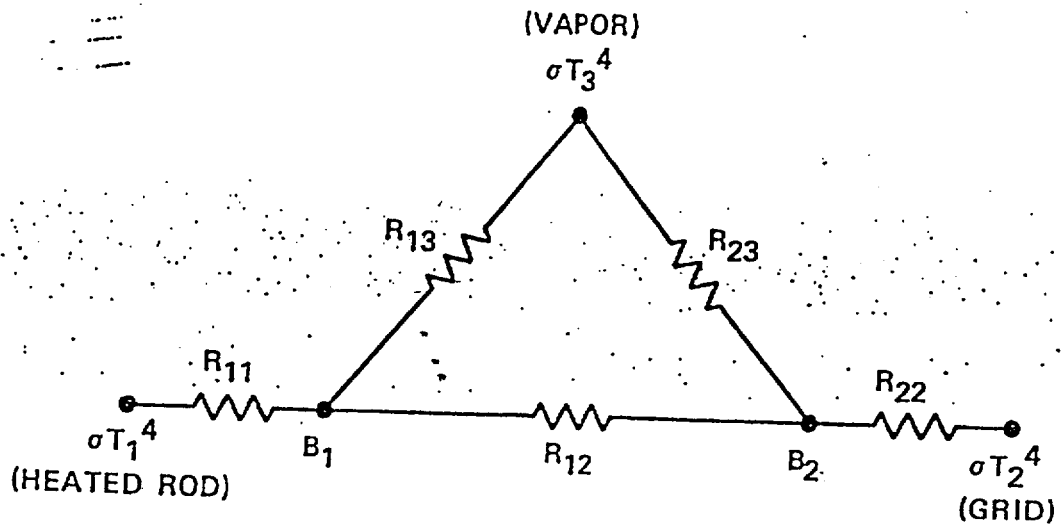


Figure 4-18 Radiation Heat Flux Network.

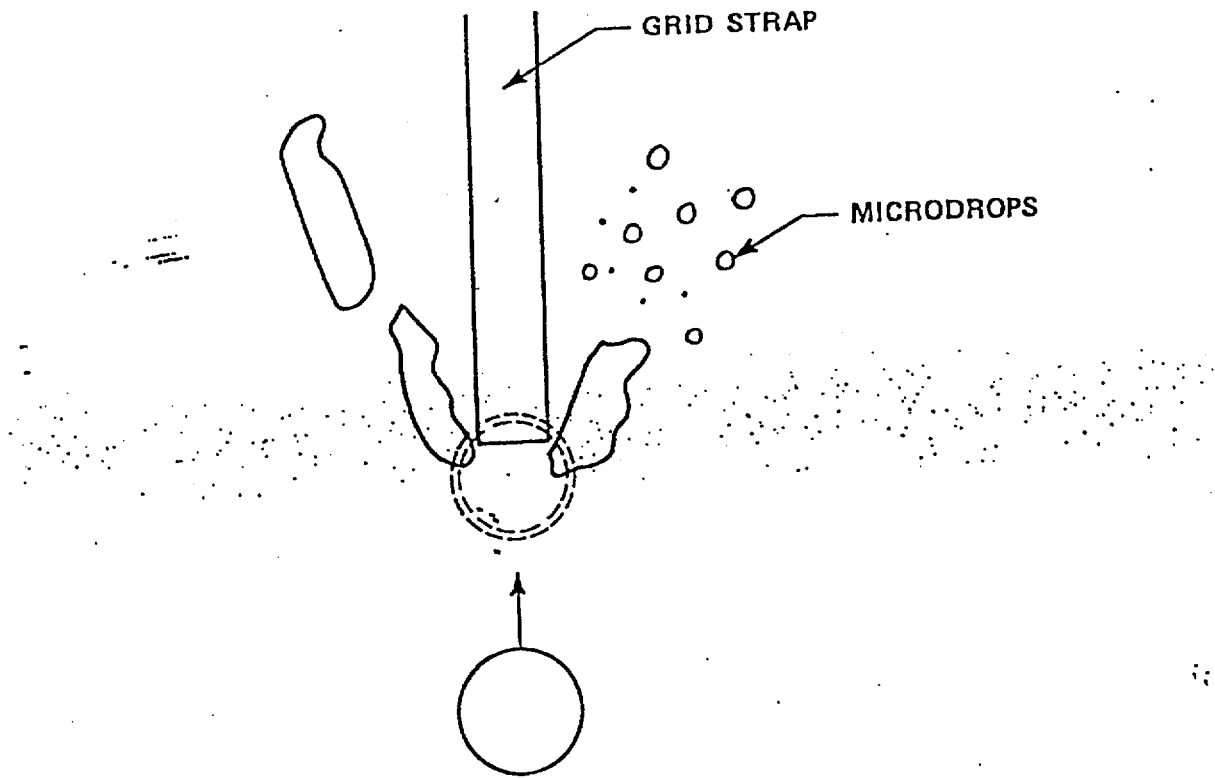


Figure 4-19 Droplet Breakup.

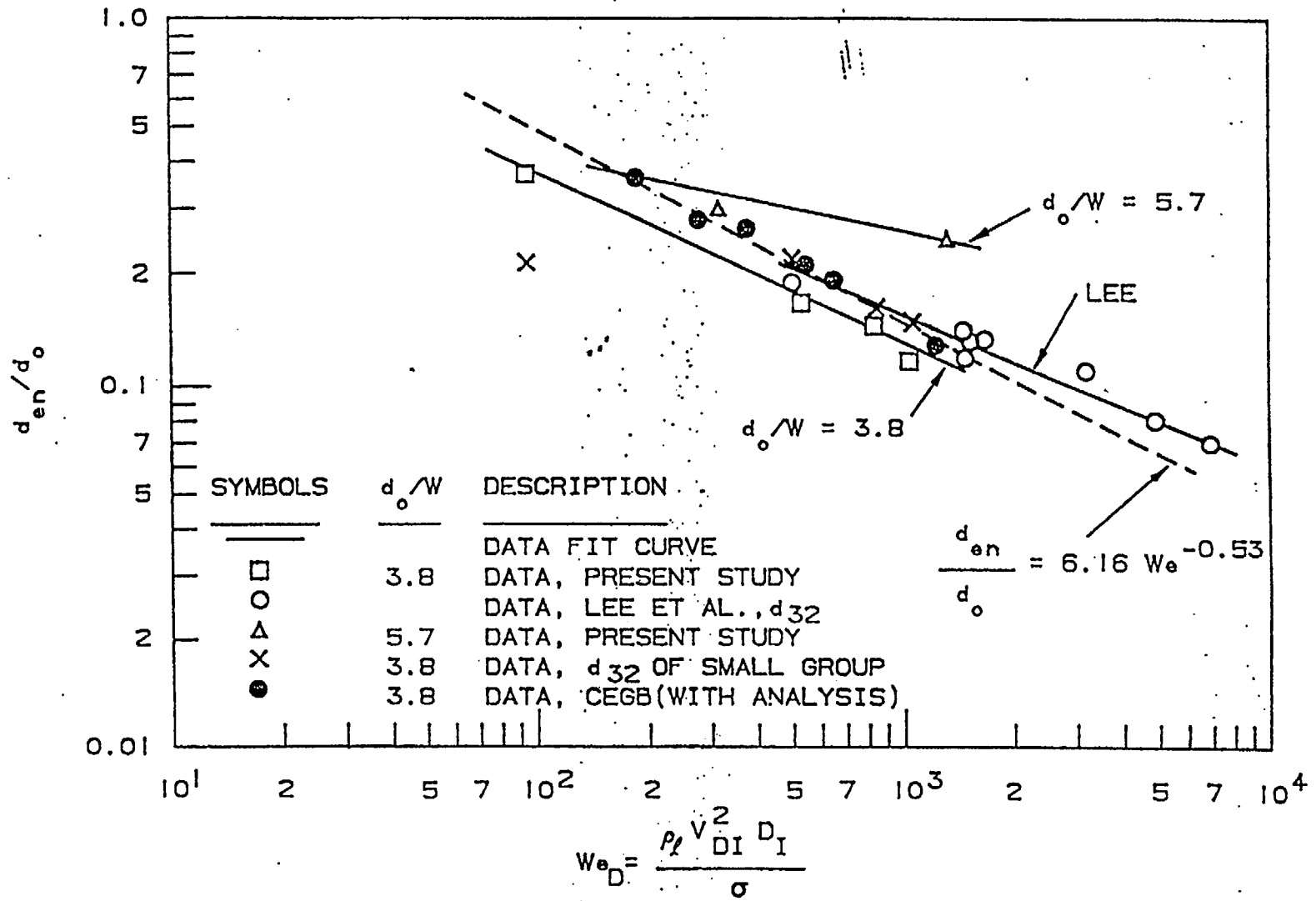


Figure 4-20 Shattered Droplet Size from Heated Grid Straps.

4.3 Road Map from the PIRT, to the Code Models, to The test Instrumentation and Data Analysis

4.3.1 Single Phase Liquid Convection Below the Quench Front (Table 4-6)

The contribution of the single-phase liquid convection during a reflood transient ranks low in the PIRT. To calculate the heat transfer with the liquid single-phase (and vapor single-phase), the codes use different correlations depending on the Reynolds number. In general the Dittus-Boelter correlation is used for turbulent flow while other correlations are used to calculate heat transfer in the laminar flow regime. These correlation are based on pipe geometry data and in general to geometries quite different than the bundle geometries. RELAP5/MOD3 uses the P/D correction relation to account of this effect but its uncertainty is very high. The two TRAC codes do not account of this effect at all. In COBRA-TF a specific correlation was developed during FLECHT-SEASET experiments but was tuned on the 163 rod bundle geometry.

Beside the geometry effect, the flow regime during reflood is often in the transition between laminar and turbulent flow and therefore a bundle specific correlation needs to be developed to predict accurate convective heat transfer. The RBHT facility allows to transverse temperature probe across the channel. This allows to have a better estimate of the bulk average temperature which is needed to assess these models.

The important phenomena were identified in the PIRT in Section 2 for the different periods or phases of the reflood transient. Examining the PIRT for single phase convective heat transfer, the items which are highly ranked are:

- The decay power which is the energy source into the fluid,
- The liquid velocity or Reynolds number,
- The liquid temperature or subcooling,
- The convective heat transfer coefficient, which is ranked as a medium.

The difference in the ranking of the liquid velocity and subcooling and the convective coefficient is that the convective fluid conditions will determine the behavior of the flow in different locations downstream, whereas the effects of uncertainty on the heat transfer coefficient for single phase heat transfer has a very small effect on the calculated peak cladding temperature.

The decay power is a test boundary condition which is controlled in the experiment and is directly measured such that this parameter is known accurately for a given test.

**Table 4-6 - Single Phase Liquid Convective Heat Transfer
in the Core Component During Reflood
Below the Quench Front**

Process/Phenomena	Ranking	RELAP5/MOD3.2		TRAC-B		TRAC-P		COBRA-TF	
		Does the model exist	Uncertainty	Does the model exist	Uncertainty	Does the model exist	Uncertainty	Does the model exist	Uncertainty
1ϕ Liquid Convective Heat Transfer	L								
Turbulent Forced Convection		Dittus-Boelter	30%	Dittus-Boelter	30%	Dittus-Boelter	30%	Yes, max of Dittus-Boelter or FLECHT-SEASET	15%
Laminar Forced Convection		Kays	10%	Kays	10%	Nu = 4	50%	Yes, Sparrow	50%
Effects of Geometry	L	P/D correction	H	No		No, for bundle can under predict HTC by 40%.	40%	Yes, in FLECHT-SEASET Correlation	15%
Effects of Spacers	L	Input grid loss		Input grid loss		Input grid loss		Yes, convection enhancement added, input grid loss	15%
Effects of Properties	L	Yes code calculated		Yes code calculated		Yes code calculated		Yes, code calculated	
1ϕ Liquid Natural Convection Heat Transfer	L	Churchill and Chu	L	McAdams	15%	Holman	~20%	Yes, McAddams	15%
Effects of Geometry	L	No		No		No		No	

Effects of Spacers grids	L	Input grid loss No H.T. effect	20%						
Effects of Properties	L	Yes code calculated		Yes code calculated		Yes code calculated		Yes, code calculates	
Decay Power	H	Input		Input		Input		Input	

Although it is not given a ranking of high, convective heat transfer for the single phase convective experiments is of interest since most of the current codes use a pipe correlation as compared to a rod bundle correlation, as seen in Table 4-6. The computer codes calculate the local convective heat transfer from the local node velocity, the fluid properties, and the given hydraulic diameter of the node. The correlations for forced convection require the code to calculate a local Reynolds and Prandtl number which depends on the the flow and temperature conditions within the computational node. In the RBHT experiment, the local power is calculated from the total power of the rods and the axial power distribution, such that the local value of the heat flux is known along the bundle. The heater rods are instrumented with 8 thermocouples which calculate the local heater rod surface temperature from an inverse conduction calculation.

There are several subchannel fluid temperature measurements along the length of the bundle. Most of the temperature measurements have the ability to traverse across the subchannel such that the temperature distribution can be obtained within the subchannel. Therefore, the local fluid temperature or subcooling will be measured directly in the experiments. The temperature traverses will have to be velocity weighted and integrated across the subchannel area to obtain the local bulk subchannel fluid temperature.

The local subchannel flow is not directly measured in the experiment, however, the total liquid flow into the bundle is measured. The pressure drop of the bundle will already have been characterized by single phase pressure drop experiments which will confirm the losses of the spacer grids as well as the frictional loss of the total bundle. The hydraulic data can be used to benchmark a subchannel computer code such as COBRA-IV or VIPRE-II which will then be used to predict the local subchannel velocity and the subchannel Reynolds number. These code calculations can be checked, for fully developed flow, with hand calculations to confirm the flow split between types of subchannels. Given the measurements of the rod heat flux, the heater rod surface temperature, and using the fluid temperature traverses and velocities predicted by COBRA-IV, the local convective heat transfer coefficient can be calculated from the data. The COBRA-IV local subchannel velocities can also be used with the fluid properties to calculate the local fluid Reynolds and Prandtl numbers such that comparisons can be made between the correlations used in the computer codes and the RBHT data to determine if the current models are adequate. This data analysis approach has been used on the FLECHT-SEASET single phase steam tests⁽⁴⁻²⁶⁾. The RBHT tests are designed to be performed over a wide range of fluid Reynolds numbers such that either a new convective correlation can be developed or an existing correlation can be confirmed.

In the case of single phase natural convection, or mixed convection, the highly ranked PIRT items include:

- natural convection heat transfer coefficient,
- effects of forced or free convection heat transfer,
- liquid velocity,
- liquid subcooling,
- decay power.

The local Reynolds and Grashoff numbers can also be calculated from the data using the same analysis approaches as given above to determine if forced convective heat transfer or natural circulation heat transfer exists within the subchannel. The ratio of the Grashoff to the square of the Reynolds will be calculated to determine if the flow is forced, free or mixed convection. For most reflood rates of interest, the convective heat transfer will be forced. If the heat transfer is free convection, a similar approach to that used for the forced convection heat transfer analysis can be used to determine the local heat transfer coefficient excepting that the local subchannel velocity will not be needed. If the convection is mixed, the data will be compared to conventional methods for mixed convection in which the forced and natural convection heat transfer coefficients are raised to a power (typically 3), summed (for aiding flow), and then raised to the inverse of the power (typically 1/3). The natural or mixed convective heat transfer coefficient is ranked higher as compared to the forced convection coefficient since there is very little data available for natural convection heat transfer in bundles.

4.3.2 Subcooled and Saturated Boiling Below the Quench Front (Table 4-7)

The heat transfer in this region ranks low in the PIRT but it determines the degree of subcooling at the quench front location, which in turn affects the ranking processes in that region. The Chen⁽⁴⁻⁴⁾ correlation is used in the codes to determine the heat transfer in the subcooled and saturated boiling regimes. In experiments the total heat transfer to the fluid in the two-phase region is measured while the codes need to calculate the heat transfer to each phase separately. Once the heat input in each phase is calculated the interfacial heat and mass transfer terms provide the closure to the equations. The subcooled boiling is modeled as follows:

- 1) convection to the liquid
- 2) vapor generation at the wall
- 3) vapor condensation near the wall
- 4) subcooled liquid 'pumped' into the thermal boundary layer.
- 5) bulk condensation (subcooled liquid core)

The fraction of vapor not condensing near the wall represents the net vapor generation term which is added explicitly into the mass-energy conservation equations. The condensation of the vapor because of the presence of vapor in the liquid core is calculated implicitly during the solution of the energy equation and it does not affect the determination of phasic heat inputs.

The convection to the liquid is calculated starting from the liquid phase Reynolds number. The code needs the local liquid bulk temperature, the local flow quality and flowrate velocity. The nucleate boiling component of the Chen correlation defines the amount of heat available to cause vapor generation at the wall. A fraction of this vapor condenses near the wall, the rest will condense in the liquid core. The near-wall condensation is determined by the conditions (flow and thermal) of the fluid near the wall while the bulk condensation is determined by the

**Table 4-7 Subcooled and Saturated Boiling
The Core Component Below the Quench Front**

<u>Process/Phenomena</u>	<u>Ranking</u>	<u>RELAP5/MOD3.2</u>		<u>TRAC-B</u>		<u>TRAC-P</u>		<u>COBRA-TF</u>	
		Does the model exist	Uncertainty	Does the model exist	Uncertainty	Does the model exist	Uncertainty	Does the model exist	Uncertainty
Subcooled Boiling	L	Yes, Chen correlation	+180 -60%	Yes, Chen correlation	+180 -60%	Yes, Chen correlation	+180 -60%	Yes, Chen	+180, -60%
Effects of Geometry, P/D, De	L	Inayatov eq. (P/D)	H	No		No		No	
Effects of Spacers	L	No, H.T. effect		No, H.T. effect		No, H.T. effect		No, H.T. effect	
Effects of Properties	L	Input		Yes, code calculates		Yes, code calculates		Yes, code calculates	
Local Void Fraction (Interfacial Heat Transfer)	H	Yes code calculates interfacial area and H.T.C (see table 4.1-1)	20% for Bubbly Flow	Yes, code calculates interfacial area and HTC		Yes, code calculates interfacial area and HTC	25% for Bubbly Flow	Yes, Hancox, Rouhagi models, see Table 4- for interfacial H.T.C. and area	
Saturated Boiling	L	Chen	12%	Yes, Chen	12%	Yes, Chen	12%	Yes, Chen	12%
Effects of Geometry, P/D, De	L	Inayatov eq. (P/D)	H	No		No		No	
Effects of Spacers	L	No H.T. effects		No H.T. effects		No H.T. effects		No H.T. effects	

Effects of Properties	H	Yes, code calculates							
Local Void Fraction (slip flow)	H	Yes, code calculates Slip							

interfacial heat transfer. Detailed void fraction measurements, void distribution, and liquid temperature during separate steady-state subcooled boiling tests should provide the information needed to assess these models.

For example, during subcooled boiling experiments, the contribution of the near wall condensation combined with the effect of subcooled liquid 'pumped' into the thermal boundary layer can be calculated from an energy balance if the transverse temperature distribution of the liquid in the subchannel is measured or estimated.

Information about void fraction distribution (bubble size distribution and bubble location) are needed to estimate the interfacial heat transfer area. Measurements or estimates of bubble velocity can be used to estimate the interfacial drag. Note that the interfacial heat transfer and interfacial drag, which determines the condensation of steam in the liquid core and the slip between the two phases, rank high in the PIRT.

During saturated boiling, condensation does not take place. The code divides the total heat transfer rate in two contributions. The first is the heat removed by liquid convection, the second is the heat removed by boiling. Both components are from wall-to-liquid. Since metastable states are essentially not permitted in the code, energy absorbed by the liquid at the wall is transformed into vapor generated at the vapor-liquid interface with an artificially large interfacial heat transfer coefficient. Boiling at the wall enhances the near-wall convection. This is modeled in the Chen correlation with the Reynolds number factor which is a function of the local quality. The effect of the Reynolds number is also to prevent/suppress boiling and this is accounted by the suppression factor in the nucleate boiling heat transfer component of the Chen correlation.

Similarly to the subcooled boiling regime, the code evaluates the flow rate, the quality, the temperature of the liquid and the temperature of the wall to calculate the heat transfer. The temperature of the liquid is at saturation. The interfacial heat transfer is not a key in this case because the liquid superheat is prevented numerically in the code and all the energy going to the liquid is converted in vapor generation.

Separate steady-state boiling experiments with a detailed measurement of void fraction can be used to assess the model in this region. The separate effect of the Reynolds number factor and the boiling suppression factor can be quantified in these experiments. Finally bubble velocity measurements and transverse void distribution, can be used to estimate the interfacial drag.

The PIRT table for the subcooled and saturated boiling regions are given in Tables 2-2 in Section 2. The important phenomena identified in these tables include:

decay power,

local void fraction,

interfacial area and heat transfer,

liquid subcooling.

As discussed above, decay power is a test boundary condition and is known. Local void fraction is measured using finely spaced differential pressure cells as well as using an X-ray attenuation technique. The liquid subcooling is measured using traversing temperature rakes at several different elevations in the bundle. These miniature thermocouples will traverse across the bundle between the heater rods and will measure temperature in the rod-to-rod gap, as well as at the center of the subchannel.

Several different computer code models interact to develop the local void fraction within a computational node in the case of subcooled boiling. Models for vapor generation, interfacial heat transfer such as condensation of the generated bubbles (if the liquid flow is subcooled), single phase convective heat transfer at the wall, criteria for wall voidage, bubble size at departure and interfacial drag all influence the resulting void distribution in the rod bundle for subcooled and saturated boiling below the quench front.

In the RBHT program, the total wall heat flux will be determined from the power applied in the test and the axial power shape as well as from the inverse conduction calculations using the measured heater rod temperature and the power. The local fluid temperature will be measured at many elevations using the traversing miniature thermocouples in the bundle which will indicate if the bulk liquid flow is subcooled or saturated. The axial behavior of the liquid temperature in the bundle can be measured such that the location of where the bulk flow becomes saturated can be determined.

The wall heat flux consists of two components; a direct convective component and a boiling component in similar manner as the model by Chen⁽⁴⁻⁴⁾. The axial fluid temperature distribution reflects both the wall convection heat transfer as well as the condensation of the voidage generated at the wall. If one assumes that the convective and boiling processes are separate and are additive (similar to Chen's model), the wall convective heat transfer can be estimated from the bulk flow conditions as well as the portion of the heat flux which is due to convection. Since the total wall heat flux is measured, the difference between the total and the convective heat fluxes is the boiling component. This is an estimate since the local liquid phase velocity distribution will be different at the wall because of the bubble formation.

Low void fractions, characteristic of nucleate boiling, will be very difficult to measure even with sensitive differential pressure cells. The laser illuminated digital camera system can detect the voidage but it may be difficult to quantify wall voidage since the bubbles will adhere to the heated surface. As subcooling of the bulk flow is reduced, the fraction will grow and the bubbles will depart from the wall and will be condensed in the bulk flow. This can occur for voids of approximately 20 percent. In this situation, the finely spaced differential pressure cells data can be analyzed to obtain an average void over the cell span with more confidence. Also, the laser illuminated camera system can also be used to obtain data on the bubble diameter and velocity distributions, for low voidage flows in which there is minimum bubble interaction.

A measurement of the local void will also be obtained using an X-ray source, photoelectric cell and a digital camera. Given the void distribution, the bubble diameters and velocities, estimates of the product of the interfacial heat transfer and the interfacial area can be made. Therefore, the computer code models and correlations for the product of the interfacial hA_i can be compared to the estimates of the hA_i estimates from the data. It is expected that the uncertainties will be large. Both the axial liquid temperature gradient as well as the void fraction (which represents a net situation, that is the void generation minus the condensation) can also be used to develop and refine models for the interfacial heat transfer and area.

When the liquid reaches saturation, all the energy from the heater rods generates vapor since there is no longer any liquid subcooling. In this case saturated boiling is occurring on the heater rod surfaces and the void fraction increases. The important items from the PIRT Table 2-2 for this case are:

Void fraction,
Decay power

The void fraction in this region is ranked high since it will influence the steam velocity at the quench front and the generation of liquid entrainment. The decay power is ranked high since it represents the energy input into the fluid which will generate steam. The saturated boiling heat transfer coefficient is not ranked as a high since a large uncertainty in its value will not effect the peak cladding temperature. Note that there is an overlap between the decay power and the boiling heat transfer coefficient since all the energy generated in the rod is transferred to the fluid. If the decay power is ranked as a "high", in reality, the surface heat transfer coefficient is also a high.

The void distribution will be determined using the finely spaced differential pressure cells which will result in a node average void along the axial length of the bundle. In addition, an X-ray technique will be used to obtain the void distribution at specific axial locations to confirm the values obtained from the differential pressure cells.

4.3.3 Quench Front Behavior (Table 4-8)

This is the most complex region in the bundle. There are several process taking place across the quench front which rank high in the PIRT table. This is also the most difficult region to simulate with the codes because a big transition in the thermal-hydraulic conditions is experienced in a small portion of the computational domain. Moreover the hydraulic process is strongly coupled with the thermal behavior in this region. The froth region behavior determine significantly the heat transfer downstream in the film boiling region. This is where compensating errors most likely occur. The code has to be able to handle each separate process accurately to limit to a minimum extent the effect of compensating errors. Unfortunately the lack of data in this region causes the models to simulate this region poorly in most of the codes. Essentially, the codes need to calculate heat transfer from the rod to the fluid, vapor generation and entrainment. The

Table 4-8 Quench Front Behavior in the Core Component

Process/Phenomena	Ranking	RELAP5/MOD3.2		TRAC-B		TRAC-P		COBRA-TF	
		Does the model exist	Uncertainty	Does the model exist	Uncertainty	Does the model exist	Uncertainty	Does the model exist	Uncertainty
Fuel /Heater Rod Quench									
Fuel/heater rod materials, ρ , C_p , k , rod diameter	H	Input		Input		Input		Input	15%
Gap heat transfer coefficient	M	FRAP-T6 ⁽¹⁾	~100%	Yes, user specified	~100%	Yes, user specified	~±100%	For plant gap HT is adjusted to match plant calc's	~100%
Cladding materials, ρ , C_p , k	L	Input		Input		Input		Input	
Cladding surface effects	H								
• Oxides		No		No		No		Input	
• Roughness		No		No		No		No	
• Materials		Input		Input		Input		Input	
• T_{min}		Yes, code calculates		Yes, homogen. nucleation, Shumay		Yes, Nelson model		Yes, Henry Homogeneous Nucleation	
• T_{CHF}		Yes, code calculates		Yes, Baisi CHF and Chen		Yes, Baisi CHF and Chen		Yes, Zuber CHF, and Chen	

Transition Boiling Heat Transfer	H	Chen	16%	Yes, $T_w - T_{Min}$ temperature weighting of nucleate and film boiling.		James and Bankoff:: composition of nucleate and film boiling weighted with wet versus dry wall.		Yes, $T_w - T_{Min}$ Weighting of nucleate and film boiling.	
Steam generation at quench front (interfacial H.T.)	H	Yes code calculates interfacial area and H.T.C. depending on flow regime		Yes, interfacial H.T. depend on Flow Regime		Yes, interfacial H.T. depend on Flow Regime		Yes, interfacial H.T. depends on Flow Regime Both Hot and Cold wall regime	
Decay Power	H	Input		Input		Input		Input	
Liquid entrainment at quench front which includes liquid ligaments, initial drop size, and droplet number density	H	Entrainment is calculated for the annular film flow regime)		Ishii model used for all flow regimes		Entrainment calculated for annular flow by Ishii and Mishima		Uses droplet correlation based on Flecht data and drop force balance.	
Void fraction/flow regime	H	Yes, has Flow Regime logic		Yes, has Flow Regime logic		Yes, has Flow Regime logic		Yes, has cold wall and hot wall flow regime logic	
Interfacial area	H	Yes calculated for non-equilibrium	100%	Yes, code calculates flow regime dependent	100%	Yes, code calculates flow regime dependent	100%	Yes, calculated for non-equilibrium situations. Flow Regime dependent, has hot and cold wall F.R.. Has interfacial are transport equation	50%

(1) - L.J. Sierken et al.. FRAP-T6 - A computer code for the transient analysis of oxide fuel rods, EGG-CDAD-5410, April 1981.

amount of droplets entrained in that region will determine the heat transfer downstream, in the dispersed flow region.

The codes at first calculate T_{CHF} and T_{MIN} , and if the clad temperature falls between those two values transition boiling regime is assumed. The heat transfer selection logic of COBRA-TF is shown in Figure 4-15. The present version of COBRA-TF does not have a transition boiling model and the heat transfer is calculated by extrapolating the dispersed flow film boiling heat transfer or the inverted annular film boiling heat transfer in that region. The models used by other codes are described in Section 4.2. A more accurate transition boiling model and a more consistent entrainment model need to be developed during the RBHT program.

Critical Heat Flux and T_{MIN} are calculated by different codes using different correlations as described in Section 4.2. In the transition boiling regime the codes calculate the total heat transfer as the sum of convective heat transfer from the wall to the vapor, radiation heat transfer to the liquid and wall-liquid direct contact heat transfer. The radiation heat transfer is a small contribution in the froth region where the wall temperature is not very high and the void fraction is low.

The code needs to predict accurately the void fraction and the slip in this region. Therefore detailed information is needed about the void fraction distribution. An estimate of the slip is also needed and can be obtained through a mass and energy balance in the froth region when sufficient data about void fraction are available. The vapor in this region can be assumed at saturation while the liquid can be subcooled. The degree of subcooling is needed to calculate the interfacial heat transfer and net vapor generation on condensation. The void fraction distribution is also needed to calculate the radiation heat transfer component as well as to define the mechanisms of entrainment. The entrainment is a function of the vapor generation rate.

Information about the size and velocity of the entrained droplets and ligaments just above the froth region are also needed to develop a mechanistic entrainment model.

Compared to the other codes, COBRA-TF has the unique feature of a three-field approach. This is a big advantage in the froth region because continuous liquid, droplets and vapor coexist. This feature combined with proper entrainment and de-entrainment model provide a more realistic representation of the phenomena at the quench front. Data from RBHT experiments can be used to assess these separate models.

All the codes attempt to calculate the rod axial conduction at the quench front by using a fine mesh rezoning in that region. The axial conduction is a very important phenomena during reflood because it represents a flow path for the energy from the region above the quench front where the heat transfer to the liquid is low to the region below the quench front characterized by a much higher heat transfer coefficient. This component needs to be extracted during the test data analysis by solving a two-dimensional inverse conduction problem.

Other effects, such as fuel/heater rod material properties, dimensions and cladding thickness, gap heat transfer coefficient, cladding surface effects, need to be correctly simulated and measured.

The highly ranked items from the PIRT in Table 2-3 for the quench region are:

Fuel/heater rod material properties, dimensions and cladding thickness,

Gap heat transfer coefficient,

Cladding surface effects,

Transition boiling heat transfer(surface-liquid contact heat transfer),

Steam generation at the quench front,

T_{CHF} the temperature where CHF occurs (maximum limit of nucleate boiling),

T_{MIN} the temperature at the minimum film boiling point,

Surface temperature.

The heater rod physical properties such as the clad conductivity, density and specific heat are known as a function of temperature from property tables. The boron nitride filler material properties such as the conductivity, specific heat and theoretical density will be determined by Purdue University Thermal Physical Property Center such that the heater rods will be well characterized. The property and geometric information is used to calculate the surface heat flux by an inverse conduction technique using an internal thermocouple. The surface temperature is also calculated using the same method. The same information is available for nuclear fuel rods such that the differences are known. The scaling analysis given in Sections 6 and 7 addresses the differences between the nuclear and the electrically heated rods.

The gap heat transfer coefficient is very high for the heater rods since they are swagged to close the gap between the boron nitride and the inside of the cladding. A typical value of 96.875 kW/m²K (5000 Btu/hr-ft²-°F) is used to characterize this gap resistance. The gap heat transfer coefficient in a nuclear fuel rod is a dynamic quantity since it changes over the fuel lifetime as well as during the accident. While the fuel rod gap heat transfer coefficient has a large uncertainty, this uncertainty will not effect the total stored energy, since it will be released during quenching. However, the gap heat transfer can affect the rate at which this energy is released. Sensitivity calculations as well as nuclear rod data can be used to quantify these effects.

Cladding surface effects such as crud, oxide layers, roughness, material types, have been shown to effect the minimum film boiling temperature, T_{MIN} and the CHF temperature T_{CHF} . Both of these temperatures define the region of transition boiling.

The heater rod surface conditions will be well characterized by the Purdue University Thermal Physical Property Center as well as at Penn State. A nuclear fuel rod cladding, however, can have a range of surface conditions which affect T_{MIN} and T_{CHF} . Therefore, it has been proposed

that as part of the Rod Bundle Heat Transfer Program, that a series of "bench top" experiments be performed to characterize the surface effects on both T_{MIN} and T_{CHF} using small samples of different cladding materials which have known surface conditions. The end result of this effort will be to develop specific criteria for a T_{MIN} correlation and to confirm the relationship for T_{CHF} . The literature will be reviewed and relevant data for different surfaces will be found and assessed.

Transition boiling heat transfer occurs as the fraction of the heated surface which has liquid contact increases until the entire surface is wetted and quenched. The RBHT electrical heater rods are well instrumented with internal thermocouples to measure the total wall heat flux using a radial inverse conduction calculations given the power and the internal temperature. The local fluid thermocouples will measure the local subchannel fluid temperature which should be near or at the saturation temperature. As the rod quenches, the measured temperature can be influence by the axial conduction down the rod to the quench front since there is a very large axial temperature gradient near the quench front. Therefore, the calculation of the radial heat flux and the resulting heat transfer coefficient from the inverse conduction scheme must be corrected for the axial conduction when the quench front passes a thermocouple location.

Two-dimensional, transient calculations will be performed on the heater rods to predict the axial heat flow such that the data can take account of axial heat flux as the quench front approaches. The transition boiling heat transfer will then be calculated as the corrected heat flux divided by the difference of the heater rod surface temperature minus the local saturation temperature. The data sampling during this time period will be sufficiently rapid such that a number of data samples will be obtained as a particular location quenches. Similar calculations will be performed on the bench top experiments.

The values of T_{MIN} and T_{CHF} will be obtained directly from the data as the heater rod quenches. The local void fraction will also be available which can be used to determine if the liquid content in the flow has an effect on T_{MIN} and T_{CHF} . These values will be supplemented with similar data from the bench top experiments such that a material and surface condition specific transition boiling correlation could be developed. The RBHT heat transfer data can then be compared to different T_{MIN} and transition boiling correlations in the literature as well as those currently used in safety analysis computer codes.

Steam generation near the quench front is responsible for the downstream development of drops, liquid ligaments and or chunks which are entrained upward by the steam flow. The entrained liquid provides an additional heat sink for the heated surface since the drops evaporate in the superheated steam flow, generating additional steam at the saturation temperature, which cools the steam. The droplets are also a radiation heat sink for the heated surfaces. Local steam flows within the bundle are not measured. The exit steam and liquid flows are measured as well as the vapor temperature distribution along the bundle as well as the rod bundle total heat flux along the heater rod surfaces. The bundle heat flux represents the total energy leaving the heater rods. The rod bundle energy has several different paths, directly to the fluid by convection and radiation to steam and droplets, to the colder housing, to colder rods, and to the colder support tubes. The

temperatures of all the structures in the rod bundle are measured at several elevations (heater rods, thimbles, housing, spacer grids).

The radiation network used to determine the radiation heat transfer in Section 6 and 7 can be used to determine the expected radiation heat fluxes during a two-phase experiment. The radiation-only tests will be used to calibrate this method such that the radiation can be subtracted from the total measured heat flux to obtain the heat flow into the fluid.

Constructing a one-dimensional transient heat balance from the exit of the test section, using the measured vapor temperatures, the measured vapor flows and liquid flows, and the portion of the wall heat which is transferred to the fluid, the axial fluid quality can be calculated in the bundle above the quench front. This calculation can be carried to the top of the froth region, where the majority of the entrainment occurs.

The vapor temperature at the top of the froth region is superheated, however, it is expected that the miniature thermocouples will have wetted such that they will not yield an accurate reading of the true vapor temperature. The vapor superheat will be assumed to be the average of T_{SAT} and the heater rod wall temperature T_{WALL} . This approach was successfully used in the analysis of the FLECHT-SEASET data. This calculations will yield the bundle average vapor and liquid flowrates at the top of the froth region. The local subchannel vapor velocities can be estimated using COBRA-IV or VIPRE-II above the froth region assuming that the droplets do not influence the vapor flow since the void fraction is very large (0.999).

A similar transient one-dimensional energy balance calculation scheme can be written from the bundle inlet to the top of the quench front. The local fluid temperatures as well as the heater rod temperatures can be used to determine if the flow is saturated or subcooled at the quench front such that the quality or subcooling can be calculated from the inlet flow conditions and the energy input into the fluid from the rod decay power, housing, and structures, as well as the heat release at the quench front. If the fluid conditions are subcooled at the quench front, the steam generation can be calculated using the difference between the energy released and the energy needed to raise the fluid temperature to the saturation temperature. This approach is reasonable for low flooding rate cases in which the flow entering the quench front is at or near saturation.

For higher flooding rate cases, additional assumptions and approximations are required since the subchannel fluid thermocouples will wet and read the saturation temperature. For high flooding rate cases (flooding rates of 6 inches/second or larger, the subchannel thermocouples could read the liquid subcooling such that an estimate of the steam flow can be made. Also, for high flooding rate cases, the two-phase mixture temperature above the quench front is at or near the saturation temperature since steam superheats are small. Therefore, an equilibrium energy balance can be used to estimate the flow quality using the bundle exit flows and the rod energy which is calculated to go into the mixture. Highly ranked PIRT phenomena of steam generation at the quench front can be calculated from the data with reasonable uncertainty and compared to the computer code predictions.

Values of T_{MIN} and T_{CHF} can be obtained directly from the heater rod thermocouple data. T_{CHF} can be obtained from plots of the calculated wall heat flux against $T_{WALL} - T_{SAT}$ for the different heater rods. T_{MIN} can be obtained from the data by using a criteria that if the temperature change is greater than $27.8^{\circ}C/sec$ ($50^{\circ}F/second$), the heater rod is wet. The $27.8^{\circ}C/sec$ ($50^{\circ}F$) is a historical value used in the FLECHT and FLECHT-SEASET programs to estimate T_{MIN} . This value will have to be verified for the RBHT facility. However, data for both T_{CHF} and T_{MIN} can be obtained to address these PIRT phenomena.

The heater rod surface temperature is also a highly ranked PIRT phenomena as given in Table 2-3. The heater rod thermocouple directly measures temperature close to the inside cladding temperature. The outside cladding temperature is calculated from the one-dimensional inverse conduction calculation at the thermocouple location. For most of the time when the rod is in film boiling, the measured inside temperature and the calculated outside temperature are nearly identical since the heat flux is very low. Immediately near the quench front, the data have to be corrected for two-dimensional effects due to the axial conduction. In either case, the RBHT facility will provide data on the surface temperature which is a highly ranked PIRT phenomena for the quench period.

The decay power, which is ranked as a high in the PIRT, will be directly simulated in the experiments over a range of powers.

Liquid entrainment at the quench front is also ranked high in the PIRT. Liquid entrainment begins at the quench front by the formation of liquid chunks, ligaments, and drops. The liquid chunks and ligaments are sheared by the high steam velocity into small particles which are then entrained as droplets at the top of the froth region. Large liquid chunks or pieces will fallback and will be sheared until they are small enough to be entrained. The bundle energy balance calculations described earlier will give the flow quality at the top of the froth region such that the bundle average liquid and vapor flowrates can be calculated from the test data. FLECHT-SEASET reflood tests indicate that the froth region thickness is approximately constant over most of the rod bundle as it refloods. Therefore, the liquid mass stored in the froth region is a constant such that the liquid flow at the top of the froth region is approximately the same as the liquid flow at the quench front. This is particularly true for lower flooding rate conditions. Using the analysis of the test data, the liquid entrainment at the quench front can be determined in the RBHT tests.

The void fraction and flow regime are also ranked high in the reflood PIRT for the quench region. The void fraction will be directly measured in the quench region using sensitive differential pressure cells with a three-inch span such that more detailed void measurements can be made as the quench front advances upward through the bundle. An X-ray attenuation technique will be used to obtain the transient chordal-average void fraction along the center plane of the bundle to obtain a time dependent void fraction. The local flow regime can also be photographed using high speed cameras or videotaped to infer the flow regime in the quench region, provided the test section windows have a minimum of wetting. Therefore, these highly ranked phenomena can be measured in the RBHT facility.

Interfacial area is also ranked high for the quench region since it effects the interfacial drag and interfacial heat transfer. There is no direct measurement of the interfacial area in the experiments. The void fraction will be measured and the liquid and vapor flowrates will be calculated from the data such that the phase velocities can be determined from the data. High speed photography can be used to infer the flow regime and hence the interfacial area. Therefore, this highly ranked PIRT phenomena can not be measured in the RBHT tests, but can be inferred from photography.

The local fluid temperature is also a highly ranked PIRT phenomena in the quench region. The miniature fluid thermocouples which are located at different axial positions in the rod bundle will measure the liquid temperature. Liquid subcooling, if present, may be difficult to measure since most of the liquid will be at the saturation temperature for most cases. When the liquid flowrate is large combined with large liquid subcooling, the subcooled liquid temperature will be more accurately measured. Therefore, for the cases when subcooling is important, the RBHT facility can measure this highly ranked PIRT phenomena.

4.3.4 Two-Phase Froth Region for the Core Component (Table 4-9)

The PIRT given in Table 2-4 from Section 2 indicates that several of the phenomena are highly ranked in this region. The froth region can be described as the region in which a transition is occurring between the continuous liquid or low void fraction mixture at and below the quench front; to a continuous vapor region with entrained liquid approximately one foot above the quench front. The void fraction changes very sharply from typical values of zero to 20 percent near the quench front to 0.99 or higher at the top of the froth region. The sudden change in the void fraction is the result of the large steam generation at the quench front as discussed earlier. It is this steam generation and the resulting film boiling heat transfer in the froth region which provides the large steam velocity needed to shear and entrain the liquid upward in the rod bundle. The wall temperatures in the froth region is above the wetting temperature such that the heated surfaces are in film boiling. The film boiling heat transfer in this region has been shown to correlate well with the local void fraction. The phenomena which are highly ranked include:

Void fraction/flow regime

Liquid entrainment

Liquid ligaments, drops sizes, number density, interfacial area

Film boiling heat transfer

Decay power

Table 4-9 Two-Phase Froth (Transition) Region for Core Component

Process/Phenomena	Ranking	RELAP5/MOD3.2		TRAC-B		TRAC-P		COBRA-TF	
		Does the model exist	Uncertainty	Does the model exist	Uncertainty	Does the model exist	Uncertainty	Does the model exist	Uncertainty
Void fraction/flow Regime	H	Yes, has Flow Regime logic		Yes, has Flow Regime logic		Yes, has flow regime logic		Yes, has more detailed flow regime logic	
Liquid entrainment	H	Ishii and Mishima		Ishii and Mishima		Ishii and Mishima		Force balance on drop, empirical model based on FLECHT data	
Liquid ligaments, drop sizes, interfacial area, droplet number density	H	Yes, Single liquid field, single drop size		Yes, single liquid field, drop size		Yes, single liquid field, drop size		Yes, has separate drop field, can treat two drop sizes	
Film Boiling H.T. at low void fraction classical film boiling	H	Bromley void weighted	25%	Modified Bromley, void weighted, max of pool Film Boiling and vapor convection		Modified Bromley correlation (Denham)		Bromley void weighted	25%
droplet contact heat transfer	H	No		No		No		Yes, has Ganic and Rohsenow	100%
convective vapor H.T.	M	Dittus-Boelter	30%	Dittus-Boelter	30%	Yes, max of Doughall-Rohsenow and Dittus-Boelter		Max Dittus-Boelter or FLECHT-SEASET ¹	25%

interfacial H.T.	M	Yes code calculates interfacial area and H.T.C. depending on flow regime		Yes code calculates interfacial area and H.T.C. depending on flow regime		Yes code calculates interfacial area and H.T.C. depending on flow regime		Yes, code calculates interfacial area using hot wall flow regime and interfacial heat transfer	
radiation H.T. to liquid/vapor	M	Yes, with modified Bromley film boiling		Yes, with modified Bromley film boiling		Yes, with modified Bromley film boiling		Yes, with Bromley Film Boiling	
effects of spacers	M	No		No		No		Yes, if $\alpha > 0.9$ considers convection, rewetting droplet breakup	
Decay Power	H	Input		Input		Input		Input	

The components of film boiling heat transfer include the classical film boiling such as Bromley as well as drop contact heat transfer, vapor convection heat transfer as well as interfacial heat transfer and radiation heat transfer.

Void fraction and flow regime are ranked high in the PIRT for this region. Void fraction will be measured using the finely spaced differential pressure which should be accurate since the void is lower in this region. The local void can also be measured at a fixed point as the froth region passes through the location where the X-ray attenuation system is located. If there is significant vapor superheat, it may be detected by the miniature thermocouples, however, since the void fraction is lower in the froth region as compared to the dispersed flow region, it is expected that the thermocouples will wet and will indicate the saturation temperature. The flow regime in this region is difficult to quantify, however, high speed photography can be used to indicate the features of the flow regime. Also examples of the froth flow region exist in the FLECHT and FLECHT-SEASET high speed movies. Therefore, the RBHT program can obtain the data needed for these PIRT phenomena.

Liquid entrainment is one of the most highly ranked phenomena in the reflood PIRT since it directly determines the peak cladding temperature downstream of the froth region. The mass flowrate of the entrained liquid can be calculated, on an bundle average basis, using the energy and mass balances described earlier from the exit mass flow measurements, vapor temperatures, and the heat flux into the fluid. In the RBHT facility, additional effort has been made to design a closely coupled liquid collection tank such that the delay time from the beginning of entrainment to the detectable liquid measurement out of the bundle is minimized. Estimates of the liquid velocity can also be made using a mass and energy balance from the bundle inlet, accounting for the quench energy and the measured void fraction.

The characteristics of the entrained liquid in the froth region is also a highly ranked PIRT phenomena. Parameters such as liquid ligaments, drop size, interfacial area, droplet number density and droplet velocities, are all highly ranked phenomena which directly effect the resulting peak clad temperature. The drops sizes and velocities will be measured by the Laser Illuminated Digital Camera system near the top of the froth region. As the froth region approaches the measurement point there may be too much liquid for the laser system to properly determine the sizes and velocities. However, if there is a significant amount of liquid present, the finely spaced differential pressure cells will provide an accurate measurement of the void fraction as the froth region passes within the span of the cell. The behavior of the froth region was also measured in the FLECHT-SEASET experiments.

Film boiling heat transfer will be measured at many locations along the length of the electrical heater rods in the bundle. The heater rod thermocouples have been placed such that they are located at or very near the center of a differential pressure span such that the average void fraction determined from the differential pressure span can be used to correlate the resulting film boiling heat transfer. The data can be corrected for radiation heat transfer assuming that the radiation is to a liquid rich two-phase mixture within the froth region.

Radiation heat transfer can be void fraction weighted and subtracted from the total measured heater rod heat transfer. Estimates can also be made of the convective heat transfer to the vapor using the single phase heat transfer correlation which was developed earlier in the program as well as the wall and vapor temperature. Use of such a correlation assumes that the presence of the liquid has a small effects on the local velocity and temperature profiles in the steam near the wall. As the void fraction decreases, this assumption becomes invalid and the correlation will be suspect. However, for very low void fractions in the froth region, the vapor will be concentrated at the wall in a traditional inverted flow film boiling situation. The local vapor temperature measurements may also be very uncertain since the miniature thermocouples can easily wet in the froth region and will indicate only the saturation temperature, not superheat temperature such that the true vapor temperature is underestimated resulting in an over-estimate of the convective heat flux. Care will have to be used in the interpretation of these results.

Another component of the heat transfer in the froth region is direct drop-wall contact heat transfer. This individual heat transfer component is zero when the surface temperature is above the minimum film boiling temperature, T_{MIN} , and increases as the surface temperature decreases. Drop contact correlations are usually expressed as a exponential of the surface temperature which calculates a multiplier which is then applied to a nucleate boiling flux. The drop contact heat transfer cannot be measured directly in the Rod Bundle Heat Transfer facility because of the highly turbulent nature of the flow and the advancing quench front along the heater rods. The contribution of the drop contact heat transfer is accounted for in the film boiling and transition boiling heat transfer which is calculated from the measured heater rod surface temperatures and power using the inverse conduction technique, however, the precise portion of the total heat transfer attributed to drop contact cannot be separated from the total with confidence. If additional detail is needed on this phenomena, a bench top experiment would be useful such that only the effect of the drop contact heat transfer is present. The resulting data could then be correlated into a model.

Vapor convection heat transfer is also an important PIRT phenomena for the froth region. In this situation, the vapor is generated as a very rapidly growing film along the walls of the heater rods and then mixes with the large chunks, drops, and ligaments of liquid which are being accelerated in the froth region. The bundle average vapor flow rate can be calculated from the bundle mass and energy balance and the bundle average vapor velocity can be calculated from the measured void fraction. Measurement of the vapor superheat is uncertain.

The measurement scheme is to use miniature bare thermocouples which point into the flow. In the liquid rich froth region, there is a high probability that the thermocouples will be wetted by the liquid which is being entrained in the flow. Therefore, the miniature thermocouple probes will read the saturation or liquid temperature most of the time. For very low void fraction mixtures within the froth region, one could expect that the vapor superheat would be at or near the saturation temperature because of the large interfacial heat transfer and the lower mass flow of the vapor. As the void fraction increases within the froth region, one could expect that the vapor temperature is between the heater rod surface temperature and the local saturation temperature such that some vapor superheat exists.

The vapor superheat data for a given test will be plotted as a function of axial position to investigate how to extrapolate the data into the froth region. This has been done in the previous FLECHT-SEASET experiments with some success. Knowing the vapor temperature, and velocity (from the energy balance and the vapor temperature), the vapor Reynolds number and a single phase convective heat flux can be calculated. Since this situation is single phase convection in a two-phase mixture, correlation is developed from droplet injection experiments. This type of a calculation will give a reasonable estimate of the portion of the total wall heat flux which is due to convection.

Heat transfer by radiation is also an important phenomena in the froth region because of the large liquid content of the flow and the increasing heater rod surface temperatures. However, the percentage of the total heat flux due to radiation should be relatively small since the majority of the heat is transferred directly by film boiling to the low void fraction mixture. The radiation heat transfer to the liquid can be estimated for the test conditions using the void fraction and high speed movies which indicate the behavior of the liquid using the measured surface temperature and the saturation temperature. Similar calculations can be performed for radiation to the vapor using the estimated vapor temperature and the heater rod surface temperature. Again, it is expected that the total effect of radiation heat transfer is small for the froth region since the absolute value of the film boiling heat transfer is much larger in this region. The radiation modeling approach has been used in the FLECHT-SEASET program and would be modified for the RBHT facility.

As liquid is entrained and accelerated in the froth region, both interfacial shear and heat transfer occur. Models for both of these important processes are crude, at best. The interfacial area and interfacial shear are not measured directly; however, estimates of the interfacial drag (shear) times the interfacial area can be made from the data. The local quality can be calculated from a detailed mass and energy balance on the bundle, particularly in the froth region. The principal uncertainty in this calculation is the vapor temperature.

Void fraction is also measured such that the average liquid velocity in the rod bundle can be calculated. Also, by the same calculation, the average vapor velocity in the bundle can be determined at different axial locations, within and above the froth region. At this point, one would have to make assumptions which can significantly effect the calculated results. If a two-phase frictional pressure drop modal is assumed, and set equal to the portion of the measured pressure drop which is believed to be caused by friction, a measure of the product of the interfacial drag and area can be calculated. Another approach is to review the high speed movies in the froth region and postulate a liquid surface area and then calculate the resulting drag.

In the case of interfacial heat transfer, the change in the local quality within the froth region will indicate the product of the interfacial heat transfer coefficient times the interfacial area. The uncertainty in this calculation is the accuracy of the measured vapor temperature. Heat transfer should be a two-step process with the wall energy being transferred to the vapor, and the resulting vapor energy causing evaporation of the entrained liquid. The axial dependence of the measured vapor temperature will have to be extrapolated into the froth region from the dispersed flow film boiling region, using the miniature thermocouples, to obtain an estimate.

To separate the heat transfer coefficient from the interfacial area, further assumptions must be made such as characterizing the liquid surface in the froth region from high speed movies, or applying an appropriate convective coefficient to the entrained liquid. Both methods are approximate and have large uncertainties but will be examined. The different models in a computer code can be compared to the data for void fraction in the froth region, and mass balance on the froth region to obtain the entrained liquid flow. The energy balance will give the bundle average liquid and vapor velocities. A computer code should match these measured and calculated quantities from the data with their particular interfacial models.

4.3.5 Dispersed Flow Film Boiling Region (Table 4-10)

In the dispersed flow film boiling region the total wall-to-fluid heat transfer is calculated by the codes as the sum of the following contributions:

- 1) Forced convection to the vapor
- 2) Radiation heat transfer to both drops and steam
- 3) Drop direct and dry wall contact heat transfer.

The forced convection heat transfer is calculated with the Dittus-Boelter correlation by knowing the vapor Reynolds number. The vapor Reynolds number is a function of the vapor velocity, the void fraction and the vapor temperature. Some dispersed flow experiments have shown that the interfacial shear between dispersed particles and a continuous phase increases the turbulence level and enhances the convective heat transfer.

In the COBRA-TF code, this two-phase enhancement factor is approximated by an extension of the analogy between wall shear stress and heat transfer. From the momentum-heat transfer analogy, the turbulent convection heat transfer coefficient is proportional to the square root of the shear stress. The total shear stress for the two-phase is the sum of the vapor-wall shear stress and the interfacial stress due to the droplets. The ratio between the interfacial shear stress due to the droplets and the vapor-wall shear stress is a function of the vapor velocity, interfacial area the droplet velocity and the entrainment phase void fraction. These quantities can be estimated from the test data such that this effect can be quantified.

The temperature of the vapor is determined by the interfacial heat transfer and the convection from the wall. Information about the drops velocity and size distribution and the vapor temperature are also needed to estimate the interfacial heat transfer. Using steady-state droplet injection experiments, by measuring the shift in the drop size distribution as the droplets move along the channel, it may be possible to estimate the droplet evaporation rate and therefore the interfacial heat transfer.

Radiation heat transfer from wall-to-wall, wall-to-vapor, and to drops need to be analytically estimated and separated from the total heat transfer during test data analysis.

Table 4-10 A Dispersed Flow Region for Core Component

Process/Phenomena	Ranking	RELAP5/MOD3.2		TRAC-B		TRAC-P		COBRA-TF	
		Does the model Exist	Uncertainty	Does the model exist	Uncertainty	Does the model exist	Uncertainty	Does the model exist	Uncertainty
Decay Power	H	Input		Input		Input		Input	
Fuel Rod/Heater Rod properties, ρ , C_p , k	L	Input		Input		Input		Input	
Dispersed Flow Film Boiling	H	Bromley correlation for conduction across the film	18%	Modified Bromley void weighted single phase convection		Yes, modified Bromley correlation (Denham)		Yes, Sum of several individual models	
Convection to superheated vapor	H	Dittus-Boelter	30%			Yes, based on Webb-Chen correlation	Not verified for rod bundle	Yes, max of Dittus-Boelter and FLECHT-SEASET	15%
Dispersed phase enhancement of convective flow	H	No		No		Yes, somehow considered in the Webb-Chen correlation	100%	Yes, empirical correlation	>100%
Direct wall contact H.T.	L	No		No				Yes, Ganic-Rohsenow	>100%
Dry wall contact ⁽¹²⁾	M	No		No				No	
Droplet to vapor interfacial heat transfer	H	Yes, code calculates interfacial area and H.T.C. depending on flow regime		Yes, code calculates interfacial area and H.T.C. depending on flow regime		Yes, code calculates interfacial area and H.T.C. depending on flow regime		Yes, Lee Ryley model	30%

Radiation Heat Transfer to:									
• Surfaces	M/H	No		Yes, has rod and channel radiation models		No		Yes, surface radiation model	20%
• vapor	M/H	Yes, Sun Gonzales, Tien.	50%	Yes, Sun, Gonzales, Tien		No		Yes, Sun Gonzales, Tien	50%
• droplets	M/H	Yes, Sun Gonzales, Tien	50%	Yes, Sun, Gonzales, Tien		No		Yes, Sun Gonzales, Tien	50%
Gap heat transfer	L	FRAP-T6		Yes, code calculates		Yes, code calculates		Yes, does have dynamic gap	100%
Cladding Material	L	Input		Input		Input		Input	
Reaction Rate	M	No		Yes, Cathart, Powell		Yes, code calculates		Yes, Cathart Powell model	
Fuel Clad Swelling/Ballooning	L	No		No		No		Not in current version	

The third component is the most difficult to estimate from the test data. Fortunately this component rank low-medium in the PIRT. In COBRA-TF, direct wall heat transfer is a function of the deentrainment rate and the drop evaporation efficiency. The deentrainment rate is a function of the droplets concentration gradient (the concentration is zero at the wall) which is a function of the average entrainment fraction. The drop evaporation efficiency is a function of the wall superheating. The code need information about the entrainment volume fraction, drop concentration gradient and wall temperature to estimate this component.

When the direct contact heat transfer becomes important (mostly in transition boiling), the intermittent wetting of the surface should produce localized oscillations in the temperature at the surface. These oscillations could be capture if the thermocouples response time is fast enough. The analysis of the oscillation can be an indirect way to estimate this component.

The dispersed flow film boiling region is a region of very low heat transfer located above the froth front in which the mixture consists of highly superheated steam in which small liquid droplets are entrained. The peak cladding temperature is calculated in this region and the temperature remains elevated until the froth region approaches the peak temperature axial position within the rod bundle. The important PIRT phenomena for this region are given in Table 2-5 as:

Decay power,

Dispersed flow film boiling, which consists of:

Convective heat transfer to superheated vapor flow,

Dispersed phase enhancement of convective flow and heat transfer,

Radiation heat transfer to drops, vapor and surfaces,

Interfacial heat transfer between drops and superheated vapor,

Interfacial drag between drops and superheated vapor,

Dry wall drop-contact heat transfer.

The decay power will be simulated and measured as a test condition and will be ranged over typical power values expected in a nuclear power plant.

The measurement methods used in the RBHT have been developed specifically for the dispersed flow film boiling regime since it is the most limiting region of the reflood process. The Laser Illuminated Digital Camera System (LIDCS), will be used to measure the drop size and velocity at different location along the bundle. The actual flow quality will be calculated from the bundle mass and energy balance such that the bundle average flow rates for the vapor and the liquid can be obtained. Since the vapor velocity can be calculated (accounting for the vapor superheat), and

the droplet velocity and quality are known, the local void fraction can be calculated. The local void fraction can also be estimated from the droplets measurements taken with the LIDCS. However, the LIDCS measurements can over-estimate the void fraction since the measurement does not record droplets which are behind the heater rods since the measuring volume is the gap between the rods.

A separate series of convective heat transfer experiments over a wide range of Reynolds numbers is planned as one of the first test series, before the actual reflood experiments. These tests will be analyzed on a subchannel basis using COBRA-IV, VIPRE-II, as well as hand calculations, to obtain the local subchannel flow for a given measured bundle inlet flowrate. The subchannel data will be correlated both on a bundle basis as well as a subchannel basis using the bundle or subchannel Reynolds number and the Nusselt number calculated from the measured wall heat flux obtained from the heater rod thermocouples. The subchannel vapor thermocouples will be used to determine the axial vapor superheat distribution. The correlation from these experiments will be compared to existing convective correlations.

Another series of separate effects experiments will examine the effects of the dispersed entrained droplets on the convective heat transfer within the rod bundle. There are different postulated phenomena which could be occurring within the dispersed flow regime. One school of thought is that the droplets increase the total shear which increases the turbulence level in the flow such that the single phase convective heat transfer increases. Since the Reynolds are very low in superheated steam (typically 1000 to 4000), any increase in turbulence could have a significant effect.

Another thought is that the drop addition acts as a distributed heat sink within the continuous steam flow and directly effects the vapor temperature resulting in a larger temperature gradient to the wall. These and other heat transfer enhancement mechanisms will be investigated in these experiments. The local wall temperature will be measured on the heater rods to obtain the wall heat flux, the vapor temperature will be measured on a subchannel basis using the traversing miniature thermocouple probes, and the entrained droplet size, distribution, velocity and velocity distribution will be measured using the Laser Illuminated Digital Camera System. The droplet injection system will be previously characterized in a bench test, such that the initial drop size and distribution will be known. The analysis of the test data will provide a basis for the development of an improved model for these phenomena.

Separate experiments are planned to examine the surface-to-surface radiation in an evacuated bundle. The purpose to verify the data analysis program which will be used to separate the radiation heat transfer components to the surfaces, drops, and vapor, from the measured total wall heat flux such that the convective portion of the dispersed flow film boiling can be determined. Ample heater rod, structure, grid, and housing thermocouples are placed at or very near the same elevations such that a radial temperature distribution across the bundle can be obtained. These tests will also indicate the influence of the housing and the radiation to the other surfaces within the bundle. The emissivity of the surfaces will have already been determined from previous tests

to characterize the surfaces such that the surface condition uncertainty is removed from the analysis.

Radiation heat transfer components from the wall to the surfaces, drops, and vapor will be calculated from the data using the measured temperatures of the heater rods, support tubes, and housing, as well as the measured vapor temperature and the droplet temperature, which is assumed to be saturation. The uncertainty in this calculation will be reduced because the method will have been verified using radiation-only tests as well as the surface emissivity properties which were independently measured for the heater rods and surfaces. The droplet data obtained from the LIDCS will be used to determine the droplet size and area to determine the radiation from the heater rods to the drops.

Using a bundle energy balance, the local quality can be calculated along the test section. The change in the calculated quality due to the interfacial heat transfer can be obtained from the energy balance once the heat flux from the wall has been corrected for the radiation effects. The convective portion of the wall heat flux is determined from the measured value minus the radiation component. Using the energy balance data and the LIDCS data, the size and velocity of the drops are known and the number of the drops can be estimated such that the interfacial area and a droplet heat transfer coefficient can be calculated and compared to correlations used in the literature and those used in the computer codes. A similar approach can be used for the interfacial drag using the droplet information from the LIDCS and the mass and energy balance for the bundle. The above calculations from the data will be estimates since there is a droplet spectrum, not single sized droplets. The spacer grids are also postulated to shatter the entrained drops resulting in the generation of "micro" droplets which can evaporate faster. Therefore, a Sauter mean drop size will be calculated from the distribution measure and will be used in the energy calculations. This approach has been used in the FLECHT-SEASET tests with some success, although some of the uncertainties were very large.

Dry wall contact can not be directly measured in the RBHT program as a separate heat transfer contribution to the total wall heat flux. The examination of the wall convective heat flux (once radiation effects have been subtracted from the measured total heat flux) as a function of void fraction will give some guidance on the relative importance of this component. There may be double accounting of the single phase convective enhancement of the convective flow and the dry wall contact phenomena such that they are really the same since the convective enhancement should include the effects of the dry wall phenomena.

4.3.6 Top Down Quench in Core Components (Table 4-11)

None of the phenomena identified in Table 2-6 for the top down quench were identified as a highly ranked PIRT phenomena. The most important phenomena for this period is the value of T_{MIN} which will allow the quench front to propagate down the bundle. T_{MIN} appears elsewhere as a highly ranked phenomena and is discussed there.

Table 4-11 Top Down Quench in Core Components

Process/Phenomena	Ranking	RELAP5/MOD3.2		TRAC-B		TRAC-P		COBRA-TF	
		Does the model exist	Uncertainty	Does the model exist	Uncertainty	Does the model exist	Uncertainty	Does the model exist	Uncertainty
De entrainment of film flow	L ¹	No		No		No		Yes	
Sputtering droplet size and velocity	L	No		No		No		Yes, min size specified	100%
fuel rod/heater rod properties for stored energy ρ , C_p , k .	L ¹	Input		Input		Input		Input	
Gap heat Transfer	L ¹	FRAP-T6		Gas gap Code calculates		Yes, code calculates		Calculated by code	

Note: Some of these individual items can be ranked as high (H) within the top down quenching process; however, the entire list is ranked as low for a PWR/BWR since it occurs downstream of the PCT location.

4.3.7 Other Effects: Spacer Grids, Housing

The spacer grids affect the total heat transfer during the reflood by:

- 1) enhancement of convection heat transfer to the vapor
- 2) large drops are shattered by the grids
- 3) grid rewetting and deentrainment

Specific models to account of these effects are in COBRA-TF. The information needed by the code to assess these models are:

- 1) temperature of the grid
- 2) vapor temperature axial distribution (downstream of the grid)
- 3) the rod temperature axial distribution (downstream of the grid)
- 4) drop velocity and size distribution

In COBRA-TF an additional small drop field is added explicitly in the equation. The model solves the small drop acceleration and interfacial heat transfer downstream the grid once the vapor flow solution is known. Information about the small drop velocity and size distribution at different position downstream the grid can be used to validate these models.

The presence of the housing which represents a distortion of the facility if compared with the real plant, must be simulated by the code. Therefore the radiation heat transfer from the rods to the housing, the heat transfer to the fluid and the quench of the housing (stored heat) need to be characterized during the experiments.

The RBHT test facility instrumentation has been designed specifically to determine the heat transfer effects of the spacer grids. The heater rod thermocouples are spaced along the rods to determine the convective enhancement of the grids, droplet breakup effects and local subchannel vapor temperature. The grids are located within the viewing regions of the windows such that the effects of the grids can be observed and measured.

4.4 Conclusions

The different large thermal-hydraulic computer codes have been briefly reviewed and compared against the reflood PIRT tables. While each code had the basic models for a boiling curve, and thermal and mechanical non-equilibrium, the COBRA-TF thermal-hydraulic formulation and additional detailed component models makes this code an attractive choice for refined reflood development. COBRA-TF can be used on a subchannel basis to model the limiting hot fuel pin in a rod bundle. COBRA-TF is also a three-field formulation with an explicit entrained liquid field and a corresponding interfacial area transport equation which permits more accurate modeling of the entrained liquid phase, which is most important for calculating dispersed flow film boiling. Using the unique representation of the third field or entrained droplet field results in more accurate predictions of flow regimes, their transition, and the resulting heat transfer in the different regimes. There is also believed to be less chance of compensating errors, since one is not adjusting a two field model to represent the effects of three fields. Specific attention was given in COBRA-TF to the dispersed flow heat transfer model to account for the different

component models which represent reflood heat transfer. Fine mesh renodalization for the heated conductors is used to better represent the quench front. Two-phase convective enhancement is accounted for in the calculations and a subchannel radiation model is used to more accurately represent radiation within a rod bundle.

COBRA-TF also models the effects of spacer grids in dispersed two-phase flow in a mechanistic manner accounting for convective effects of spacer grids, spacer grid quenching behavior and the droplet breakup caused by spacer grids. In particular, a small-droplet field has been added to COBRA-TF to model the heat transfer effects of the much smaller drops as they evaporate and provide additional cooling downstream of the grids.

As shown in the PIRT table comparisons, the formulation of the COBRA-TF code, as developed as part of the FLECHT-SEASET 163 Blocked Bundle Program, has the desired basic formulation to develop the improved component models needed for dispersed flow film boiling in reflood. The Rod Bundle Heat Transfer program will utilize COBRA-TF for modeling purposes, and predictions and model validation purposes in the development of improved reflood models.

4.5 References

- 4-1 The RELAP5 Code Development Team, "RELAP5/MOD3 Code Manual Volume V: Models and Correlation", NUREG/CR-5535, June 1995
- 4-2 Dittus, F.W., and L. M. K. Boelter, "Heat Transfer for Automobile Radiators of the Tubular Type", University of California, Berkeley Publ. Eng, Vol. 2, No. 13, Pg 442 462, (1930).
- 4-3 S. W. Churchill and H. H. S. Chu, "Correlation Equations for Laminar and Turbulent Free Convection From a Vertical Plate", International Journal of Heat and Mass Transfer, 18. 1975, pp. 1323-1329.
- 4-4 J. C. Chen, "A Correlation for Boiling Heat Transfer to saturated Fluids in Convective Flow," Process Design and Development, 5, 1966, pp. 322-327.
- 4-5 F. D. Moles and J. R. G. Shah, "Boiling Heat Transfer to Subcooled Liquids Under Conditions of Forced Convection", Transaction, Institution Chemical Engineers, 45, 1949, p. 39.
- 4-6 L. Biasi et al., "Studies on Burnout Part 3 - A New Correlation for Round Ducts and Uniform Heating and its Comparison with World Data", Energia Nucleare, 14, 1967, pp. 535-536.

- 4-7 A. Sjoberg and D. Caraher, Assessment of RELAP5/MOD2 against 25 Dryout Experiments Conducted at the Royal Institute of Technology, NUREG/IA-0009, October 1986.
- 4-8 D. C. Groneneveld, S. C. Cheng, and T. Doan, "1986 AECL-UO Critical Heat Flux Lookup Table", Heat Transfer Engineering, 7, 1-2, 1986, pp 46-62.
- 4-9 J. C. Chen, R.K. Sundaram and F.T. Ozkaynak, A Phenomenological Correlation for Post-CHF Heat Transfer, NUREG-0237, June 1977.
- 4-10 Bromley, L.A., "Heat Transfer in Stable Film Boiling," Chemical Engineering Progress, Vol. 46, No. 5, Pgs 221-226, (1950).
- 4-11 K. H. Sun, J.M. Gonzales-Santalo and C. L. Tien, "Calculations of Combined Radiation and Convection Heat Transfer in Rod Bundles Under Emergency Cooling Conditions", Journal of Heat, 1976, pp. 414.2-420.
- 4-12 L. K. Brumfield, R. N. Houze and T. G. Theofanous, "Turbulent Mass Transfer at Free, Gas-Liquid Interfaces, with Applications to Film Flows", International Journal of Heat and Mass Transfer, 18, 1975, pp. 1077-1081.
- 4-13 K. Lee and D. J. Ryley, "The Evaporation of Water Droplets in Superheated Steam", Journal of Heat Transfer, ASME, November 1968, pp. 445-451.
- 4-14 M. S. Plesset and S. A. Zwick, "The Growth of Vapor Bubbles in Superheated Liquids", Journal of Applied Physics, 25, 4, 1954, pp. 493-500.
- 4-15 H. C. Unal, "Maximum Bubble Diameter, Maximum Bubble-Growth Time and Bubble Growth Rate During the Subcooled Nucleate Flow Boiling of Water up to 17.7 MN/m²", International Journal of Heat and Mass Transfer, 19, 1976, pp. 643-649.
- 4-16 G. Brown, "Heat Transmission of Condensation of Steam on a Spray of Water Drops", Proceedings of the General Discussion on Heat Transfer, 11-13 September 1951, published by the Institution of Mechanical Engineers, pp. 49-52.
- 4-17 T. G. Theofanous, "Modeling of Basic Condensation Processes", The Water Reactor Safety Research Workshop on Condensation, Silver Springs, MD, May 24-25, 1979.
- 4-18 M. Ishii and K. Mishima, "Correlations for Liquid Entrainment in Annular Two-Phase Flow of Low Viscous Fluid", ANL/RAS/LWR 81-2, 1981.
- 4-19 I. Kataoka and M. Ishii, "Entrainment and Deposition Rates of Droplets in Annular Two-Phase Flow", CONF-830301-11, ASME-JSME Thermal Engineering Joint Conference, Honolulu, HI, March 20, 1985.

- 4-20 Jay W. Spore, et. al., Los Alamos National Laboratory. *TRAC-PF1/MOD2, Vol. I, Theory Manual.*
- 4-21 C. Unal, K. Tuzla, C. A. Tuzla, and J. C. Chen, "Vapor Generation Model for Dispersed Drop Flow," in *ANS Proc. 1989 National Heat Transfer Conf. (August 1989), HTC-Vol. 4.*
- 4-22 I. Kataoka and M. Ishii, "Mechanism and Correlation of Droplet Entrainment and Deposition in Annular Two-Phase Flow," Argonne National Laboratory report ANL-82-44 (NUREG/CR-2885) (1982).
- 4-23 J. A. Borkowski, N. L. Wade, et.al., Idaho National Engineering Laboratory. *TRAC-BF1/MOD1 Models and Correlations*, July 1992.
- 4-24 Paik, C.Y., Hochreiter, L.E., Kelly, J.M., and R.J. Kohrt, "Analysis of FLECHT-SEASET 163 -Rod Blocked Bundle Data Using COBRA-TF," NUREG/CR-4166, WCAP- 103 75, EPRI-NP-41 11, (October 1985).
- 4-25 Thurgood, M.J. et al, "COBRA/TRAC: A Thermal-Hydraulic Code for Transient Analysis of Nuclear Reactor Vessels and Primary Coolant Systems," NUREG/CR-3046 (Volumes 1-5, (March 1982).
- 4-26 Wong, S. and L.E. Hochreiter, "Analysis of the FLECHT-SEASET Unblocked Bundle Steam Cooling and Boil-off Tests," NRC/EPRI Westinghouse Report 8, (January 1981).
- 4-27 Sparrow, E. M. et al, "Heat Transfer to Longitudinal Laminar flow Between Cylinders," *J. Heat Transfer*, Vol 83, Pg 415, (1961).
- 4-28 Hancox, W.T. and W.B. Nicoll, "A General Technique for the Prediction of Void Distributions in Nonsteady Two-phased Forced Convection," *Int. J Heat and Mass Transfer*, Vol 14, (1971).
- 4-29 Rouhani, S.Z. and F. Axelsson, "Calculation of Void Volume Fraction in Subcooled and Quality Boiling Regions," *Int. J. H Mass transfer*, Vol. 13 (1970).
- 4-30 Zuber, N. et al, "The Hydrodynamic Crisis in Pool Boiling of Saturated and Subcooled Liquids," Part II, No. 27 in *International Heat Transfer Conference*, Boulder, CO, (1961).
- 4-31 Henry, R.E., "A Correlation for Minimum Film Boiling Temperature," *AIChE Symposium Series 70*, (138), Pgs. 81-90, (1974).
- 4-32 Ganic, E.N., and W.M. Rohsenow, "Dispersed Flow Heat Transfer," *Int. J. Heat and Mass Transfer*, Vol 20, pgs 855-866, (1977).

- 4-33 McCoy, D.D., and T.J. Hanratty, "Rate of Deposition of Droplets in Annular Two-Phase Flow," *Int J. Multi phase Flow*, Vol 3, pgs 319-331, (1977).
- 4-34 Drucker, M., and V.K. Dhir, "Studies of single and Two-Phase Heat Transfer in a Blocked Four- Rod Bundle," EPRI-NP-3481, (June 1984).
- 4-35 Kays, W., Convective Heat and Mass Transfer, McGraw-Hill, New York, (1966).
- 4-36 Kelly, J.M., "Quench Front Modeling and Reflood Heat Transfer in COBRA-TF," Paper 79-WA/HT-63, ASME Winter Annual Meeting, New York, (1979).
- 4-37 Yao, S.C., Hochreiter, L.E., and W. Leech, "Heat-Transfer Augmentation in Rod Bundles Near Grid Spacers," *I Heat Transfer*, Vol 104, (1982).

5. ROD BUNDLE HEAT TRANSFER PROGRAM OBJECTIVES AND FACILITY MISSION

5.1 Introduction

Sections 2 and 3 identified the phenomena of interest and the existing database for reflood model development and validation over the range of conditions of interest. Section 2 also identified the individual component models and phenomena which a computer code uses to perform calculations for the complete heat transfer. Section 3 identified those existing data useful for addressing particular types of phenomena of importance to reflood heat transfer. Section 3 also provided information on the range of parameters to be selected for the various types of experiments to be performed in the Rod Bundle Heat transfer Program. Section 4 reviewed the different reflood heat transfer models in current computer codes and identified the current state-of-the-art needs for a best-estimate safety analysis computer code. The need for the improved analysis models becomes the objectives of the Rod Bundle Heat transfer Program. The needs define the specific mission of the test program as well as the analysis efforts which will compliment the experiments. The combination of specifically directed experiments and the corresponding data analysis, development of physically based heat transfer and two-phase flow models as well as implementation of these models into a best-estimate computer code will achieve the program objectives.

5.2 Rod Bundle Heat Transfer Program Objectives

The objective of the Rod Bundle Heat transfer Program is to provide needed, unique, separate-effects rod bundle data on specific component models which comprise the "reflood" heat transfer phenomena observed in PWR and BWR rod bundle situations for a large-break loss of coolant accident. The emphasis of the program is to provide specific experimental data and associated analysis which will enhance the understanding of the dispersed flow film boiling region which is the limiting heat transfer situation for the LOCA transient. The reflood heat transfer processes are very complex. The full range of the phenomena identified in a boiling curve occur in the reflood heat transfer calculation as well as the multi-dimensional conduction heat transfer in the fuel rod at the quench location. The rod heat transfer is coupled to the two-phase flow behavior of the coolant such that as the stored energy from the rods is released into the fluid, the local flow regime can change and continuous liquid flow, at the quench front, can be dispersed first into slugs and ligaments then sheared into dispersed droplets. The coupling of the rod heat release drives the liquid entrainment which then provides additional cooling above the quench front.

There are several different thermal-hydraulic phenomena which interact to provide the "reflood heat transfer" which best-estimate safety analysis computer codes must predict. In the dispersed flow film boiling regime, no single phenomena dominates. The total heat transfer is comprised of several different mechanisms as identified in Section 1 of this report. The relative importance of a particular mechanism will vary as the rod surface temperature increases or decreases, as the pressure varies, and as the flooding rate into the bundle changes. In dispersed flow film boiling,

the primary heat transfer mechanism is convective heat transfer to superheated steam. It is known that the steam heat transfer coefficient can be enhanced by up to 100% due to the presence of entrained droplets. No suitable models currently exist for this phenomenon.

The combination of single-phase vapor heat transfer tests with the forced droplet injection tests (where drop size and flow rate are known) will result in the development of the needed model. What is needed is a series of experiments which help isolate a particular heat transfer mechanism such that its individual effects can be identified, modeled and used to predict the total heat transfer in the bundle.

Therefore, the objectives of the Rod Bundle Heat Transfer Program are to:

1. Develop a Phenomena Identification Ranking Table for reflood heat transfer on a component model level and estimate the relative importance of each phenomenon for predicting reflood heat transfer,
2. Develop a test facility design which has a minimum of distortion to represent reflood heat transfer in PWR and BWR cores,
3. Assess the needs of best-estimate computer codes on their modeling approaches for reflood heat transfer and the component models used in the computer codes
4. Perform component experiments which isolate individual phenomena which compromise reflood heat transfer,
5. Determine the effects of the fuel assembly spacer grids on the dispersed flow film boiling heat transfer downstream of the grid,
6. Develop specific component models from these experiments,
7. Add the component models into a best-estimate computer code and compare to the forced reflood heat transfer data from this series of experiments as well as other sets of reflood heat transfer data,
8. Validate the new proposed component reflood heat transfer models over their range of application,
9. Document the results of the experiments and analysis in a form that it can be used by others.

The majority of the experiments will be separate effects tests which will isolate individual models. The separate effects tests which are proposed include:

1. Single phase flow pressure drop experiments to characterize the hydraulic behavior of the facility,
2. Heat loss experiments which characterize the heat losses to the atmosphere which are needed for modeling the facility and analyzing the test data,
3. Radiation heat transfer experiments in a evacuated bundle to assess the rod-to-surface, and rod-to rod radiation heat transfer which is needed to subtract out the radiation contribution from the total measured heat transfer,
4. Single phase steam flow convective heat transfer experiments which cover the Reynolds number range expected in a rod bundle during reflooding,
5. Single phase steam flow experiments with injected droplets over a range of conditions to simulate the dispersed two-phase flow region above the quench front,
6. Forced reflooding experiments over a wide range of conditions typical of a PWR and BWR rod bundle during reflooding,
7. Forced oscillating flow experiments which characterize the inlet flow into a reactor system during reflooding.

The proposed experiments will be performed in a building block approach such that the more complex experiments occur after the more fundamental experiments. In this fashion, additional information and desired test conditions can be modified as needed to optimize the test matrix of the forced reflooding tests which are the most difficult tests to perform. The proposed experiments will provide new unique data as well as supplement existing reflood heat transfer data but they will focus on the improvements of specific best-estimate thermal-hydraulic models rather than identifying licensing margin.

To achieve the objectives of the experiments and to capture the important thermal-hydraulic phenomena which have been identified for reflood heat transfer, several new or novel approaches are proposed for the bundle instrumentation. The characteristics of the froth region are relatively unknown. In this region, the flow changes from a liquid continuous flow to a vapor continuous flow as the rods quench and generate a significant amount of steam. The liquid flow is sheared by the steam and generates a droplet distribution which is entrained into the upper regions of the bundle where the peak cladding temperature occurs. The void fraction in the froth region varies from nearly zero to almost one in the span of approximately one-foot. There are three different measurement systems which will be used in the Rod Bundle Heat Transfer Program:

1. A soft gamma detector with beryllium windows on the test section will measure the chordal average void fraction within the rod bundle as the dispersed flow; froth front and quench pass at selected elevations.

2. Finely spaced, very sensitive differential pressure cells will measure the local pressure along the test section and will be corrected for frictional and acceleration effects to calculate a span average void fraction. It has been demonstrated that many of the apparent functional dependencies (i.e., mass flux, subcooling, and distance from the quench front) for this heat transfer regime are primarily due to the axial profile of the void fraction in this region. Currently available data for this regime in rod bundles is insufficient for model development due to the coarse spacing (from 1 - 2 feet) used for the delta-P cells used to measure the void fraction. The RBHT program will redress this data deficiency through the use of finely spaced delta-P cells (three inch span) and by a local void fraction measurement provided by a low energy gamma-densitometer.
3. A laser illuminated digital camera will be used to measure the drop size, distribution, and velocities at the dispersed flow/froth flow boundary such that the droplet entrainment distribution can be obtained. To correctly calculate the interfacial heat transfer requires the knowledge of both the entrained droplet flow rate and droplet diameter. There is very little data of this type available for quenching rod bundles. The RBHT program will generate the needed database through the use of advanced instrumentation, specifically through the use of the Laser Illuminated Digital Camera System (LIDCS).

At several axial locations in the rod bundle, there will also be steam probes to measure the vapor temperature in the dispersed two-phase mixture or the local fluid temperature for single-phase tests. The laser illuminated digital camera will also be used in this region to obtain the drop distribution, size, and velocity. There will also be ample heater rod temperature measurements along the bundle as well as exit and inlet flow measurements such that the bundle energy and mass balance can be performed and the total heat flux can be separated into radiation heat transfer and flow film boiling heat transfer.

Spacer grids which support the rods in the rod bundle will be instrumented as well as the rod temperatures downstream of the grids and the coolant subchannels downstream of the spacer grids. There will be laser illuminated digital camera system data taken above and below the spacer grids to observe and quantify the change in the droplet diameter and velocity distributions due to the droplet breakup caused by the spacer grids. The heater rod thermocouples and the vapor temperature measurements will also measure the local heat transfer enhancement caused by the spacer grids.

Specific bench-top experiments have been designed to aid in the instrumentation development for the Rod Bundle Heat Transfer program. These bench top experiments test the laser illuminated digital system for droplet measurements in an unheated 3x7 bundle and in a 3x3 heated one-third length bundle. The 3x7 experiments verify the performance of the droplet injector component which will be used in the Rod Bundle Heat Transfer Program. These tests also confirm the ability of the laser illuminated digital camera system to measure the droplet

distribution accurately. The 3x3 heated bundle experiments will specifically examine the effects of spacer grids on the entrained droplet distribution within subchannels. This heated bundle will also provide comparison data on the thermal-hydraulic effects of different spacer grid designs. The 3x3 bench test will also be used to determine the flow disturbance effects of miniature thermocouples which will be used to traverse the rod bundle. A reliable measurement of the non-equilibrium vapor temperature is desired, but since the method used is intrusive, the measurement method must be assessed to ensure that the rod bundle flow is not changed by the measurement technique.

5.3 Conclusions

The objectives of the Rod Bundle Heat Transfer Program have been established to provide the needed data on the highly ranked PIRT phenomenon for reflood heat transfer. Experiments will be performed to isolate a specific phenomenon as best as possible so as to permit specific model development for that phenomenon. The test facility instrumentation has been designed to obtain, as best as possible, the local fluid conditions within the bundle using new and unique techniques. In this manner, the local heat transfer can be related to the local fluid conditions such that the risk of introducing compensating errors into the advanced reflood model package is minimized.

6. FIRST TIER SCALING FOR THE ROD BUNDLE HEAT TRANSFER TEST FACILITY

6.1 Introduction

In order to simulate actual systems (prototype), many experiments are performed at a reduced size, with different materials and different working fluids. The object of the experiment is to capture the phenomena which have been determined to be important for understanding the full size system. Scaling analyses are normally performed for the smaller size models to verify the performance of the full size system.

Scaled experiments have been used for many years in the areas of fluid mechanics for airfoil design, hydraulics for ship design as well as water tables for harbor designs and heated effluent discharges. Scaling fluids have been used in heat transfer studies to simulate high pressure fluids and other dangerous working fluids to examine critical heat flux behavior and core melt conditions. More recently, scaling has been used to simulate the thermal-hydraulic conditions expected in a nuclear reactor for postulated accident conditions. There have been several different thermal-hydraulic scaling approaches proposed by Larson⁽⁶⁻¹⁾ and Ishii⁽⁶⁻²⁾ for single and two-phase systems.

A generalized scaling approach has been developed by Zuber⁽⁶⁻³⁾ for thermal-hydraulic systems in which a two tier scaling approach is given. An important aspect of Zuber's approach is that the scaling process can be used to help identify the most important phenomena as well as the less important phenomena such that when compromises are made, the important phenomena are correctly simulated. This approach has been refined by Wulff⁽⁶⁻⁴⁾ who recommended that the full equation be divided by a "driver term" such that the relative importance of the different terms could be assessed. Zuber⁽⁶⁻⁵⁾ also extended the methodology by using the maximum ranges to normalize variables such that correct limits would be represented. The result has been to translate the scaling analysis into a workable methodology which can be used on any general thermal-hydraulic system.

The Zuber approach was used for the scaling efforts for the Oregon State University AP600 small break Loss of Coolant Accident (LOCA) and long term cooling experiments⁽⁶⁻⁶⁾. The combination of the Zuber and Wulff scaling methodologies were used for the other AP600 experiments to assess possible test distortions relative to the full size reactor⁽⁶⁻⁷⁾. The combined Zuber-Wulff scaling approach is the current state-of-the-art methodology for scaling thermal-hydraulic systems.

This methodology has been used to assess the ability of the Rod Bundle Heat Transfer Test Facility to capture the phenomena of interest for the reflood phase of a LOCA transient such that the data can be used with confidence to verify and develop heat transfer and two-phase flow models for best-estimate thermal-hydraulic computer codes. In addition to verifying that the test facility can produce the desired data, the two tier scaling process also identifies possible distortions in the test facility relative to the nuclear reactor core and will provide a numerical assessment of the importance of the possible distortion.

6.2 Two Tier Scaling Approach

The two tier scaling approach, as developed by Zuber, consists of “top-down” scaling which gives a scaling group for each transfer process as derived from the dimensionless control volume equations for the conservation of mass, momentum, and energy as written for the thermal-hydraulic system. The scaling groups which result from the normalization of the control volume equations are time ratios for the different processes which occur in the system. These groups are called “Pi” parameters. Therefore, top-down scaling or systems approach provides a method for identifying the important phenomena, derive similarity groups, weighting of the different groups to establish priorities, and providing a basis for decoupling fast and slow acting processes which have different time scales. The top-down scaling approach, which is used for both the experiment and the prototype, or full scale system, can identify the lack of similarity between the test and the prototype which indicates scaling distortions. Top-down scaling will also identify those thermal-hydraulic processes which require additional detailed analysis using a “bottom-up” scaling approach.

The bottom-up scaling approach (or process approach) addresses only those thermal-hydraulic processes which are identified as being important or can have distortions which could impact the experiment. Bottom-up scaling will focus on specific Pi terms in the system equations which govern the particular phenomena of interest. The bottom-up scaling can be used to characterize the transport terms in the control volume equations (transport of mass, momentum or energy), establish the relationships for calculating these terms and compare the scaled experiment to the full size prototype.

This section of the report will discuss the application of the first tier or top-down scaling for the Rod Bundle Heat Transfer Test Facility, the bottom-up scaling will be discussed in Section 7.

6.3 Application of the Top-down Scaling Approach

There are three equations which are examined for the Rod Bundle Heat Transfer test facility; the fluid energy equation, the solid energy (heater rod, fuel rod) equation and the fluid momentum equation. Each conservation equation is derived in the fashion as recommended by Zuber and Wulff, the equations are normalized and the terms are divided by the “driver term” such that the resulting Pi groups are dimensionless. This approach is applied to both the Rod Bundle Heat Transfer test facility as well as to a PWR and a BWR fuel assembly to indicate the possible non-typical effects and distortions in the test facility relative to the actual plant component.

Since the tests proposed for the Rod Bundle Heat Transfer test facility are separate effects, the flow at the inlet is forced, or is a prescribed boundary condition. In these situations, the fluid momentum equation has lesser importance as compared to the fluid energy and solid energy equations. However, since one of the primary goals of the analysis is to identify test distortions, the momentum equation will be used to examine the hydraulic behavior of the test facility relative to PWR and BWR fuel assemblies.

6.3.1 Fluid Energy Equation

A simplified fluid energy equation is written for the test bundle with the following assumptions:

- Constant forced flooding rate into the bundle,
- Zero-dimensional analysis. No radial gradients in the fluid. Single and two-phase regions are treated separately,
- No radial temperature gradient in the structures that interact with the fluid; averaged solid temperatures are used,
- The analysis represents a snapshot in time with a single phase region, a two phase region and a quench front on the rods, housing, grids, and dummy (unheated) rods,
- Once a structure is quenched, there is no longer any energy transfer to or from the fluid, flow is assumed to be single phase liquid below the quench front.

The “fluid” in the fluid energy equation is assumed to be single phase liquid below the quench front and superheated vapor, in the two-phase mixture, above the quench front. The real flow above the quench front is a two-phase dispersed flow mixture. However, the vapor represents the continuous phase and is the heat sink for the heat transfer above the quench front. The interfacial heat transfer is also modeled such that the correct vapor temperature would be calculated.

The single phase liquid (below the quench front) and the single phase vapor (beyond the quench front) thermally connects the electrical heater rods (or fuel rods), the test section housing (no housing for a PWR, fuel can for a BWR), the spacer grids used to support the rod bundle and the dummy rods in the test bundle (control rod guide tube thimbles in a PWR and water rods in a BWR). With these assumptions, the fluid energy equation becomes:

$$\begin{aligned}
 & \text{(1)} \qquad \qquad \qquad \text{(2)} \qquad \qquad \qquad \text{(3)} \qquad \text{(4)} \qquad \text{(5)} \qquad \text{(6)} \qquad \text{(7)} \\
 & V_{1\phi} \frac{d}{dt_1} (\rho c_p \Delta T)_{1\phi} + V_{2\phi} \frac{d}{dt_1} (\rho_v e_v) = Q_{q,r} + Q_{q,H} + Q_{q,g} + Q_{q,DR} + Q_{DP} \\
 & - Q_{loss,H} - Q_{loss,g} - Q_{loss,DR} - Q_I + W_{hi} - W_{ho} \\
 & \text{(8)} \qquad \text{(9)} \qquad \text{(10)} \qquad \text{(11)} \qquad \text{(12)} \qquad \text{(13)}
 \end{aligned} \tag{6-1}$$

Where:

- term 1 is the rate of energy change in the single phase region
- term 2 is the rate of energy change of the vapor in the two-phase region
- term 3 is the energy release to the fluid from the rod quenching

term 4 is the energy release to the fluid from the housing quenching
 term 5 is the energy release to the fluid from the grids quenching
 term 6 is the energy release to the fluid from the dummy rods (thimbles) quenching
 term 7 is the energy release to the fluid from the rods above and below the quench front
 term 8 is the energy loss to the housing
 term 9 is the energy loss from the fluid to the spacer grids
 term 10 is the energy loss from the fluid to the dummy rods or control rod thimbles
 term 11 is the interfacial heat transfer between vapor and droplets
 term 12 is the energy flow into the bundle at the inlet
 term 13 is the energy flow out of the bundle at the exit.

A listing of the nomenclature used for the equation development is given at the end of this section.

The quench front represents the dividing line between efficient cooling (nucleate boiling or forced convection) and poor cooling (film boiling, either in a froth region or dispersed flow film boiling). An alternate expression for term 6 for the energy transport into the fluid on either side of the quench front can be used. Below the quench front, the flow will be assumed to be single phase such that the energy into the fluid is equal to the decay power which is specified for the test. Above the quench front, the energy into the fluid is transported by film boiling heat transfer as well as by radiation heat transfer from the heated surfaces to the fluid. Therefore, a more general expression for the energy transfer above the quench front is given as

$$Q_{2\phi} = h_{2\phi,r} A_r (T_r - T_v) + h_{R,r/v} A_r (T_r - T_v) \quad (6-2)$$

Where $h_{2\phi,c}$ is the convective/film boiling heat transfer coefficient, and $h_{R,r/v}$ is the radiation heat transfer coefficient from the heated rod surfaces to the fluid. The reference temperatures for both transfer processes are the rod wall temperatures (T_r) as well as the local fluid vapor (non-equilibrium) temperature (T_v). Therefore, term 7 becomes:

$$Q_{DP} = Q_{DP}|_{1\phi} + \left[h_{2\phi,r} A_r (T_r - T_v) + h_{R,r/v} A_r (T_r - T_v) + h_{R,r/d} A_d (T_r - T_{sat}) \right]_{2\phi} \quad (6-3)$$

The heat transfer in the two-phase region can also be written as energy flows (Btu/hr) instead of a heat transfer coefficient, area and temperature difference as

$$Q_{DP} = Q_{DP,1\phi} + Q_{C/FB} + Q_R \quad (6-4)$$

where $Q_{C/FB}$ represents the convective/film boiling portion of the heat transfer while Q_R represents the radiation portion of the total heat transfer from the rods to the fluid above the quench front.

The quench energy release from the heater rods (or the fuel rods), term 3 ($Q_{q,r}$), can be calculated as

$$Q_{q,r} = \rho_r c_{p,r} V_r \frac{dT_{r,q}}{dt_2} \quad (6-5)$$

where T_r is the property weighted average temperature for the heater rod (or the fuel rod) with $c_{p,r}$, V_r and ρ_r , are the rod weighted specific heat, volume, and density respectively. The temperature-time curve can be estimated from data for heater rod ⁽⁶⁻⁸⁾ and/or nuclear rod quenching, ⁽⁶⁻⁹⁾ as well as from more accurate calculations for a heater and nuclear rods using finite difference methods. Rod quench is assumed to occur when the rod temperature reaches the minimum film boiling temperature. The effects of property differences between the electrical heater rod and the nuclear rod cladding, will be considered when determining the minimum film boiling temperatures used to calculate the rod energy release for electrical heater rods and Zirconium clad fuel rods.

The test section housing heat release is given in term 4 (Equation 6-6) as

$$Q_{q,H} = \rho_H c_{p,H} V_H \frac{dT_{H,q}}{dt_3} \quad (6-6)$$

and represents the heat transferred to the coolant when the housing, which is an elevated temperature, quenches. T_H represents the average housing temperature and ρ_H , $c_{p,H}$ and V_H , represent the housing density, specific heat and volume of the housing which is quenching. The test section housing represents an atypicality or distortion of the test rod bundle relative to a PWR fuel assembly since there is no housing for the PWR assembly. However, when comparing the test facility to a BWR fuel assembly, the similarity is improved, since these assemblies have a channel, similar to a housing. The BWR channel is Zircaloy and not Inconel as used in the experiment; therefore, there can be differences in the minimum film boiling temperature and the resulting quench energy released to the coolant.

Term 5 represents the energy release to the coolant from the quenching of the spacer grids, which are used to position the heater rods or fuel rods, and is given in Equation (6-7) as

$$Q_{q,g} = \rho_g c_{p,g} V_g \frac{dT_{g,q}}{dt_4} \quad (6-7)$$

The spacers are constructed from thin metal shim stock, typically 0.010-inches thick and 1-2 inches in height. It is assumed that the grid will quench at once such that its entire stored energy is released to the coolant. There can be material differences between the test grids, which will be made of Inconel or Stainless steel and the current generation PWR spacers which use Zircaloy. The difference in materials can lead to different minimum film boiling temperatures which in turn affects the energy release. For the experiment, the spacers, cladding surface, housing, and

the dead rods are all made of Inconel, therefore, they all have the same value of T_{\min} . For a PWR or BWR fuel assembly, the cladding and the spacer grids are made of Zircaloy and a T_{\min} value for this material is used.

Term 6 (Equation 6-8) represents the quenching of the unheated support or dummy rods in the bundle. There are four (4) such rods used to represent the presence of guide tube thimbles in the test rod bundle and to allow in bundle instrumentation to be brought out with the minimum flow interference. The dummy rod quench energy is given as

$$Q_{q,DR} = \rho_{DR} c_{p,DR} V_{DR} \frac{dT_{DR,q}}{dt_5} \quad (6-8)$$

Term 7 represents the energy added to the fluid below and above the quench front, as given earlier in Equation 6-3.

Term 8 represents the heat loss from the fluid to the environment through the housing. This term will be most important above the quench front where the fluid, rod and housing temperatures are higher. The heat loss from the fluid to the housing is given as

$$Q_{loss,H} = h_{2\phi,H} A_H (T_v - T_H) + h_{R,v/H} A_H (T_v - T_H) + h_{R,H/d} A_d (T_H - T_{sat}) \quad (6-9)$$

where the first term is the convective/film boiling term while the second term represents the radiation from the superheated vapor to the housing structure and the third term represents the radiation heat transfer from the hot housing to the entrained liquid drops. Both the convective and the radiation terms will operate on the same housing heat transfer area. The expressions for the heat transfer to the housing from the fluid can also be expressed in terms of heat flows (Btu/hr) as

$$Q_{loss,H} = Q_{2\phi,c,H} + Q_{R,H} \quad (6-10)$$

Where $Q_{R,H}$ is the sum of the two radiation components.

In a similar fashion, term 9 models the fluid energy losses to the spacer grids and is given as

$$Q_{loss,g} = h_{2\phi,g} A_g (T_v - T_g) + h_{R,v/g} A_g (T_v - T_g) + h_{R,g/d} A_d (T_g - T_{sat}) \quad (6-11)$$

where the fluid will transfer heat by convection/film boiling and radiation heat transfer. This equation can also be written as heat flows as

$$Q_{loss,g} = Q_{2\phi,c,g} + Q_{R,g} \quad (6-12)$$

Where $Q_{R,g}$ is the sum of the two radiation heat transfer terms.

It should be noted that equation 6-11 is only relevant above the quench front where the vapor is significantly superheated relative to the spacer grids. The differences between the reactor and the test facility will be the geometry and materials used for the spacers. Once the spacers are quenched, there is no longer any significant heat transfer to or from the spacers and the fluid.

In a similar manner, term 10 models the fluid energy loss to the dummy rods or the control rod guide tubes for the reactor case and is given as

$$Q_{loss,DR} = h_{2\phi,DR} A_{DR} (T_v - T_{DR}) + h_{R,v/DR} A_{DR} (T_v - T_{DR}) + h_{R,DR/d} A_d (T_{DR} - T_{sat}) \quad (6-13)$$

The heat transfer from the fluid to these structures is by convection/film boiling and radiation. This only occurs above the quench front where the vapor is superheated and saturated entrained droplets exist. Once the dead rods or thimbles are quenched, there is no longer any energy transfer between these structures and the fluid.

Since the fluid energy equation is written for superheated vapor, and there are entrained droplets present, the two-phase flow above the quench front is not in thermal equilibrium. There is heat transfer between the superheated vapor and the entrained droplets, which are at the saturation temperature. The heat transfer occurs by two paths. The first is convection heat transfer in which the droplet Reynolds and Nusselt numbers depend upon the drop size and the relative velocities of the drops and vapor. The second is radiation heat transfer from vapor to droplets as they are swept along in the test section. Both terms contribute to the total interfacial heat transfer between the continuous vapor phase and the discontinuous entrained droplet phase. The interfacial heat transfer will result in generation of additional saturated steam which mixes with the superheated steam and results in increased steam flow at a lower temperature. The droplet evaporation improves the steam as a heat sink for the heater or fuel rods.

The expression for the interfacial heat transfer becomes:

$$Q_i = h_l A_d (T_r - T_{sat}) + h_{R,v/d} A_d (T_r - T_{sat}) \quad (6-14)$$

Substituting Equations 6-3 to 6-14 into Equation 6-1 gives the fluid energy equation which considers all sources of heat gain and heat loss for the fluid in the test section.

$$\begin{aligned}
& V_{1\phi} \frac{d}{dt_1} (\rho c_p \Delta T)_{1\phi} + V_{2\phi} \frac{d}{dt_1} (\rho_v e_v) = \rho_r c_{p,r} V_r \frac{dT_r}{dt_2} + \rho_H c_{p,H} V_H \frac{dT_H}{dt_3} \\
& \quad + \rho_g c_{p,g} V_g \frac{dT_g}{dt_4} + \rho_{DR} c_{p,DR} V_{DR} \frac{dT_{DR}}{dt_5} + \\
& \left\{ Q_{DP} \Big|_{1\phi} + \left[h_{2\phi,r} A_r (T_r - T_v) + h_{R,v/d} A_r (T_r - T_v) + h_{R,v/d} A_d (T_r - T_{sat}) \right] \right\} \\
& - \left[h_{2\phi,H} A_H (T_v - T_H) + h_{R,v/H} A_H (T_v - T_H) + h_{R,H/d} A_d (T_H - T_{sat}) \right] \\
& - \left[h_{2\phi,g} A_g (T_v - T_g) + h_{R,v/g} A_g (T_v - T_g) + h_{R,g/d} A_d (T_g - T_{sat}) \right] \\
& - \left[h_{2\phi,DR} A_{DR} (T_v - T_{DR}) + h_{R,v/DR} A_{DR} (T_v - T_{DR}) + h_{R,DR/d} A_d (T_{DR} - T_{sat}) \right] \\
& + h_l A_d (T_v - T_{sat}) + h_{R,v/d} A_d (T_v - T_{sat}) + W_i h_i - W_o h_o
\end{aligned} \tag{6-15}$$

The same generalized equation can be used to represent the fluid energy in a PWR or BWR fuel assembly. The differences will be due to the geometry, materials and possible temperature limits. The boundary conditions of flow, pressure and power are the same and can be modeled in the experiments. There are also different components in the fluid energy equation as noted above. There is no housing for a PWR assembly, therefore, these terms represent a distortion of the fluid energy equation relative to a PWR assembly. There is more similarity between a BWR fuel assembly and the test facility since both have a channel surrounding the heater rods.

The next step in the Zuber-Wulff scaling process is to non-dimensionlize the equation to determine the different Pi groups which represent the different transfer processes in either the test facility or in a PWR or BWR fuel assembly. A listing of the parameters used to normalize each term in Equation 6-15 is given in Table 6-1. The initial conditions and boundary conditions are used for the normalization. Ranges are selected such that they address the variability of the different parameters. The initial conditions and their definitions are given in Table 6-2.

Table 6-1

Normalizing Factors for Fluid Energy Equation

$$A_{DR}^* = \frac{A_{DR}}{A_{DR,i}}$$

$$A_g^* = \frac{A_g}{A_{g,i}}$$

$$A_H^* = \frac{A_H}{A_{H,i}}$$

$$A_r^* = \frac{A_r}{A_{r,i}}$$

$$c_p^* = \frac{c_p}{c_{p,i}}$$

$$W^* = \frac{W}{W_i}$$

$$W_e^* = \frac{W_e}{W_e}$$

$$W_i^* = \frac{W_i}{W_i}$$

$$\phi_{DP}^* = \frac{\phi_{DP}}{\phi_{DP,i}}$$

$$\rho^* = \frac{\rho}{\rho_i}$$

$$T_r^* - T_v^* = \frac{T_r - T_v}{T_{\max,r} - T_{sat}}$$

$$T_{DR,q}^* = \frac{T_{DR,q}}{T_{\min,DR} - T_{sat}}$$

$$T_{g,q}^* = \frac{T_{g,q}}{T_{\min,g} - T_{sat}}$$

$$T_{H,q}^* = \frac{T_{H,q}}{T_{\min,H} - T_{sat}}$$

$$T_{r,q}^* = \frac{T_{r,q}}{T_{\min,r} - T_{sat}}$$

$$h_l^* = \frac{h_l}{h_{l,i}}$$

$$h_{2\phi,DR}^* = \frac{h_{2\phi,DR}}{h_s}$$

$$h_{2\phi,g}^* = \frac{h_{2\phi,g}}{h_s}$$

$$h_{2\phi,H}^* = \frac{h_{2\phi,H}}{h_s}$$

$$h_{2\phi,r}^* = \frac{h_{2\phi,r}}{h_s}$$

$$h_{R,r/v}^* = \frac{h_{R,r/v}}{h_{R,r/v,i}}$$

$$h_{R,r/d}^* = \frac{h_{R,r/d}}{h_{R,r/d,i}}$$

$$h_{R,y/H}^* = \frac{h_{R,y/H}}{h_{R,y/H,i}}$$

$$h_{R,H/d}^* = \frac{h_{R,H/d}}{h_{R,H/d,i}}$$

$$h_{R,y/g}^* = \frac{h_{R,y/g}}{h_{R,y/g,i}}$$

$$h_{R,s/d}^* = \frac{h_{R,s/d}}{h_{R,s/d,i}}$$

$$h_{R,y/DR}^* = \frac{h_{R,y/DR}}{h_{R,y/DR,i}}$$

$$h_{R,DR/d}^* = \frac{h_{R,DR/d}}{h_{R,DR/d,i}}$$

$$h_{R,y/d}^* = \frac{h_{R,y/d}}{h_{R,y/d,i}}$$

Table 6-2

List of Initial Conditions and Assumptions

1. Normalization for fluid and rod properties was done on the inlet conditions for the fluid, and the initial conditions for the rod.
2. The flows were initialized on the inlet flow, W_i
3. Time constants for structures were defined in the text of the report.
4. The temperature for a component is normalized by the expected maximum temperature variation for the component, such as

$$T_r^* = \frac{T_r}{T_{r,CL} - T_{sat}}$$

where $T_{r,CL}$ is the centerline temperature and T_{sat} is the saturation temperature.

5. The lengths were normalized on the full length of the bundle.
6. Pressure drop was normalized on the velocity head of the fluid.
7. The fluid momentum equation was normalized on the static head for the bundle.

The total volume is the sum of the single phase and two phase volumes. Thus,

$$V_{1\phi} + V_{2\phi} = V_T \quad (6-16)$$

The time scale for the temporal terms is assumed to be the same for single phase and two-phase flow. That is, the time constant is defined in terms of the inlet flow rate and the total fluid volume as

$$\tau_1 = \frac{\rho_i V_T}{W_i} \quad (6-17)$$

τ_1 is used to normalize the time rate of change terms on the lefthand side of Equation 6-15.

Separate time constants are used to model the quenching of the heater rods, spacer grids and the housing. During the quenching, the convection heat transfer coefficient is about 5.6782 kW/m²K (1000 Btu/hr-ft²-F). The Biot number is of the order of unity for all the heat structures with the exception of the spacer grids which has a Biot number much lower than 1.0. Therefore, in general, the conductivity across the heat structures cannot be neglected. For each structure the heat removal is characterized by a time constant:

heater rods	τ_2
housing	τ_3
grids	τ_4
dummy rods	τ_5

The quench energy terms are normalized as follows:

$$Q_{q,r} = \rho_r c_{p,r} V_r \frac{dT_{r,q}}{dt_2} = \frac{\rho_{r,i} c_{p,r,i} V_{r,i} (T_{\min,r} - T_{sat})}{\tau_2} \rho_r^* c_{p,r}^* V_r^* \frac{dT_{r,q}^*}{dt_2^*} \quad (6-18)$$

$$Q_{q,H} = \rho_H c_{p,H} V_H \frac{dT_{H,q}}{dt_3} = \frac{\rho_{H,i} c_{p,H,i} V_{H,i} (T_{\min,H} - T_{sat})}{\tau_3} \rho_H^* c_{p,H}^* V_H^* \frac{dT_{H,q}^*}{dt_3^*} \quad (6-19)$$

$$Q_{q,g} = \rho_g c_{p,g} V_g \frac{dT_{g,q}}{dt_4} = \frac{\rho_{g,i} c_{p,g,i} V_{g,i} (T_{\min,g} - T_{sat})}{\tau_4} \rho_g^* c_{p,g}^* V_g^* \frac{dT_{g,q}^*}{dt_4^*} \quad (6-20)$$

$$Q_{q,DR} = \rho_{DR} c_{p,DR} V_{DR} \frac{dT_{DR,q}}{dt_5} = \frac{\rho_{DR,i} c_{p,DR,i} V_{DR,i} (T_{\min} - T_{sat})}{\tau_5} \rho_{DR}^* c_{p,DR}^* V_{DR}^* \frac{dT_{DR,q}^*}{dt_5^*} \quad (6-21)$$

The temporal term representing the rate of change of energy storage within the control volume, term 2, becomes

$$V_{2\phi} \frac{d}{dt_1} (\rho_v e_v) = V_{2\phi} \frac{d}{dt_1} (\rho_v c_p \Delta T_v) \quad (6-22)$$

where

$$e_v = c_p \Delta T_v \quad (6-23)$$

and

$$\Delta T_v = T_v - T_{sat} \quad (6-24)$$

Operating on each term in Equation 6-15 using the normalizing parameters from Table 6-1 and ranges from Table 6-2 gives:

$$\begin{aligned} & W_i c_{p,i} (T_f - T_i) V_{1\phi}^* \frac{d}{dt_1^*} (\rho^* c_p^* \Delta T^*)_{1\phi} + \frac{W_i \rho_{v,sat,i} c_{p,sat,i} (T_{max,v} - T_{sat})}{\rho_i} V_2^* \frac{d}{dt_1^*} (\rho_v^* c_{p,v}^* \Delta T_v^*) = \\ & \frac{\rho_{r,i} c_{p,r,i} V_{r,i} (T_{min,r} - T_{sat})}{\tau_2} \rho_r^* c_{p,r}^* V_r^* \frac{dT_{r,q}^*}{dt_2^*} + \frac{\rho_{H,i} c_{p,H,i} V_{H,i} (T_{min,H} - T_{sat})}{\tau_3} \rho_H^* c_{p,H}^* V_H^* \frac{dT_{H,q}^*}{dt_3^*} \\ & + \frac{\rho_{g,i} c_{p,g,i} V_{g,i} (T_{min,g} - T_{sat})}{\tau_4} \rho_g^* c_{p,g}^* V_g^* \frac{dT_{g,q}^*}{dt_4^*} + \\ & \frac{\rho_{DR,i} c_{p,DR,i} V_{DR,i} (T_{min} - T_{sat})}{\tau_5} \rho_{DR}^* c_{p,DR}^* V_{DR}^* \frac{dT_{DR,q}^*}{dt_5^*} \\ & + \left\{ Q_{DP,i} Q_{DP}^* + [h_s A_{r,i} (T_{max,r} - T_{sat}) h_{2\phi,r}^* A_r^* (T_r^* - T_v^*) + \right. \\ & \left. h_{R,r/v,i} A_{r,i} (T_{max,r} - T_{sat}) h_{R,r/v}^* A_r^* (T_r^* - T_v^*) + h_{R,r/d,i} A_{d,i} (T_{max,r} - T_{sat}) h_{R,r/d}^* A_d^* (T_r^* - T_{sat}^*) \right\} - \end{aligned} \quad (6-25)$$

$$\begin{aligned}
& \left\{ \left[h_s A_{H,i} (T_{\max,H} - T_{sat}) h_{2\phi,H}^* A_H^* (T_v^* - T_H^*) \right] + \left[h_{R,v/H,i} A_{H,i} (T_{\max,H} - T_{sat}) h_{R,v/H}^* A_H^* (T_v^* - T_H^*) \right] \right\} + \\
& \left[h_{R,H/d,i} A_{d,i} (T_{\max,H} - T_{sat,H}) h_{R,H/d}^* A_d^* (T_H^* - T_{sat}^*) \right] - \left\{ \left[h_s A_{g,i} (T_{\max,g} - T_{sat}) h_{2\phi,g}^* A_g^* (T_v^* - T_g^*) \right] \right. \\
& \left. + \left[h_{R,v/g} A_{g,i} (T_{\max,g} - T_{sat}) h_{R,v/g}^* A_g^* (T_v^* - T_g^*) \right] + \left[h_{R,g/d,i} A_{d,i} (T_{\max,g} - T_{sat}) h_{R,g/d}^* A_d^* (T_g^* - T_{sat}^*) \right] \right\} \\
& - \left\{ \left[h_s A_{DR,i} (T_{\max,DR} - T_{sat}) h_{2\phi,DR}^* A_{DR}^* (T_v^* - T_{DR}^*) \right] + \left[h_{R,v/DR,i} A_{DR,i} (T_{\max,DR} - T_{sat}) h_{R,v/DR}^* A_{DR}^* (T_v^* - T_{DR}^*) \right] \right\} + \\
& \left[h_{R,DR/d,i} A_{d,i} (T_{\max,DR} - T_{sat}) h_{R,DR/d}^* A_d^* (T_{DR}^* - T_{sat}^*) \right] + \left[h_{l,i} A_{d,i} (T_{\max,v} - T_{sat}) h_l^* A_d^* (T_v^* - T_{sat}^*) \right] \\
& + \left[h_{R,v/d,i} A_{d,i} (T_{\max,v} - T_{sat}) h_{R,v/d}^* A_d^* (T_v^* - T_{sat}^*) \right] + W_i (h_f - h_i) W_i^* h_i^* - W_o (h_s - h_g) W_o^* h_o^*
\end{aligned}$$

If we now divide all terms in Equation 6-25 by the “driver term” as first proposed by Wulff, one can obtain the normalized Pi time constants which represent the heat transfer processes in the rod bundle during reflood. The driver term selected is the initial decay power, Q_{DP_i} , which is a test boundary condition. Therefore, each heat transfer process will be evaluated relative the initial bundle decay power. The resulting normalized Pi groups become:

$$\Pi_1 = \frac{W_i c_{p,i} (T_{sat} - T_i)}{Q_{DP_i}} = \frac{1\phi \text{ fluid sensible energy / time}}{\text{Initial decay power}} \quad (6-26)$$

$$\Pi_2 = \frac{W_i \rho_{v,sat,i} c_{p,v,sat,i} (T_{\max} - T_{sat})}{\rho_i Q_{DP_i}} = \frac{\text{Vapor sensible energy / time}}{\text{Initial decay power}} \quad (6-27)$$

$$\Pi_3 = \frac{\rho_{r,i} c_{p,r,i} V_{r,q,i} (T_{\max,r,q} - T_{sat})}{\tau_2 Q_{DP_i}} = \frac{\text{Rod quench energy / time}}{\text{Initial decay power}} \quad (6-28)$$

$$\Pi_4 = \frac{\rho_{H,i} c_{p,H,i} V_{H,q,i} (T_{\min,H,q} - T_{sat})}{\tau_3 Q_{DP_i}} = \frac{\text{Housing quench energy / time}}{\text{Initial decay power}} \quad (6-29)$$

$$\Pi_5 = \frac{\rho_{g,i} c_{p,g,i} V_{g,q,i} (T_{\min,g,q} - T_{sat})}{\tau_4 Q_{DP_i}} = \frac{\text{Grid quench energy / time}}{\text{Initial decay power}} \quad (6-30)$$

$$\Pi_6 = \frac{\rho_{DR,i} c_{p,DR,i} V_{DR,q,i} (T_{\min,DR,q} - T_{sat})}{\tau_5 Q_{DP_i}} = \frac{\text{Dead rod quench energy / time}}{\text{Initial decay power}} \quad (6-31)$$

$$\Pi_7 = \frac{Q_{DP}|_{1\phi}}{Q_{DP_i}} \quad (6-32)$$

$$\Pi_8 = \frac{h_s A_{r,i} (T_{\max,r} - T_{sat})}{Q_{DP_i}} = \frac{\text{Convective heat rate from rods to mixture vapor}}{\text{Initial decay power}} \quad (6-33)$$

$$\Pi_9 = \frac{h_{R,r/v,i} A_{r,i} (T_{\max,r} - T_v)}{Q_{DP_i}} = \frac{\text{Radiation heat rate from rods to vapor}}{\text{Initial decay power}} \quad (6-34)$$

$$\Pi_{10} = \frac{h_{R,r/d,i} A_{d,i} (T_{\max,r} - T_{sat})}{Q_{DP_i}} = \frac{\text{Radiation heat rate from rod to drops}}{\text{Initial decay power}} \quad (6-35)$$

$$\Pi_{11} = \frac{h_s A_{H,i} (T_{\max,H} - T_{sat})}{Q_{DP_i}} = \frac{\text{Convective heat rate from mixture to housing}}{\text{Initial decay power}} \quad (6-36)$$

$$\Pi_{12} = \frac{h_{R,v/H,i} A_{H,i} (T_{\max,H} - T_v)}{Q_{DP_i}} = \frac{\text{Radiative heat rate from vapor to housing}}{\text{Initial decay power}} \quad (6-37)$$

$$\Pi_{13} = \frac{h_{R,H/d,i} A_{d,i} (T_{\max,H} - T_{sat})}{Q_{DP_i}} = \frac{\text{Radiation heat rate from housing to drops}}{\text{Initial decay power}} \quad (6-38)$$

$$\Pi_{14} = \frac{h_s A_{g,i} (T_{\max,g} - T_{sat})}{Q_{DP_i}} = \frac{\text{Convective heat rate from vapor to grids}}{\text{Initial decay power}} \quad (6-39)$$

$$\Pi_{15} = \frac{h_{R,v/g,i} A_{g,i} (T_{\max,g} - T_v)}{Q_{DP_i}} = \frac{\text{Radiation heat rate from vapor to grids}}{\text{Initial decay power}} \quad (6-40)$$

$$\Pi_{16} = \frac{h_{R,g/d,i} A_{d,i} (T_{\max,g} - T_{sat})}{Q_{DP_i}} = \frac{\text{Radiation heat rate from grids to drops}}{\text{Initial decay power}} \quad (6-41)$$

$$\Pi_{17} = \frac{h_s A_{DR,i} (T_{\max,DR} - T_{sat})}{Q_{DP_i}} = \frac{\text{Convective heat rate from vapor to dead rod}}{\text{Initial decay power}} \quad (6-42)$$

$$\Pi_{18} = \frac{h_{R,v/DR,i} A_{DR,i} (T_{\max,DR} - T_v)}{Q_{DP_i}} = \frac{\text{Radiation heat rate from vapor to dead rods}}{\text{Initial decay power}} \quad (6-43)$$

$$\Pi_{19} = \frac{h_{R,DR/d,i} A_{d,i} (T_{\max,DR} - T_{sat})}{Q_{DP_i}} = \frac{\text{Radiation heat rate from dead rods to drops}}{\text{Initial decay power}} \quad (6-44)$$

$$\Pi_{20} = \frac{h_{l,i} A_d (T_{\max,v} - T_{sat})}{Q_{DP_i}} = \frac{\text{Interfacial heat transfer rate}}{\text{Initial decay power}} \quad (6-45)$$

$$\Pi_{21} = \frac{h_{R,v/d,i} A_{d,i} (T_{\max,v} - T_{sat})}{Q_{DP_i}} = \frac{\text{Radiation heat rate from vapor to drops}}{\text{Initial decay power}} \quad (6-46)$$

$$\Pi_{22} = \frac{W_i (h_f - h_i)}{Q_{DP_i}} = \frac{W_i c_{p,i} (T_f - T_i)}{Q_{DP_i}} = \Pi_1 \quad (6-47)$$

$$\Pi_{23} = \frac{W_o (h_s - h_g)}{Q_{DP_i}} = \frac{\text{Exit mixture energy / time}}{\text{Initial decay power}} \quad (6-48)$$

Therefore Equation 6-25 becomes

$$\begin{aligned} & \Pi_1 V_{1\phi}^* \frac{d}{dt_1} (\rho^* c_p^* \Delta T^*)_{1\phi} + \Pi_2 V_{2\phi}^* \frac{d}{dt_1} (\rho_v^* c_{p,v}^* \Delta T_v^*) = \Pi_3 \frac{dT_{r,q}^*}{dt_2^*} \\ & + \Pi_4 \frac{dT_{H,q}^*}{dt_3^*} + \Pi_5 \frac{dT_{g,q}^*}{dt_4^*} + \Pi_6 \frac{dT_{DR,q}^*}{dt_5^*} + 1 + \Pi_8 h_{2\phi,r}^* A_r^* (T_r^* - T_v^*) \\ & + \Pi_9 h_{R,r/v}^* A_r^* (T_r^* - T_v^*) + \Pi_{10} h_{R,r/d}^* A_d^* (T_r^* - T_{sat}^*) - \Pi_{11} h_{2\phi,H}^* A_H^* (T_v^* - T_H^*) \\ & - \Pi_{12} h_{R,v/H}^* A_H^* (T_v^* - T_H^*) - \Pi_{13} h_{R,H/d}^* A_d^* (T_H^* - T_{sat}^*) - \Pi_{14} h_{2\phi,g}^* A_g^* (T_v^* - T_g^*) \end{aligned} \quad (6-49)$$

$$\begin{aligned}
& -\Pi_{15} h_{R,v/g}^* A_g^* (T_v^* - T_g^*) - \Pi_{16} h_{R,g/d}^* A_d^* (T_g^* - T_{sat}^*) - \Pi_{17} h_{2\phi,DR}^* A_{DR}^* (T_v^* - T_{DR}^*) \\
& -\Pi_{18} h_{R,v/DR}^* A_{DR}^* (T_v^* - T_{DR}^*) - \Pi_{19} h_{R,DR/d}^* A_d^* (T_{DR}^* - T_{sat}^*) + \Pi_{20} h_i^* A_d^* (T_v^* - T_{sat}^*) \\
& + \Pi_{21} h_{R,v/d}^* A_d^* (T_v^* - T_{sat}^*) + \Pi_1 W_i^* h_i^* - \Pi_{23} W_o^* h_o^*
\end{aligned}$$

These Pi groups can be numerically calculated using the assumptions given in Table 6-2 for the heat transfer coefficients, heat flows and material properties. The results of the different Pi group calculations will be given in Section 6.4 of this report.

Tables 6-3 and 6-4 summarize and compare the expected values of the fluid energy equation Pi groups of the RBHT test facility with those of a PWR and BWR respectively. Since the rod bundle geometry models a PWR assembly, it is expected that most of the Pi groups are preserved. However, since there is no housing in a PWR assembly, to ensure similarity, the Pi groups which represent the heat transfer processes associated with the housing should be small. Since the test facility has a housing similar to a BWR channel, the same Pi groups derived for the RBHT test facility are present for a BWR fuel assembly. Their magnitudes are expected to be slightly different because of differences in material properties.

**Table 6-3
PWR Comparisons**

$\Pi_{1_t} \cong \Pi_{1_{PWR}}$	Should be similar since geometry is approximately correct and flows, powers are typical
$\Pi_{2_t} \cong \Pi_{2_{PWR}}$	Similar to Π_1 above, geometry is exact but power and flows are typical
$\Pi_{3_t} \cong \Pi_{3_{PWR}}$	not clear due to rod size and properties - need to check
$\Pi_{4_t} \neq \Pi_{4_{PWR}}$	Distortion, as there is no housing in PWR.
$\Pi_{5_t} \approx \Pi_{5_{PWR}}$	not clear how similar due to different materials and thicknesses (grids)
$\Pi_{6_t} \approx \Pi_{6_{PWR}}$	not clear how similar due to different materials and thicknesses (dead or water rods)
$\Pi_{7_t} = \Pi_{7_{PWR}}$	controllable boundary conditions
$\Pi_{8_t} \stackrel{?}{=} \Pi_{8_{PWR}}$	should be similar but geometry differences exist
$\Pi_{9_t} \stackrel{?}{=} \Pi_{9_{PWR}}$	should be similar but geometry differences exist
$\Pi_{10_t} \stackrel{?}{=} \Pi_{10_{PWR}}$	should be similar but geometry differences exist
$\Pi_{11_t} \neq \Pi_{11_{PWR}}$	Distortion, as there is no housing in PWR.
$\Pi_{12_t} \neq \Pi_{12_{PWR}}$	Distortion, as there is no housing in PWR.
$\Pi_{13_t} \neq \Pi_{13_{PWR}}$	Distortion, as there is no housing in PWR.
$\Pi_{14_t} \stackrel{?}{\approx} \Pi_{14_{PWR}}$	some differences due to grid designs, materials
$\Pi_{15_t} \stackrel{?}{\approx} \Pi_{15_{PWR}}$	some differences due to grid designs, materials
$\Pi_{16_t} \stackrel{?}{\approx} \Pi_{16_{PWR}}$	some differences due to grid designs, materials

**Table 6-3
PWR Comparisons**

$\Pi_{17_i} \stackrel{?}{\approx} \Pi_{17_{PWR}}$	different materials, geometries, number - need to check
$\Pi_{18_i} \stackrel{?}{\cong} \Pi_{18_{PWR}}$	different materials, geometries, number - need to check
$\Pi_{19_i} \stackrel{?}{\cong} \Pi_{19_{PWR}}$	different materials, geometries, number - need to check
$\Pi_{20_i} \approx \Pi_{20_{PWR}}$	Should be similar, as it is related to drops only and not materials, dimensions etc.
$\Pi_{21_i} \approx \Pi_{21_{PWR}}$	Should be similar, as it is related to drops only and not materials, dimensions etc.
$\Pi_{23_i} \approx \Pi_{23_{PWR}}$	should be similar, but not exact due to geometry differences.
<p>Note: some of the parameters, Pi groups, can be made closer by adjusting the fluid conditions. Other Pi groups reflect the materials and geometry differences between the PWR and BWR assemblies so the simulation will only be approximate for a BWR.</p>	

**Table 6-4
BWR Comparisons**

$\Pi_{1_t} \cong \Pi_{1_{BWR}}$	Should be similar since geometry is approximately correct (not sized for BWR) and flows, powers are typical
$\Pi_{2_t} \cong \Pi_{2_{BWR}}$	Similar to Π_1 above, geometry is exact but power and flows are typical
$\Pi_{3_t} \cong \Pi_{3_{BWR}}$	not clear due to rod size and properties - need to check
$\Pi_{4_t} \cong \Pi_{4_{BWR}}$	not clear how similar due to different materials and thicknesses (housing)
$\Pi_{5_t} \approx \Pi_{5_{BWR}}$	not clear how similar due to different materials and thicknesses (grids)
$\Pi_{6_t} \approx \Pi_{6_{BWR}}$	not clear how similar due to different materials and thicknesses (dead or water rods)
$\Pi_{7_t} = \Pi_{7_{BWR}}$	controllable boundary conditions
$\Pi_{8_t} \stackrel{?}{=} \Pi_{8_{BWR}}$	should be similar but geometry differences exist
$\Pi_{9_t} \stackrel{?}{=} \Pi_{9_{BWR}}$	should be similar but geometry differences exist
$\Pi_{10_t} \stackrel{?}{\approx} \Pi_{10_{BWR}}$	should be similar but geometry differences exist
$\Pi_{11_t} \stackrel{?}{\approx} \Pi_{11_{BWR}}$	should be similar but housing thickness, material are different
$\Pi_{12_t} \stackrel{?}{\approx} \Pi_{12_{BWR}}$	should be similar but housing thickness, material are different
$\Pi_{13_t} \approx \Pi_{13_{BWR}}$	should be similar but housing thickness, material are different
$\Pi_{14_t} \stackrel{?}{\approx} \Pi_{14_{BWR}}$	some differences due to grid designs, materials
$\Pi_{15_t} \approx \Pi_{15_{BWR}}$	some differences due to grid designs, materials
$\Pi_{16_t} \stackrel{?}{\cong} \Pi_{16_{BWR}}$	some differences due to grid designs, materials
$\Pi_{17_t} \stackrel{?}{\approx} \Pi_{17_{BWR}}$	different materials, geometries, number - need to check

**Table 6-4
BWR Comparisons**

$\Pi_{18,} \stackrel{?}{\cong} \Pi_{18_{BWR}}$	different materials, geometries, number - need to check
$\Pi_{19,} \stackrel{?}{\cong} \Pi_{19_{BWR}}$	different materials, geometries, number - need to check
$\Pi_{20,} \approx \Pi_{20_{BWR}}$	Should be similar, as it is related to drops only and not materials, dimensions etc
$\Pi_{21,} \approx \Pi_{21_{BWR}}$	Should be similar, as it is related to drops only and not materials, dimensions etc
$\Pi_{23,} \approx \Pi_{23_{BWR}}$	should be similar, but not exact due to geometry differences.
<p>Note: some of the parameters, Pi groups, can be made closer by adjusting the fluid conditions. Other Pi groups reflect the materials and geometry differences between the PWR and BWR assemblies so the simulation will only be approximate for a BWR.</p>	

6.3.2 Heater Rod (Fuel Rod) Energy Equation Scaling

Equation 6-1 accounts for the energy release from the rods to the fluid and for some of the test distortions relative to a nuclear fuel assembly. The following analysis examines the behavior of the heater rod and a nuclear rod to determine the similarities and differences in their response to a reflood transient at or near the time that the peak cladding temperature would be calculated. In this situation, the quench front would be approximately 2 or 3 feet below the peak temperature location such that there would be no axial conduction effects and one-dimensional radial heat transfer is sufficient. The analysis will also consider the effects of the housing on the rod thermal response.

Two heat transfer equations are developed for the rods; an equation which describes the transient fuel, or boron nitride (BN) and heating coil power generating region; and an equation for the cladding which reflects the rod interactions with the flow field, housing and other surfaces. The assumptions for the equation development include:

- Analysis at one axial position in the bundle,
- No axial conduction, that is, far from the quench front
- Selected location on the rod is in dispersed flow film boiling, and the temperatures of the rod exceed T_{min} ,
- A gap heat transfer coefficient couples the fuel pellet or boron nitride and heating coil, to the cladding,
- Heat generation is either in the fuel pellet region or in the boron nitride and heater coil region (BN).

The radial conduction equation can be written for the fuel or BN region as:

$$\rho_f c_{p,f} V_f \frac{\partial T_f}{\partial t} - \frac{1}{r} \frac{\partial}{\partial r} \left(k_f r \frac{\partial T_f}{\partial r} \right) V_f = Q_f''' V_f - h_{gap} A_i (T_s - T_{ci}) \quad (6-50)$$

where Q_f''' is the volumetric heat generation for the fuel or BN region.

A similar radial conduction equation can be written for the cladding as

$$\rho_c c_{p,c} V_c \frac{\partial T_c}{\partial t} + \frac{1}{r} \frac{\partial}{\partial r} \left(k_c r \frac{\partial T_c}{\partial r} \right) V_c = h_{gap} A_i (T_s - T_{ci}) - h_c A_c (T_{co} - T_v)$$

(from pellet) (convective)

$$\begin{aligned}
& -h_{R,s} A_{R,s} (T_{co} - T_s) - h_{R,H} A_{R,H} (T_{co} - T_H) - h_{R,hr/cr} A_{R,hr/cr} (T_{co,hr} - T_{co,cr}) \\
& \text{(surface radiation) (housing radiation) (hot rod to cold rod radiation)}
\end{aligned} \tag{6-51}$$

$$\begin{aligned}
& -h_{lw} A_{lw} (T_{co} - T_{sat}) - h_{R,d} A_{R,d} (T_{co} - T_{sat}) - h_{R,v} A_{R,v} (T_{co} - T_v) \\
& \text{(liquid contact HT) (radiation to drops) (radiation to vapor)}
\end{aligned}$$

where the heat losses to the fluid, direct contact heat transfer, and the radiation heat transfer to the different components in the flow and bundle are indicated. This formulation allows rod-to-housing and rod to cold rod radiation heat transfer to occur. The heat transfer from the pellet or BN and heating coil to the cladding is given as

$$q = h_{gap} A_i (T_s - T_{ci}) \tag{6-52}$$

Since the region of interest for the rod is assumed to be in dispersed flow film boiling, the local void fraction is greater than 90% such that there is allowable radiation heat transfer between the different components in the bundle. In this situation, the region of interest is also far from the quench front.

The parameters for the normalization of Equations 6-50 and 6-51 are given on Table 6-5 and are similar to those used for the normalization of Equation 6-1. The individual temperature difference for that component temperature drop, as shown in Table 6-5. In this fashion, the relative temperature differences are preserved. The time constant τ_f is the fuel pellet and or BN region time constant.

Using the definitions from Table 6-5 and substituting into Equation 6-50 gives

$$\begin{aligned}
& \frac{\rho_{f,i} c_{p,f,i} V_{fi} (T_{f,CL} - T_s)}{\tau_f} \rho_f^* c_{p,f}^* V_f^* \frac{\partial T_f^*}{\partial t^*} + \\
& \frac{R_o k_{f,i} (T_{f,CL} - T_s)}{R_f^2 R_o} V_{ci} \frac{1}{r^*} \frac{\partial}{\partial r^*} \left(k_f^* r^* \frac{\partial T_f^*}{\partial r^*} \right) V_f^* = Q_{fi}'' V_{fi} Q_f'' V_f^*
\end{aligned} \tag{6-53}$$

$$-h_{gap,i} A_{i,i} (T_s - T_{ci}) h_{gap}^* A_i^* (T_s - T_{ci})^*$$

Table 6-5

Normalization Parameters for Rod Energy Equation

$$A_i^* = \frac{A_i}{A_{i,i}}, \quad C_{p,c}^* = \frac{C_{p,c}}{C_{p,c,i}}, \quad C_{p,f}^* = \frac{C_{p,f}}{C_{p,f,i}}$$

$$h_c^* = \frac{h_c}{h_{c,i}}, \quad h_{gap}^* = \frac{h_{gap}}{h_{gap,i}}, \quad h_{R,hr/cr}^* = \frac{h_{R,hr/cr}}{h_{R,hr/cr,i}}$$

$$k_f^* = \frac{k_f}{k_{f,i}}, \quad Q_f^{***} = \frac{Q_f^{***}}{Q_{f,i}^{***}}, \quad r^* = \frac{r}{R_f}$$

$$t^* = \frac{t}{\tau_c}, \text{ (For clad)} \quad t^* = \frac{t}{\tau_f} \text{ (For fuel)}$$

$$T_c^* = \frac{T_c}{(T_{ci} - T_{co})}, \quad T_f^* = \frac{T_f}{(T_{f,CL} - T_s)}$$

$$V_c^* = \frac{V_c}{V_{c,i}}, \quad V_f^* = \frac{V_f}{V_{f,i}}$$

$$\rho_c^* = \frac{\rho_c}{\rho_{c,i}}, \quad \rho_f^* = \frac{\rho_f}{\rho_{f,i}}$$

Equation 6-50 can be normalized by dividing each term in the equation by the “driver” term as recommended by Wulff. For this situation, the driver term is the initial power which is given as $V_{fi} Q_i'''$. Performing the division results in the different Pi groups for the pellet or BN region of the fuel or heater rod. The Pi groups are:

$$\Pi_{24} = \frac{\rho_{f,i} c_{p,f,i} (T_{f,CL} - T_s)}{\tau_f Q_i'''} = \frac{\text{Stored energy / time}}{\text{Initial heat generation rate}} \quad (6-54)$$

$$\Pi_{25} = \frac{k_{f,i} (T_{f,CL} - T_s)}{R_f^2 Q_i'''} = \frac{\text{Clad heat conduction rate}}{\text{Initial heat generation rate}} \quad (6-55)$$

$$\Pi_{26} = \frac{V_{fi} Q_i'''}{V_{fi} Q_i'''} = 1 \quad (6-56)$$

Π_{26} is identically unity since this was the driver term which was used to normalize the other Pi values. The normalization of the h_{gap} term yields a Pi group which is identical to Π_{29} .

$$\Pi_{29} = \frac{h_{gap,i} A_{i,i} (T_s - T_{ci})}{Q_i''' V_{fi}} = \frac{\text{Heat transfer rate from pellet to clad}}{\text{Heat generation rate}} \quad (6-57)$$

The parameters used to normalize the clad conduction equation are also given in Table 6-5 where τ_c is the cladding time constant. Normalizing Equation 6-51 gives

$$\begin{aligned}
& \frac{\rho_{c,i} c_{p,c,i} V_{ci} (T_{ci} - T_{co})}{\tau_c} \rho_c^* c_{p,c}^* \frac{\partial T_c^*}{\partial t^*} + \\
& \frac{1}{R_i^2} k_{c,i} (T_{ci} - T_{co}) V_{ci} \frac{1}{r^*} \frac{\partial}{\partial r^*} \left(k_f^* r^* \frac{\partial T_c^*}{\partial r^*} \right) V_c^* = \\
& h_{gap,i} A_{i,i} (T_s - T_{ci}) h_{gap}^* A_i^* (T_s - T_{ci})^* - h_{c,i} A_{c,i} (T_{co} - T_{sat}) h_c^* A_c^* (T_{co} - T_v)^* \\
& - h_{R,r/s,i} A_{R,s,i} (T_{co} - T_s) h_{R,r/s}^* A_{R,s}^* (T_{co} - T_s)^* - h_{R,r/H,i} A_{R,H,i} (T_{co} - T_H) h_{R,r/H}^* A_{R,H}^* (T_{co} - T_H)^* \quad (6-58) \\
& - h_{R,hr/cr,i} A_{R,hr/cr,i} (T_{co,hr} - T_{co,cr}) h_{R,hr/cr}^* A_{R,hr/cr}^* (T_{co,hr} - T_{co,cr})^* \\
& - h_{\ell w,i} A_{\ell w,i} (T_{co} - T_{sat}) h_{\ell w}^* A_{\ell w}^* (T_{co} - T_{sat})^* \\
& - h_{R,r/d,i} A_{R,r/d,i} (T_{f,CL} - T_{sat}) h_{R,r/d}^* A_{R,r/d}^* (T_{co} - T_{sat})^* \\
& - h_{R,r/v,i} A_{R,r/v,i} (T_{f,CL} - T_{sat}) h_{R,r/v}^* A_{R,r/v}^* (T_{co} - T_v)^*
\end{aligned}$$

Equation 6-58 for the cladding can also be further normalized by dividing the coefficients by the driving term which is the rod initial heat generation rate. After this operation, the different Pi groups become:

$$\Pi_{27} = \frac{\rho_{c,i} c_{p,ci} V_{ci} (T_{ci} - T_{co})}{\tau_c Q_i''' V_{fi}} = \frac{\text{Clad stored energy / time}}{\text{Heat generation rate}} \quad (6-59)$$

$$\Pi_{28} = \frac{1}{R_o^2} \frac{k_{c,i}(T_{ci} - T_{co})V_{ci}}{Q_i''' V_{fi}} = \frac{\text{Clad conduction heat rate}}{\text{Heat generation rate}} \quad (6-60)$$

$$\Pi_{29} = \frac{h_{gap,i} A_{t,i}(T_s - T_{ci})}{Q_i''' V_{fi}} = \frac{\text{Heat transfer rate from pellet to clad}}{\text{Heat generation rate}} \quad (6-61)$$

$$\Pi_{30} = \frac{h_{c,i} A_{c,i}(T_{co} - T_{sat})}{Q_i''' V_{fi}} = \frac{\text{Convective HT rate}}{\text{Heat generation rate}} \quad (6-62)$$

$$\Pi_{31} = \frac{h_{R,r/s,i} A_{R,r/s,i}(T_{co} - T_s)}{Q_i''' V_{fi}} = \frac{\text{Radiation HT rate to surfaces in bundle}}{\text{Heat generation rate}} \quad (6-63)$$

$$\Pi_{32} = \frac{h_{R,r/H,i} A_{R,r/H,i}(T_{co} - T_H)}{Q_i''' V_{fi}} = \frac{\text{Radiation HT rate to housing}}{\text{Heat generation rate}} \quad (6-64)$$

$$\Pi_{33} = \frac{h_{R,hr/cr,i} A_{R,hr/cr,i}(T_{co,hr} - T_{co,cr})}{Q_i''' V_{fi}} = \frac{\text{Radiation HT rate from hot rods to cold rods}}{\text{Heat generation rate}} \quad (6-65)$$

$$\Pi_{34} = \frac{h_{\ell w,i} A_{\ell w,i} (T_{co} - T_{sat})}{Q_i''' V_{fi}} = \frac{\text{Liquid contact HT rate}}{\text{Heat generation rate}} \quad (6-66)$$

$$\Pi_{35} = \frac{h_{R,r/d,i} A_{R,r/d,i} (T_{co} - T_{sat})}{Q_i''' V_{fi}} = \frac{\text{Radiation HT rate to entrained drops}}{\text{Heat generation rate}} \quad (6-67)$$

$$\Pi_{36} = \frac{h_{R,r/v,i} A_{R,r/v,i} (T_{co} - T_v)}{Q_i''' V_{fi}} = \frac{\text{Radiation HT rate to vapor}}{\text{Heat generation rate}} \quad (6-68)$$

One can replace the radiation heat transfer representation by a more complex model which will include the material dependent emissivity. The radiation heat transfer equations can also be replaced with a calculation of the heat flow by this path within the bundle. This will be presented in Section 7.

The Pi groups presented in Equations 6-54 to 6-57 and 6-59 to 6-68, are valid for either a nuclear rod or a heater rod in a test bundle, though differences exist due to the difference in materials between the fuel rods and the electrical heater rods. Also, there is an additional term, Π_{32} , which represents the radiation from the hot rods to the test facility housing. There is no housing in a PWR fuel assembly. This is a distortion in the test facility relative to an infinitely sized PWR fuel assembly and will be addressed in Section 7 of this report. The housing effect must also be addressed in the analysis of the test data. Also, computer simulations of the test will require a structure model for the housing since the wall will communicate directly with the fluid and both directly and indirectly by radiation heat transfer with the heater rods in the interior of the bundle.

6.3.3 Momentum Equation Scaling for the Rod Bundle Heat Transfer Test Facility

The generalized one-dimensional integral form of the momentum equation is given by Shames⁽⁶⁻¹¹⁾ and Wulff⁽⁶⁻⁴⁾ and is written for the entire test bundle as:

$$P_i - P_e = \frac{1}{g_c} \int_i^e \frac{dW}{dt} \frac{dz}{A} + \frac{1}{g_c} \left[\frac{1}{A^2} \left(\frac{W_e^2}{\rho_e} - \frac{W_i^2}{\rho_i} \right) \right] - \frac{g}{g_c} \int_i^e \rho dz + \frac{f}{2D_e \rho A^2 g_c} \int_i^e W|W| dz + \frac{k_T W^2}{\rho Q A^2 2 g_c} \quad (6-69)$$

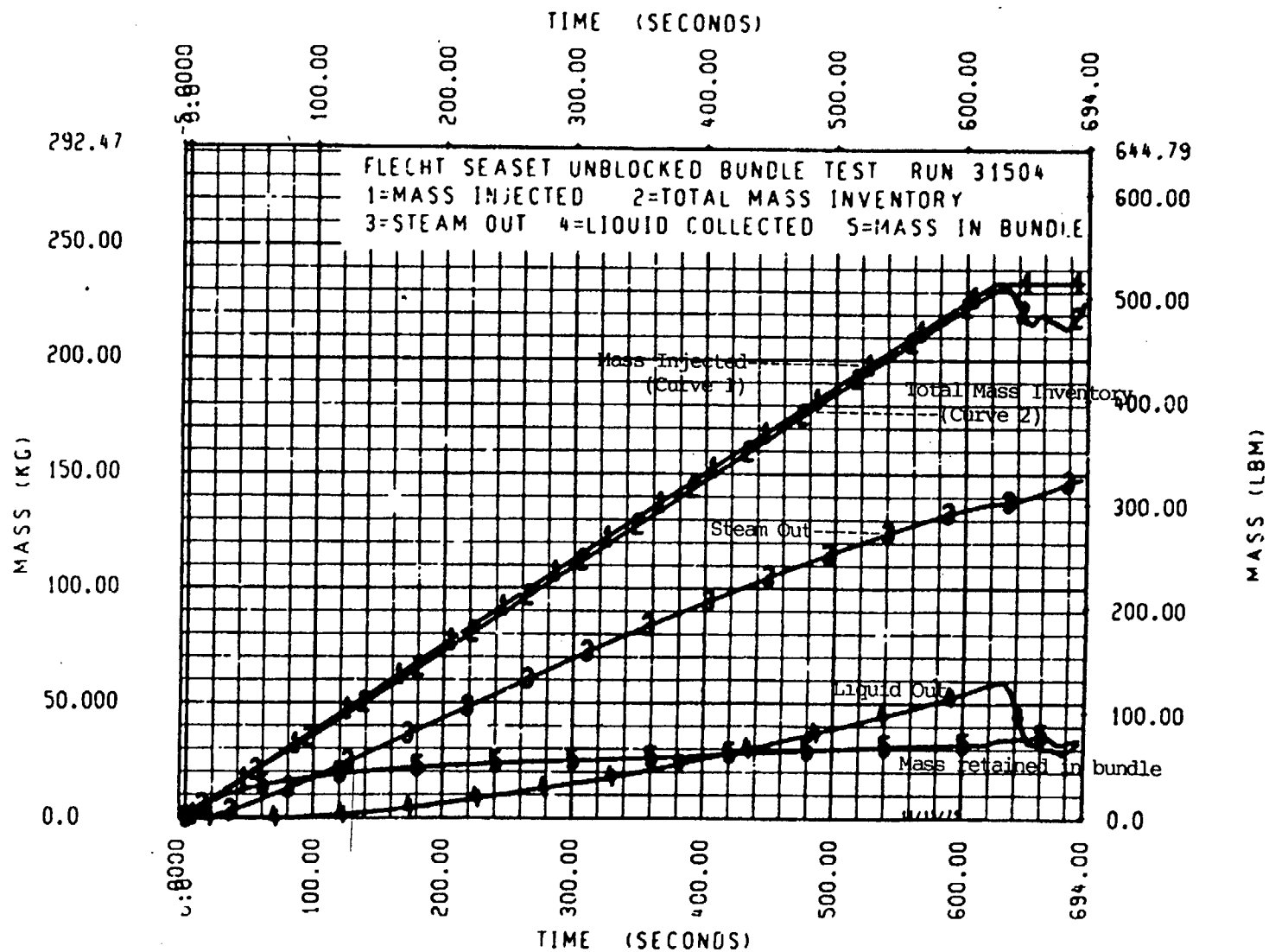
where the terms on the right hand side represent the

- inertia effects of the fluid in the volume,
- momentum flux of the fluid into and out of the volume,
- gravitational forces,
- frictional effects,
- form losses within the volume.

The nomenclature is given at the end of this section for these equations. The momentum equation can be written for the complete bundle from the inlet to the exit. The flow in the bundle is single phase for some length and two-phase over the remaining length. The inlet is assumed to be single phase while the exit has a dispersed two-phase mixture. The saturation point is assumed to be at same location within the bundle as the quench front. Assuming that the saturation point is at the quench front is a reasonable simplification since for most reflood situations with low flooding rates (typically 0.0254 m/s, 1 inch/second). The flow up to the quench front is assumed to be single phase while the flow downstream of the quench front is assumed to be in two-phase film boiling regime. Thus, the total bundle length can be split into a single phase region (from z_i to z_{sat}) and a two-phase region (from z_{sat} to z_e).

It is also assumed that the mass flow rate is only time dependent, and does not vary across the bundle cross section or along the length (this is approximately true for low flooding rate situations of interest in which the exit flows nearly equal the inlet flows). For constant low flooding rate situations, a nearly constant flow process occurs. Most of the flow which is injected into the bundle becomes entrained and flows out of the bundle as a steam/droplet mixture. Figure 6-1 shows the mass balance on FLECHT-SEASET test 31504, a 0.0254 m/s, 1-inch/sec, 40 psia, constant flooding rate test. Curve 1 represents the integrated injection, while curves 3 and 4 represent the integrated exit vapor and liquid flows respectively. The mass storage in the bundle is shown as curve 5 and is nearly horizontal indicating that only a portion of the injected water is stored in the bundle, while the remainder exits the bundle.

Figure 6-1: Mass Balance FLECHT-SEASET Run 31504.



If one examines the data at the very beginning of the test; this quasi-steady situation is not true and the rate of mass accumulation nearly equals the injection rate. However, once the quench front becomes developed, as seen in Figure 6-1, the flows are quasi-steady.

Operating on the inertia term gives

$$\frac{1}{g_c} \int_i^e \frac{dW}{dt} \frac{dz}{A} = \frac{1}{g_c} \frac{dW}{dt} \frac{1}{A} \int_i^e dz = \frac{dW}{dt} \left(\frac{L_T}{A} \right) \frac{1}{g_c} \quad (6-70)$$

where L_T is the total length of the bundle.

Operating on the momentum flux term gives

$$\frac{1}{g_c} \frac{1}{A^2} \left[\left(\frac{W_e^2}{\rho_e} \right) - \left(\frac{W_i^2}{\rho_i} \right) \right] = \frac{1}{g_c} \frac{W^2}{A^2} \left[\frac{1}{\rho_m} - \frac{1}{\rho_i} \right] \quad (6-71)$$

where the difference in the momentum flux is due to the density difference from the bundle inlet and exit. The density at the bundle exit is a mixture density ($\rho_e = \rho_m$) that reflects the two-phase flow behavior in the bundle during reflooding. This term is also called the acceleration pressure drop in two-phase flow.

The gravity term is integrated along the length of the bundle and represents the single and two-phase flow contributions to the total head in the bundle, therefore,

$$\frac{g}{g_c} \int_i^e \rho dz = \frac{g}{g_c} L_{1\phi} \bar{\rho}_\ell + \frac{g}{g_c} \int_{z_{sat}}^{z_e} \rho_m dz \quad (6-72)$$

where the single phase portion of the gravitational pressure drop uses an averaged fluid density from the subcooled inlet to the saturation density for the liquid, and the two-phase region uses a mixture density.

The gravity term can be expanded in the two-phase region by representing the mixture density as:

$$\rho_m = \alpha \rho_v + (1 - \alpha) \rho_f \quad (6-73)$$

Inserting Equation 6-73 into Equation 6-72, and using an average void fraction in the two-phase region gives

$$\frac{g}{g_c} \int_i^e \rho dz = \frac{g}{g_c} L_{1\phi} \bar{\rho}_\ell + \frac{g}{g_c} [\rho_v \bar{\alpha} + (1 - \bar{\alpha}) \rho_f] L_{2\phi} \quad (6-74)$$

The frictional terms and the form pressure loss terms can be combined for both the single phase flow region as well as the two-phase flow region assuming that the mass flow is vertically upward in the test section (the absolute sign disappears). Operating on the single phase frictional term gives

$$\frac{f}{2D_e \rho_\ell A^2 g_c} W^2 \int_{z_i}^{z_{sat}} dz = \frac{f L_{1\phi} W^2}{2D_e g_c A^2} \quad (6-75)$$

and for the two-phase frictional pressure drop, one obtains,

$$\frac{f}{D_e \rho_\ell A^2 z g_c} \int_{z_{sat}}^{z_e} W|W| dz = \frac{\overline{\phi_{fo}^2} f L_{2\phi} W^2}{D_e \rho_f A^2 z g_c} \quad (6-76)$$

where

$$\overline{\phi_{fo}^2} = \int_{z_{sat}}^{z_e} \phi_{fo}^2 dz \quad (6-77)$$

is the average two-phase flow multiplier over the two-phase flow region.

A similar approach can be used for the single and two-phase form losses in the bundle. The form losses represent the spacer grids within the bundle structure. Since the quench front is assumed to be at some intermediate position, there are a certain number of spacer grids which are in the single phase region and the remaining grids are in the two-phase region. There are typically eight (8) grids in the rod bundle. The total form loss is given as :

$$\frac{K_T W^2}{2\rho_\ell A^2 g_c} = \frac{n K_{1\phi} W^2}{2\rho_\ell A^2 g_c} + \frac{\overline{\phi_{fo}^2} m K_{1\phi} W^2}{2\rho_\ell A^2 g_c} \quad (6-78)$$

where 'n' and 'm' are the number of grids in the single-phase and two-phase region respectively.

The frictional and form losses can be combined for single and two-phase flow as

$$\frac{1}{\rho_\ell A^2 g_c} \left[\frac{fL_{1\phi}}{2D_e} + nK_{1\phi} \right] W^2 + \frac{1}{\rho_\ell A^2 g_c} \left[\overline{\phi}_{fo}^2 \left\{ \frac{fL_{2\phi}}{2D_e} + mK_{1\phi} \right\} \right] W^2 \quad (6-79)$$

Substituting Equations 6-70, 6-71, 6-74 and 6-79 into Equation 6-69 gives

$$P_1 - P_2 = \frac{1}{g_c A} \frac{dW}{dt} L_T + \frac{1}{g_c} \frac{W^2}{A^2} \left(\frac{1}{\rho_m} - \frac{1}{\rho_i} \right) - \left[\frac{g}{g_c} L_{1\phi} \overline{\rho}_\ell - \frac{g}{g_c} \left[\rho_v \overline{\alpha} + (1 - \overline{\alpha}) \rho_f \right] L_{2\phi} \right] \\ + \frac{W^2}{\rho_\ell A^2 g_c} \left[\frac{fL_{1\phi}}{2D_e} + nK_{1\phi} \right] + \frac{W^2}{\rho_\ell A^2 g_c} \left[\overline{\phi}_{fo}^2 \left(\frac{fL_{2\phi}}{2D_e} + mK_{1\phi} \right) \right] \quad (6-80)$$

We can define the total frictional and form resistance for single-phase as

$$R_{f1\phi} = \frac{fL_{1\phi}}{2D_e} + nK_{1\phi} \quad (6-81)$$

and for two-phase as

$$R_{f2\phi} = \overline{\phi}_{fo}^2 \left[\frac{fL_{2\phi}}{2D_e} + mK_{1\phi} \right] \quad (6-82)$$

This equation can be normalized using the initial condition and boundary condition parameters from Table 6-2 and Table 6-6 as

$$\frac{\Delta P^* W_i^2}{\rho_i A^2 2g_c} = \left(\frac{1}{g_c} \right) \frac{W_i^2}{A \rho_i} \frac{L_T L^*}{V_B A^*} \cdot \frac{dW^*}{dt^*} + \frac{W_i^2}{g_c A^2} \frac{1}{A^{*2} \rho_i} \left(\frac{1}{\rho_m^*} - \frac{1}{\rho_\ell^*} \right) W^{*2}$$

$$\begin{aligned}
& - \left[\frac{g}{g_c} L_T \rho_i L_{1\phi}^* \rho_\ell^* + \frac{g}{g_c} \left(\rho_v^* \rho_i \alpha^* \alpha_e + (1-\alpha)^* (1-\alpha_e) \rho_f^* \rho_i L_T L_{2\phi}^* \right) \right] \\
& + \frac{W_i^2}{\rho_\ell^* \rho_i A^2 A^{*2} g_c} \left[R_{f_{1\phi}}^* R_{f_{1\phi}} \right] W^{*2} + \frac{W_i^2}{\rho_i A^2} \frac{W^{*2}}{A^{*2} \rho_f^* g_c} \left[R_{f_{2\phi}}^* R_{f_{2\phi}} \right]
\end{aligned} \tag{6-83}$$

The bundle volume $V_B = A \cdot L_T$ can be used in equation 6-83.

Collecting the different terms and dividing by $\frac{gL_T \rho_i}{g_c}$, the maximum gravitational driving head in the bundle as the “driving term” as recommended by Wulff, gives:

$$\begin{aligned}
\frac{W_i^2}{\rho_i^2 A^2 2gL_T} \Delta P^* &= \frac{W_i^2}{\rho_i^2 A^2 2gL_T} \frac{dW^*}{dt^*} L^* + \frac{W_i^2}{g\rho_i^2 A^2 L_T} \left(\frac{1}{\rho_m^*} - \frac{1}{\rho_\ell^*} \right) \\
& - \left[L_{1\phi}^* \rho_\ell^* + \frac{\rho_{vs} \alpha_e}{\rho_i} \left(\rho_v^* \alpha^* L_{2\phi}^* \right) + \frac{\rho_{fs}}{\rho_i} (1-\alpha_e) \rho_f^* (1-\alpha)^* L_{2\phi}^* \right] \\
& + \frac{W_i^2}{\rho_i^2 A^2 gL_T} R_{f_{1\phi}}^* \cdot W^{*2} R_{f_{1\phi}}^* + \frac{W_i^2}{\rho_i^2 A^2 gL_T} R_{f_{2\phi}}^* W^{*2} R_{f_{2\phi}}^*
\end{aligned} \tag{6-84}$$

where the Pi groups are given as:

$$\Pi_{37} = \frac{W_i^2}{\rho_i^2 A^2 2gL_T} = \frac{\text{Velocity head}}{\text{Gravity head}} \tag{6-85}$$

$$\Pi_{38} = \frac{W_i^2 L_T}{A \rho_i V_B g L_T \rho_i} \quad \text{but, } V_B = AL_T, \text{ therefore}$$

$$\Pi_{38} = \frac{W_i^2}{A^2 \rho_i^2 gL_T} = \frac{\text{Velocity head}}{\text{Gravity head}} \tag{6-86}$$

$$\Pi_{39} = \frac{W_i^2}{A^2 \rho_i^2 g L_T} = \frac{\text{Velocity head}}{\text{Gravity head}} \quad (6-87)$$

$$\Pi_{40} = 1 \quad (6-88)$$

$$\Pi_{41} = \frac{\rho_{v_s} \alpha_e}{\rho_i} = \frac{\text{Vapor head}}{\text{Total head}} \quad (6-89)$$

$$\Pi_{42} = \frac{\rho_{fs} (1 - \alpha_e)}{\rho_i} = \frac{\text{Liquid head}}{\text{Total head}} \quad (6-90)$$

$$\Pi_{43} = \frac{W_i^2}{\rho_i^2 A^2 L_T g} R_{f_{1\phi}} = \frac{\text{Single phase resistance}}{\text{Gravity head}} \quad (6-91)$$

$$\Pi_{44} = \frac{W_i^2}{\rho_i A^2 L_T g_c} R_{f_{2\phi}} = \frac{\text{Two phase resistance}}{\text{Gravity head}} \quad (6-92)$$

Note that Π_{37} , Π_{38} , and Π_{39} are the same or are not independent and represent the velocity head or kinetic energy of the flow relative to the maximum gravity head. Since inlet fluid conditions, geometry, and energy addition are preserved between the test and the PWR fuel assembly, the PWR plant would have the same Pi groups and these in turn will have the same numerical value. Therefore, the test facility will correctly represent the inertia effects of the fluid, the momentum flux effects and the gravitational force effects.

Π_{40} , Π_{41} and Π_{42} represent the single-phase and two-phase gravity head terms in the momentum equation, relative to the maximum gravity head in the bundle.

Π_{43} represents the ratio of the single phase frictional and form pressure losses in the bundle to the maximum gravitational head in the bundle. Π_{44} represents the same ratio for the two-phase region within the bundle.

Comparing these terms to those for a PWR fuel assembly, differences can occur. If the spacer grids used in the test are prototypical, the form loss term will be the same for both the plant and the test. The frictional term, however, can be different since in the test there is a housing which adds additional wetted perimeter such that the hydraulic diameter is smaller for the same flow area. The smaller hydraulic diameter results in a lower Reynolds number for the same flow condition and hence a higher friction factor. The effects of the non-prototypical hydraulic effect of the test section housing will be calculated in Section 6.6. All the Pi groups are presented in Table 6-7.

Table 6-6

Normalizing Factors for Fluid Momentum Equation

$$A^* = \frac{A}{A_i}, \quad L^* = \frac{L}{L_T}, \quad L_{1\varphi}^* = \frac{L_{1\varphi}}{L_T}, \quad L_{2\varphi}^* = \frac{L_{2\varphi}}{L_T}$$

$$\Delta P = \frac{(P_1 - P_2)}{\left\{ \frac{W_i^2}{(2g_c A^2 \rho_i)} \right\}}, \quad R_{f_{1\varphi}}^* = \frac{R_{f_{1\varphi}}}{R_{f_{1\varphi i}}}, \quad R_{f_{2\varphi}}^* = \frac{R_{f_{2\varphi}}}{R_{f_{2\varphi i}}}$$

$$W^* = \frac{W}{W_i}, \quad \rho_l^* = \frac{\rho_l}{\rho_i}, \quad \rho_m^* = \frac{\rho_m}{\rho_i}$$

Table 6-7: Pi Groups for Fluid Energy Equation

Π_i	Definition	Ratio of
Π_1	$\frac{W_i c_{p,i} (T_{sat} - T_i)}{Q_{DP_i}}$	<u>Single phase fluid sensible energy/time</u> Initial decay power
Π_2	$\frac{W_i \rho_{v,sat,i} c_{p,v,sat,i} (T_{max,v} - T_{sat})}{\rho_i Q_{DP_i}}$	<u>Vapor sensible energy/time</u> Initial decay power
Π_3	$\frac{\rho_{r,i} c_{p,r,i} V_{r,q,i} (T_{max,r,q} - T_{sat})}{\tau_2 Q_{DP_i}}$	<u>Rod quench energy/time</u> Initial decay power
Π_4	$\frac{\rho_{H,i} c_{p,H,i} V_{H,q,i} (T_{min,H,q} - T_{sat})}{\tau_3 Q_{DP_i}}$	<u>Housing quench energy/time</u> Initial decay power
Π_5	$\frac{\rho_{g,i} c_{p,g,i} V_{g,q,i} (T_{min,g,q} - T_{sat})}{\tau_4 Q_{DP_i}}$	<u>Grid quench energy/time</u> Initial decay power
Π_6	$\frac{\rho_{DR,i} c_{p,DR,i} V_{DR,q,i} (T_{min,DR,q} - T_{sat})}{\tau_5 Q_{DP_i}}$	<u>Dead rod quench energy/time</u> Initial decay power
Π_7	$\frac{Q_{DP} _{1\phi}}{Q_{DP_i}} = 1$	<u>Heat generation rate</u> Initial decay power
Π_8	$\frac{h_s A_{r,i} (T_{max,r} - T_{sat})}{Q_{DP_i}}$	<u>Convective heat rate from rod to mixture vapor</u> Initial decay power

Π_9	$\frac{h_{R,r/v,i} A_{r,i} (T_{\max,r} - T_v)}{Q_{DP_i}}$	<u>Radiation heat rate from rods to vapor</u> Initial decay power
Π_{10}	$\frac{h_{R,r/d,i} A_{d,i} (T_{\max,r} - T_{sat})}{Q_{DP_i}}$	<u>Radiation heat rate from rod to drops</u> Initial decay power
Π_{11}	$\frac{h_s A_{H,i} (T_{\max,H} - T_{sat})}{Q_{DP_i}}$	<u>Convective heat rate from mixture to housing</u> Initial decay power
Π_{12}	$\frac{h_{R,v/H,i} A_{H,i} (T_{\max,H} - T_v)}{Q_{DP_i}}$	<u>Radiation heat rate from vapor to housing</u> Initial decay power
Π_{13}	$\frac{h_{R,H/d,i} A_{d,i} (T_{\max,H} - T_{sat})}{Q_{DP_i}}$	<u>Radiation heat rate from housing to drops</u> Initial decay power
Π_{14}	$\frac{h_s A_{g,i} (T_{\max,g} - T_{sat})}{Q_{DP_i}}$	<u>Convective heat rate from vapor to grids</u> Initial decay power
Π_{15}	$\frac{h_{R,v/g,i} A_{g,i} (T_{\max,g} - T_v)}{Q_{DP_i}}$	<u>Radiation heat rate from vapor to grids</u> Initial decay power
Π_{16}	$\frac{h_{R,g/d,i} A_{d,i} (T_{\max,g} - T_{sat})}{Q_{DP_i}}$	<u>Radiation heat rate from grids to drops</u> Initial decay power
Π_{17}	$\frac{h_s A_{DR,i} (T_{\max,DR} - T_{sat})}{Q_{DP_i}}$	<u>Convective heat rate from vapor to dead rods</u> Initial decay power
Π_{18}	$\frac{h_{R,v/DR,i} A_{DR,i} (T_{\max,DR} - T_v)}{Q_{DP_i}}$	<u>Radiation heat rate from vapor to dead rods</u> Initial decay power

Π_{19}	$\frac{h_{R,DR/d,i} A_{d,i} (T_{\max,DR} - T_{sat})}{Q_{DP_i}}$	<u>Radiation heat rate from dead rods to drops</u> Initial decay power
Π_{20}	$\frac{h_{l,i} A_d (T_{\max,v} - T_{sat})}{Q_{DP_i}}$	<u>Interfacial heat transfer rate</u> Initial decay power
Π_{21}	$\frac{h_{R,v/d,i} A_d (T_{\max,v} - T_{sat})}{Q_{DP_i}}$	<u>Radiation heat rate from vapor to drops</u> Initial decay power
Π_{22}	$\frac{W_i c_{p,i} (T_f - T_i)}{Q_{DP_i}}$	<u>Single phase fluid sensible energy</u> Initial decay power
Π_{23}	$\frac{W_o (h_s - h_g)}{Q_{DP_i}}$	<u>Exit mixture energy/time</u> Initial decay power

Table 6-7 (continued): Pi Groups for Rod Energy Equation

Π_i	Definition	Ratio of
Π_{24}	$\frac{\rho_{f,i} c_{p,f,i} (T_{f,CL} - T_s)}{\tau_f Q''_{f,i}}$	$\frac{\text{Stored energy/time}}{\text{Initial heat generation rate}}$
Π_{25}	$\frac{k_{f,i} (T_{f,CL} - T_s)}{R_f^2 Q''_{f,i}}$	$\frac{\text{Clad heat conduction rate}}{\text{Initial heat generation rate}}$
Π_{26}	1	$\frac{\text{Initial power}}{\text{Initial heat generation rate}}$
Π_{27}	$\frac{\rho_{c,i} V_{c,i} c_{p,ci} (T_{ci} - T_{co})}{V_{f,i} Q''_{f,i} \tau_c}$	$\frac{\text{Clad stored energy/time}}{\text{Heat generation rate}}$
Π_{28}	$\frac{k_{c,i} V_{c,i} (T_{ci} - T_{co})}{V_{f,i} Q''_{f,i} R_o^2}$	$\frac{\text{Clad heat conduction rate}}{\text{Heat generation rate}}$
Π_{29}	$\frac{h_{gap,i} A_{i,i} (T_s - T_{ci})}{V_{f,i} Q''_{f,i}}$	$\frac{\text{Heat transfer rate from pellet to clad}}{\text{Heat generation rate}}$
Π_{30}	$\frac{h_{c,i} A_{c,i} (T_{co} - T_{sat})}{V_{f,i} Q''_{f,i}}$	$\frac{\text{Convective HT rate}}{\text{Heat generation rate}}$
Π_{31}	$\frac{h_{R,r/s,i} A_{R,r/s,i} (T_{co} - T_s)}{V_{f,i} Q''_{f,i}}$	$\frac{\text{Radiation HT rate to surfaces in bundle}}{\text{Heat generation rate}}$

Π_{32}	$\frac{h_{R,r/H,i} A_{R,r/H,i} (T_{co} - T_H)}{V_{f,i} Q''_i}$	<u>Radiation HT rate to housing</u> Heat generation rate
Π_{33}	$\frac{h_{R,hr/cr,i} A_{R,hr/cr,i} (T_{co,hr} - T_{co,cr})}{V_{f,i} Q''_i}$	<u>Radiation HT rate from hot rods to cold rods</u> Heat generation rate
Π_{34}	$\frac{h_{lw,i} A_{lw,i} (T_{co} - T_{sat})}{V_{f,i} Q''_i}$	<u>Liquid contact HT rate</u> Heat generation rate
Π_{35}	$\frac{h_{R,r/d,i} A_{R,r/d,i} (T_{co} - T_{sat})}{V_{f,i} Q''_i}$	<u>Radiation HT rate to entrained drops</u> Fuel rod heat generation rate
Π_{36}	$\frac{h_{R,r/v,i} A_{R,r/v,i} (T_{co} - T_v)}{V_{f,i} Q''_i}$	<u>Radiation HT rate to vapor</u> Fuel rod heat generation rate

Table 6-7 (continued): Pi Groups for Fluid Momentum Equation

Π_i	Definition	Ratio of
$\Pi_{37} = \Pi_{38} = \Pi_{39}$	$\frac{W_i^2}{2\rho_i g A^2 L_T}$	<u>Velocity head</u> Gravity head
Π_{40}	1	<u>Maximum gravitational driving head</u> Total head
Π_{41}	$\frac{\rho_v \alpha_e}{\rho_i}$	<u>Vapor head</u> Total head
Π_{42}	$\frac{\rho_{f_s} (1 - \alpha_e)}{\rho_i}$	<u>Liquid head</u> Total head
Π_{43}	$\frac{W_i^2}{\rho_i g A^2 L_T} R_{f_{1\phi}}$	<u>Single phase resistance</u> Gravity head
Π_{44}	$\frac{W_i^2}{\rho_i g_c A^2 L_T} R_{f_{2\phi}}$	<u>Two phase resistance</u> Gravity head

6.4 Calculation of Pi groups for flow energy equation

6.4.1 Introduction

The fluid energy equation includes 23 π groups which are defined in Section 6.1. Here, the numerical values of these groups are calculated for the RBHT facility, the PWR bundle and BWR bundle.

The RBHT reference conditions, given in Table 6-8 are similar to FLECHT-SEASET experiment (Run 31504) conditions. Hence, reference conditions used in the calculations are obtained from FLECHT-SEASET and then applied to the geometry and materials for each case (RBHT, PWR and BWR).

Table 6-8: RBHT Program Conditions

Flooding rate, m/s (in/sec)	0.0254 (1.0)
Pressure, bar (psia)	2.67788 (40)
Inlet subcooling, °C (°F)	60 (140)
kW/m (kW/ft) at peak power location	2.3 (0.7)
Peaking factor	1.5

The fluid energy equation represent the energy balance for the fluid in the entire bundle at a given time which is selected to be the PCT time (this is 125 seconds in Run 31504). Measured values are then averaged axially to obtain the values to be used in the calculations which are shown in Table 6.9.

6.4.2 Calculation of Convective Heat Transfer Pi groups

The Pi groups for the fluid energy equation can be categorized mainly into quench energy terms, convective heat transfer terms and radiative heat transfer terms. The present section discusses the Pi groups of the fluid energy equation.

Table 6-9: Reference Conditions for the Fluid Energy Equation Pi groups

Exit Temperature, T_e , °C (°F)	260 (500)
Quench front location, m (ft)	1.2 (4.0)
Average clad temperature, T_c , °C (°F)	898.88 (1650)
Average housing temperature, T_H , °C (°F)	246.11 (475)
Average surface temperature, T_s , °C (°F)	246.11 (475)
Fluid saturation temperature, T_{sat} , °C (°F)	130.55 (267)
Average vapor temperature, T_{vapor} , °C (°F)	656.11 (1177)
Average thimble temperature, $T_{thimble}$, °C (°F)	746.66 (1376)
Average grid temperature, T_g , °C (°F)	746.66 (1376)
Exit void fraction, α_e	0.999

6.4.2.1 Methodology used for Calculations:

The following assumptions and simplifications were used in the analysis:

1. Data from FLECHT-SEASET experiment (Run 31504) with conditions similar to the RBHT facility were used, however, these values were applied to the RBHT facility geometry and power shape.
2. The maximum temperature encountered in the run occurred at 125 sec for channel 99. This was at an elevation of 1.98m (6'-6"). All other quantities from the FLECHT-SEASET, Run 31504 were obtained at this time (125 sec).
3. Quench front: The location of the quench front at 125 sec was obtained from the plot of quench front location vs. time in the FLECHT-SEASET report (Figure 6-6). At $t = 125$ s, the quench front was at the 1.2m (4 ft.) elevation. The quench front has been 'frozen' at this location for all calculations. In the calculation of the fluid energy equation Pi groups, all data used from FLECHT-SEASET report represents a snapshot in time, taken by freezing the quench front at that elevation (4 ft).
4. Time averaged values over 1.2m - 3.6m (4' - 12') of the heater rod clad temperature, vapor temperature and thimble temperature were used in the calculation of the Pi groups. For the housing temperature, the maximum value of the housing temperature at that time (125 sec) was used to provide a more realistic estimate of the Pi group value. This value is 410°C (770 F), obtained from the FLECHT SEASET report. The dummy rod

temperature was taken to be the same as the maximum housing temperature. The grid temperature was set equal to the thimble temperature.

5. The heat transfer coefficient value for convection, was the time average value obtained from data above the quench front location to the exit of the test section. This value was referenced to the fluid saturation conditions (T_{sat})
6. The exit void fraction was assumed to be 0.999.
7. Finally, the exit temperature was obtained from the FLECHT-SEASET plot for channel 199, which gives temperature of the vapor near the exit location 3.45m (11.5 ft). Thus $T_{exit} = 260^{\circ}\text{C}$ (500 F).

All values used in the calculations are summarized in Table 6-9.

6.4.2.2 Numerical Input Quantities:

Initial decay power:

$Q_{DPI} = 2.3 \text{ kW/m}$ (0.7 kW/ft), is the initial rod decay power (40 seconds into a LOCA) at the peak power location, which is equivalent to a value of 5.6 kW/rod using a peaking factor of 1.50. With 45 heated rods in the bundle, the total bundle power was 252 kW.

Inlet conditions:

Based on the information in Tables 6-8 and 6-9, the inlet properties were obtained from thermodynamic tables at a temperature of 52.77°C (127 F).

Areas of rods, housing, grids and dead rods above the quench front (4-feet):

- a. The total rod area is calculated based on rod diameter 9.55mm (0.374") and length above quench front 2.4m (8 ft) for 45 heated rods.
- b. The housing area is obtained from the product of the inner perimeter of the housing and the length of housing above the quench front.
- c. The total grid area is calculated based on the product of the following:

Area of each cell = 4 x pitch 12.6 mm (0.496") x height of the grid 38.1mm (1.5")
Number of cells per grid = 45
Number of grids stops above quench front = 6
- d. The total dummy rod area is based on the dummy rod diameter 9.5mm (0.374") and length above quench front 2.4m (8 ft) for four dummy rods.

6.4.2.3 Numerical Values of the Convection Pi groups:

The Pi groups representing the energy storage terms are

$$\Pi_1 = 0.144$$

$$\Pi_2 = 0.0007$$

For the convective energy terms for rods, housing, grids and dummy rods, a heat transfer coefficient of 56.78 W/m²-K (10 Btu/hr-ft²-F) was used, based on the average from the FLECHT-SEASET report (Run 31504) data. To give a more realistic value for the Pi group, $\Pi_{\theta\theta\epsilon}$ instead of average value of housing temperature, the maximum housing temperature of 410°C (770 F) at PCT time (125 sec), at the 6' elevation was used. Also, the maximum housing temperature 410°C (770 F) was for the value of T_{\max} of dummy rods.

Using the above information and the calculated areas, the Pi values for the various convective heat transfer terms are

$$\Pi_\lambda = 0.567$$

$$\Pi_{\theta\theta} = 0.055$$

$$\Pi_{14} = 0.072$$

$$\Pi_{17} = 0.019$$

The Pi group for the interfacial heat transfer is

$$\Pi_{20} = \frac{h_{l,i} A_d (T_{\max,v} - T_{sat})}{Q_{DPi}} = \frac{\text{Interfacial heat transfer rate}}{\text{Initial decay power}}$$

where A_d represents the interfacial area, given by the product of area of a single drop times the number of drops. The number of drops is given by

$$N_d = \frac{6(1 - \bar{\alpha})}{\pi d^3} \quad (6-93)$$

With a mean void fraction value of 0.995, and a drop diameter of 1.016mm (0.04"), the number of drops is

$$N_d = 9.104 \text{ drops/cm}^3 \text{ (149.2 drops/in}^3\text{)}$$

The quench front is at the 4' elevation, hence, the number of drops in the two-phase region which extends from the location of the quench front to the bundle exit is obtained by the product of the number of drops per unit volume times the volume above the quench front.

$$\text{Flow area} = 45.8 \text{ cm}^2. (7.0987 \text{ sq in.})$$

Hence, the total number of drops is calculated to be 101641.

From the FLECHT-SEASET report (Pg 6-26), the mean droplet velocity and mean vapor velocity are found as

$$\bar{u}_d = 6.555 \text{ m/sec (21.5 ft/sec)}$$

$$\bar{u}_v = 13.415 \text{ m/sec (44 ft/sec)}$$

The Reynolds number for drop based on the relative velocity of drops and vapor is given as:

$$\text{Re}_d = \frac{\rho_v d (\bar{u}_v - \bar{u}_d)}{\mu_v} \quad (6-94)$$

The droplet Reynolds Number is calculated to be 803.65

Taking a $\text{Pr}_v = 1.04$ (from Collier and Thome⁽⁶⁻¹²⁾) and using the Lee-Ryley Correlation, the Nusselt number is

$$\text{Nu}_d = 2 + 0.74 \text{Re}_d^{0.5} \text{Pr}_v^{1/3} \quad (6-95)$$

$$h_{l_{co}} = \frac{\text{Nu}_d k_v}{d} \quad (6-96)$$

where the thermal conductivity for vapor is obtained from Collier and Thome⁽⁶⁻¹²⁾ as

$$k_v = 0.02799027 \text{ W/m-K (0.01617 Btu/hr-ft-F)}$$

Based on these,

$$\Pi_{20} = 0.43$$

The flow energy Pi groups for exit energy is calculated assuming the exit mass flow is equal to the inlet mass flow. Value of saturated vapor enthalpy is used from thermodynamic tables at $P = 40 \text{ psia}$. Thus

$$\Pi_{22} = \Pi_1 = 0.144$$

$$\Pi_{23} = 0.121$$

From these, it is seen that the Pi groups representing the energy storage, the flow energy and convection from rod to vapor and the interfacial heat transfer terms are the dominant Pi groups. The other terms are very small by comparison. This clear distinction between the dominant terms and the others are in line with what is expected typically.

$$\Pi_4 = \frac{\rho_{H,i} c_{p,H,i} V_{H,q,i} (T_{\min,H,q} - T_{sat})}{\tau_3 Q_{DPi}} = \frac{\text{Housing quench energy / time}}{\text{Initial decay power}}$$

$$\Pi_5 = \frac{\rho_{g,i} c_{p,g,i} V_{g,q,i} (T_{\min,g,q} - T_{sat})}{\tau_4 Q_{DPi}} = \frac{\text{Grid quench energy / time}}{\text{Initial decay power}}$$

$$\Pi_6 = \frac{\rho_{DR,i} c_{p,DR,i} V_{DR,q,i} (T_{\min,DR,q} - T_{sat})}{\tau_5 Q_{DPi}} = \frac{\text{Dead rod quench energy / time}}{\text{Initial decay power}}$$

6.4.3
Quench
Energy

groups

The Pi groups describing the heat transfer at the quench front for the rods, the housing, the grids and the surfaces (dummy rods) are the following:

The calculation is based on the input data from in Table 6-8 and 6-9 and the methodology used in Section 6.4.2.1. In addition, the following assumptions have been made to complete the calculation:

- The same transition boiling heat transfer coefficient of $h_{q,i} = 5.678 \text{ kW/m}^2\text{-K}$ (1000 Btu/hr-ft²-F) is assumed for the structures (rods, housing, grids and surfaces);
- The same $T_{\min} = 550^\circ\text{C}$ (1022 F) is assumed for all surfaces;
- The same axial quench front velocity u_q is assumed for all the structures.

where the same value of T_{\min} has been used for all surfaces since the material is all Inconel. The material properties and geometry data used in the calculation are summarized in the following tables (6-10, 6-11, 6-12, 6-13).

Table 6-10: Material Properties

Material	Reference Temperature (C)	Density (kg/m ³)	Heat Capacity (J/kg-K)	Conductivity (W/m-K)
Inconel-600	1100	8254	696	24.7
Boron Nitride	1100	1910	1500	86.3
Monel K-500	1100	8470	531	34.4
Uranium Dioxide	1100	9649	326	3.9
Zircaloy-2	1100	6560	362	16.8

Table 6-11: Electrical Rod Geometry

Material	r_i (mm, in)	dr_i (mm, in)
Boron Nitride	0, 0	1.7145, 0.0675
Monel K-500	1.7145, 0.0675	1.143, 0.0450
Boron Nitride	2.8575, 0.1125	1.1811, 0.0465
Inconel-600	4.0386, 0.1590	0.7112, 0.0280
Rod surface	4.7498, 0.1870	

Table 6-12: Nuclear Rod Geometry for PWR

Material	r_i (mm, in)	dr_i (mm, in)
Uranium Dioxide	0, 0	4.18084, 0.1646
Zircaloy-2	4.18084, 0.1646	0.56896, 0.0224
Rod surface	4.7498, 0.1870	

Table 6-13: Nuclear Rod Geometry for BWR

Material	r_i (mm, in)	dr_i (mm, in)
Uranium Dioxide	0, 0	5.199, 0.2047
Zircaloy-4	5.199, 0.2047	0.810, 0.0319
Rod surface	6.0198, 0.2370	

At first we need to calculate the volume of the rod which is quenching. This is related to the assumed quench front velocity, (v_q) and the heat structure time constant to release the stored energy:

$$V_r = A_{s,r} v_q \tau_2 \quad (6-97)$$

where, $A_{s,r}$ is the cross section of one of the heater rods and is given as

$$A_{s,r} = N_r \left(\frac{\pi}{4} D_r^2 \right) \quad (6-98)$$

This expression, when substituted in the definition of Π_3 gives

$$\Pi_3 = \frac{\rho_r c_{p,r} A_{s,r} v_{q,r} \tau_2 (T_{\min,r} - T_{sat})}{Q_{DP_i} \tau_2} \quad (6-99)$$

Note that the time constant drops out. This is because, regardless the time constant, most of the stored energy will be released during the quenching time period. In other words, if the time constant is larger, then the energy release rate will be lower but the energy will be released by a larger volume as the quench front is advancing over the same time period. This follows from the assumption that the quench front velocity is constant.

A similar procedure is used to calculate Π_4 , i.e. the energy released during quenching of the housing

$$\Pi_4 = \frac{\rho_{H,i} c_{p,H,i} V_{H,q,i} (T_{\min,H,q} - T_{sat})}{\tau_3 Q_{DP_i}} \quad (6-100)$$

Similarly for the grid

$$\Pi_5 = \frac{\rho_{g,i} c_{p,g,i} V_{g,q,i} (T_{\min,g,q} - T_{sat})}{\tau_4 Q_{DP_i}} \quad (6-101)$$

where

$$A_{s,g} = 4 \left(p \times \frac{s}{2} \right) \times 45 \quad (6-102)$$

p is the pitch and s is the strop thickness.

Finally for the dummy (corner rods):

$$\Pi_6 = \frac{\rho_{DR,i} c_{p,DR,i} V_{DR,q,i} (T_{\min,DR,q} - T_{sat})}{\tau_5 Q_{DP_i}} \quad (6-103)$$

where

$$A_{s,DR} = N_{DR} \left(\frac{\pi}{4} D_{DR}^2 \right) \quad (6-104)$$

N_{DR} is the number of dead rods (in our case, 4).

Details of the calculations are reported in Appendix B7. The values of the Π_i groups are the following:

$$\Pi_3 = 0.092$$

$$\Pi_4 = 0.084$$

$$\Pi_5 = 0.022$$

$$\Pi_6 = 0.003$$

6.4.4 Thermal Radiation Heat Transfer Π_i group calculation

The Π_i groups describing the radiative heat transfer to the fluid from the structures are:

Π_9 to Π_{16} . These terms require particular attention because in order to obtain these values, the solution of a radiative surface network is required. Thermal radiation heat transfer takes place between the rod surfaces, between rod and housing, between any surface to steam and droplets and between steam and droplets directly. For a given temperature field (clad, dummy rods,

housing, liquid and vapor) the heat rates among the surfaces, liquid and vapor are calculated by solving a radiation network lumped model (using the RADNET Fortran computer program).

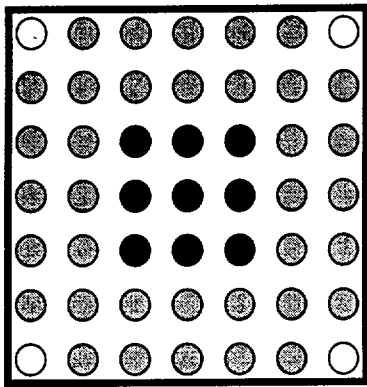
In this model, rods are lumped together and global surface view factors are calculated by combining single rod view factors obtained with the VUEFAC subroutine of the MOXY computer program⁽⁶⁻¹¹⁾. Details of the view factors calculation are reported in Appendix B.1.

To account for a radial temperature distribution in the bundle, a six node radiation network has been developed, where the heater rods are divided in hot rods and cold rods (Figure 6-2). The hot rods are considered to be either the single center rod, the inner 3x3 array or the inner 5x5 array. Sensitivity analysis (Appendix B.1) have been carried out and the inner 3x3 hot rods lumping approach was chosen to be the most appropriate.

The radiation network (Figure 6-3) resistances are calculated as described in Reference 6.8 and Appendix B.1 while the temperature at each network node surfaces is an input for the program. The node surface temperatures are calculated by averaging measured temperature in Run 31504 of

... ?
where the rest?

Figure 6-2

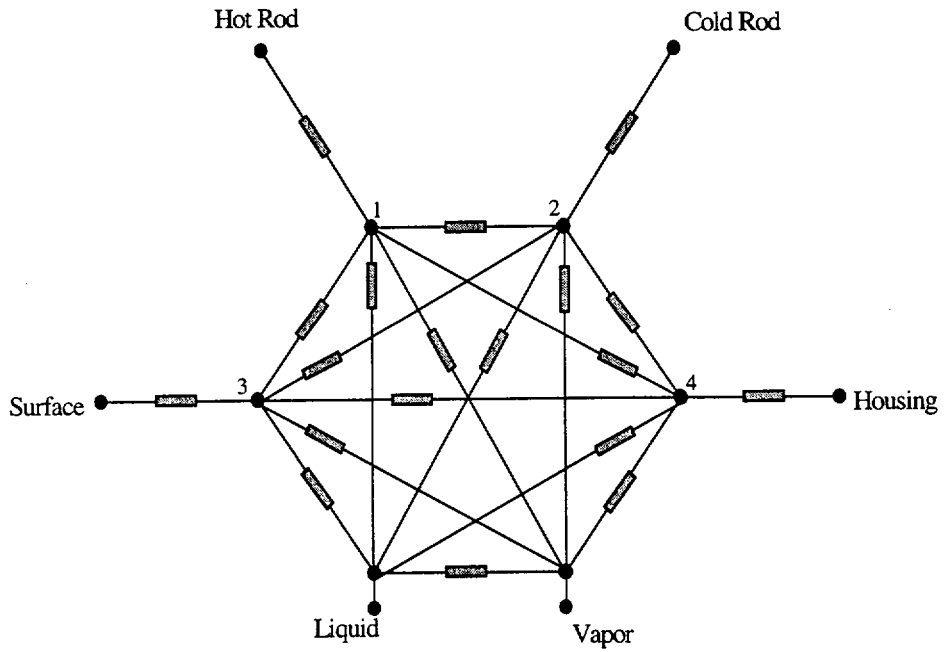


RBHT Layout

- Hot Rod
- Nominal Rod
- Dummy Rod
- Housing

Figure 6-3

Six Node Radiation Network



FLECHT-SEASET experiments. These values are summarized in Table 6-9. Once the temperature is assigned to each radiative surface, the radiation network is solved for the heat rate (per unit length) between each node. In particular, the Pi groups concerned with radiation are redefined below:

$$\Pi_9 = \frac{h_{R,r/v,i} A_{r,i} (T_{\max,r} - T_v)}{Q_{DP_i}} = \frac{Q'_{r/v} (z_{top} - z_q)}{Q_{DP_i}} \quad (6-105)$$

$$\Pi_{10} = \frac{h_{R,r/d,i} A_{d,i} (T_{\max,r} - T_{sat})}{Q_{DP_i}} = \frac{Q'_{r/d} (z_{top} - z_q)}{Q_{DP_i}} \quad (6-106)$$

$$\Pi_{12} = \frac{h_{R,v/H,i} A_{H,i} (T_{\max,H} - T_v)}{Q_{DP_i}} = \frac{Q'_{v/H} (z_{top} - z_q)}{Q_{DP_i}} \quad (6-107)$$

$$\Pi_{13} = \frac{h_{R,H/d,i} A_{d,i} (T_{\max,H} - T_{sat})}{Q_{DP_i}} = \frac{Q'_{H/d} (z_{top} - z_q)}{Q_{DP_i}} \quad (6-108)$$

$$\Pi_{15} = \frac{h_{R,v/g,i} A_{g,i} (T_{\max,g} - T_v)}{Q_{DP_i}} = \frac{Q'_{v/g} \Delta z_g N_g}{Q_{DP_i}} \quad (6-109)$$

$$\Pi_{16} = \frac{h_{R,g/d,i} A_{d,i} (T_{\max,g} - T_{sat})}{Q_{DP_i}} = \frac{Q'_{g/d} \Delta z_g N_g}{Q_{DP_i}} \quad (6-110)$$

$$\Pi_{18} = \frac{h_{R,v/DR,i} A_{DR,i} (T_{\max,DR} - T_v)}{Q_{DP_i}} = \frac{Q'_{DR/v} (z_{top} - z_q)}{Q_{DP_i}} \quad (6-111)$$

$$\Pi_{19} = \frac{h_{R,DR/d,i} A_{d,i} (T_{\max,DR} - T_{sat})}{Q_{DP_i}} = \frac{Q'_{DR/d} (z_{top} - z_q)}{Q_{DP_i}} \quad (6-112)$$

$$\Pi_{21} = \frac{h_{R,v/d,i} A_d (T_{\max,v} - T_{sat})}{Q_{DP_i}} = \frac{Q'_{v/d} (z_{top} - z_q)}{Q_{DP_i}} \quad (6-113)$$

where

- z_{top} - Elevation to the top of the bundl, 3.6m(12 ft).
- z_q - Elavation of the quench front, 1.2m at 125 sec (4 ft at 125 sec).
- Δz_g - Grid axial length, 38.1mm (1.5 in).
- N_g - Number of grids above quench front

The solution of the radiation network provides the radiosity or emissive power in each node, then the Q_{ij} values in each branch can be calculated by applying the definition

$$Q_{ij} = \frac{J_i - J_j}{R_{ij}} \text{ or } Q_{ij} = \frac{J_i - E_{b,j}}{R_{ij}} \quad (6-114)$$

The 6 nodes network requires two clad temperature values: the hot rod temperature and the cold rod temperature. The temperature difference between the hot rods and the cold rods is estimated from the rod-to-rod (MOXY) radiation model and is 161 F when a 3x3 inner hot rods lumping approach in the bundle is assumed. Then the hot and cold rod temperature are calculated

$$\frac{9T_{hr} + 36T_{cr}}{45} = \bar{T} = 1650 \quad (6-115)$$

since

$$T_{cr} = T_{hr} - \Delta T = T_{hr} - 161$$

we obtain

$$T_{hr} = 970.55^\circ \text{C} (1779 \text{ F})$$

$$T_{cr} = 880.55^\circ \text{C} (1617 \text{ F})$$

This completes the input data for the radiation network. The dimensionless group Π_9 is the radiative energy from all the rods to the vapor and is expressed as

$$\Pi_9 = \frac{Q'_{r/v} \Delta z}{Q_{DP_i}}$$

where the numerator has the units of heat rate per unit length and is the sum of two contributions: energy from hot rods to vapor and energy from nominal rods to vapor.

As already mentioned the difference Δz is the height above the quench front

$$\Delta z = z_{top} - z_q$$

and

$$Q'_{r/v} = Q'_{1v} + Q'_{2v}$$

The initial bundle decay power is:

$$Q_{DP_i} = 252.0 \text{ kW}$$

As results we obtain

$$\Pi_9 = 8.55e^{-4}$$

Similarly the Pi group for the radiative energy from the rod to the liquid droplets is calculated as:

$$\Pi_{10} = \frac{Q'_{r/d} \Delta z}{Q_{DP_i}}$$

where

$$Q'_{r/d} = Q'_{1d} + Q'_{2d}$$

and

$$\Pi_{10} = 7.06e^{-2}$$

The next two dimensionless groups represent the radiative heat transfer from the housing to the vapor and droplets respectively

$$\Pi_{12} = \frac{Q'_{v/H} \Delta z}{Q_{DP_i}} \quad \text{and} \quad \Pi_{13} = \frac{Q'_{H/d} \Delta z}{Q_{DP_i}}$$

where

$$Q'_{v/H} = Q'_{4v}$$

$$Q'_{H/d} = Q'_{4d}$$

and then

$$\Pi_{12} = -8.01e^{-5}$$

$$\Pi_{13} = 2.85e^{-3}$$

The next two Pi groups for the radiative energy from the grids to the fluid are calculated by solving a separate four node radiation network (Figure 6-4). The Pi groups are defined as

$$\Pi_{15} = \frac{Q'_{v/g} \Delta z_g N_g}{Q_{DP_i}} \quad \text{and} \quad \Pi_{16} = \frac{Q'_{g/d} \Delta z_g N_g}{Q_{DP_i}}$$

where

$$Q'_{v/g} = \frac{J_2 - \sigma T_v^4}{R_{2v}}, \quad Q'_{g/d} = \frac{J_2 - \sigma T_d^4}{R_{2d}}$$

and J_2 and R_{2v} refer to four nodes radiation network. The grid vertical length and the number of grids above the quench front are

$$\Delta z_g = 1.5 \text{in} \quad \text{and} \quad N_g = 6$$

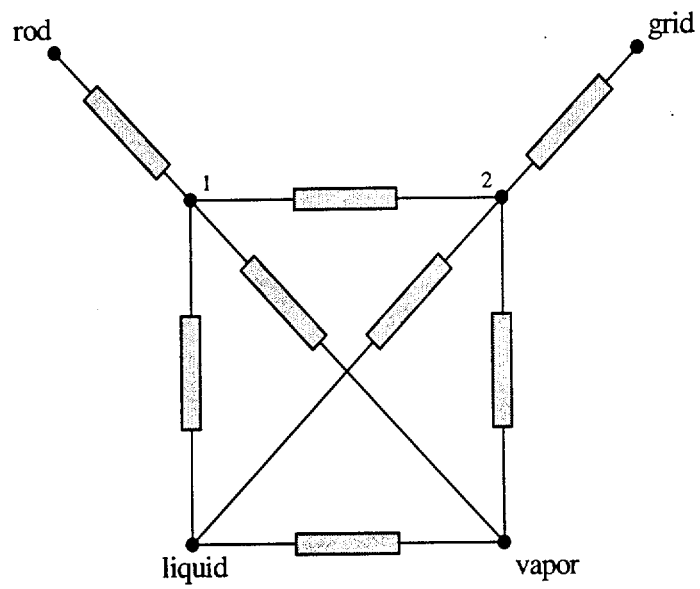
The rod-grid-liquid-vapor network resistances are calculated with the same procedure and equations described for the bundle six-node-radiation network. In this case there are only two unknowns (J_1 and J_2) which can be determined explicitly. Details of the calculation are reported in the Excel worksheet attached in Appendix B.2. The result is

$$\Pi_{15} = 6.9e^{-7}$$

$$\Pi_{16} = 0.0016$$

Figure 6-4

Four Node Radiation Network



Finally, the radiation energy from the surfaces (unheated rods) to the fluid are represented by

$$\Pi_{18} = \frac{Q'_{v/DR} \Delta z}{Q_{DP_i}} \quad \text{and} \quad \Pi_{19} = \frac{Q'_{DR/d} \Delta z}{Q_{DP_i}}$$

where

$$Q'_{v/DR} = Q'_{3v} \quad \text{and} \quad Q'_{DR/d} = Q'_{3d}$$

as results:

$$\Pi_{18} = -3.22e^{-5} \quad \text{and} \quad \Pi_{19} = 6.5e^{-4}$$

The last contribution to the radiative heat transfer is expressed by the interfacial radiation heat transfer

$$\Pi_{21} = \frac{Q'_{v/d} \Delta z}{Q_{DP_i}}$$

which is determined directly from the network with the result that

$$\Pi_{21} = 3.9e^{-5}$$

6.4.5 Summary

Table 6-14 shows the numerical values of all the Pi groups for the fluid energy equation. As expected, stored energy, rod quench energy, convection from rod to vapor, interfacial heat transfer and flow energy terms are significant. The values of the radiation Pi groups are relatively small, thereby indicating the predominance of convection over radiation heat transfer. Though the rod quench energy term is significant, the housing, grid and the dummy rod quench energy terms are small.

Table 6-14: Numerical Values of Pi Groups - Fluid Energy Equation

Π_i	Definition	Ratio of	Value for RBHT	Value for PWR	RBHT PWR	Value for BWR	RBHT BWR
Π_1	$\frac{W_i c_{p,i} (T_{sat} - T_i)}{Q_{DP_i}}$	<u>Single phase fluid sensible energy/time</u> Initial decay power	0.144	0.144	1	0.144	1
Π_2	$\frac{W_i \rho_{v,sat,i} c_{p,v,sat,i} (T_{max,v} - T_{sat})}{\rho_i Q_{DP_i}}$	<u>Vapor sensible energy/time</u> Initial decay power	0.000	0.000	Insignificant*	0.000	Insignificant*
Π_3	$\frac{\rho_{r,i} c_{p,r,i} V_{r,q,i} (T_{max,r,q} - T_{sat})}{\tau_2 Q_{DP_i}}$	<u>Rod quench energy/time</u> Initial decay power	0.092	0.066	1.394	0.105	0.876
Π_4	$\frac{\rho_{H,i} c_{p,H,i} V_{H,q,i} (T_{min,H,q} - T_{sat})}{\tau_3 Q_{DP_i}}$	<u>Housing quench energy/time</u> Initial decay power	0.084	0	Does not exist as Π term for PWR is zero	0.009	Insignificant*
Π_5	$\frac{\rho_{g,i} c_{p,g,i} V_{g,q,i} (T_{min,g,q} - T_{sat})}{\tau_4 Q_{DP_i}}$	<u>Grid quench energy/time</u> Initial decay power	0.022	0.009	Insignificant*	0.012	Insignificant*
Π_6	$\frac{\rho_{DR,i} c_{p,DR,i} V_{DR,q,i} (T_{min,DR,q} - T_{sat})}{\tau_5 Q_{DP_i}}$	<u>Dead rod quench energy/time</u> Initial decay power	0.003	0.001	Insignificant*	0.000	Insignificant*
Π_7	$\frac{Q_{DP} _{1\phi}}{Q_{DP_i}}$	<u>Heat generation rate</u> Initial decay power	1	1	1	1	1

Π_8	$\frac{h_s A_{r,i} (T_{\max,r} - T_{sat})}{Q_{DP_i}}$	<u>Convective heat rate from rod to mixture vapor</u> Initial decay power	0.567	0.567	1	0.719	1.268
Π_9	$\frac{h_{R,r/v,i} A_{r,i} (T_{\max,r} - T_v)}{Q_{DP_i}}$	<u>Radiation heat rate from rods to vapor</u> Initial decay power	0.000	0.000	Insignificant*	0.000	Insignificant*
Π_{10}	$\frac{h_{R,r/d,i} A_{d,i} (T_{\max,r} - T_{sat})}{Q_{DP_i}}$	<u>Radiation heat rate from rod to drops</u> Initial decay power	0.071	0.074	0.959	0.116	0.612
Π_{11}	$\frac{h_s A_{H,i} (T_{\max,H} - T_{sat})}{Q_{DP_i}}$	<u>Convective heat rate from mixture to housing</u> Initial decay power	0.055	0	Does not exist as Π term for PWR is zero	0.07	0.786
Π_{12}	$\frac{h_{R,v/H,i} A_{H,i} (T_{\max,H} - T_v)}{Q_{DP_i}}$	<u>Radiation heat rate from vapor to housing</u> Initial decay power	0.000	0	Does not exist as Π term for PWR is zero	0.000	Insignificant*
Π_{13}	$\frac{h_{R,H/d,i} A_{d,i} (T_{\max,H} - T_{sat})}{Q_{DP_i}}$	<u>Radiation heat rate from housing to drops</u> Initial decay power	0.000	0	Does not exist as Π term for PWR is zero	0.000	Insignificant*
Π_{14}	$\frac{h_s A_{g,i} (T_{\max,g} - T_{sat})}{Q_{DP_i}}$	<u>Convective heat rate from vapor to grids</u> Initial decay power	0.072	0.072	1	0.093	0.774

Π_{15}	$\frac{h_{R,v/g,i} A_{g,i} (T_{\max,g} - T_v)}{Q_{DP_i}}$	<u>Radiation heat rate from vapor to grids</u> Initial decay power	0.000	0.000	Insignificant*	0.000	Insignificant*
Π_{16}	$\frac{h_{R,g/d,i} A_{d,i} (T_{\max,g} - T_{sat})}{Q_{DP_i}}$	<u>Radiation heat rate from grids to drops</u> Initial decay power	0.002	0.002	1	0.002	1
Π_{17}	$\frac{h_s A_{DR,i} (T_{\max,DR} - T_{sat})}{Q_{DP_i}}$	<u>Convective heat rate from vapor to dead rods</u> Initial decay power	0.019	0.019	1	0.023	0.826
Π_{18}	$\frac{h_{R,v/DR,i} A_{DR,i} (T_{\max,DR} - T_v)}{Q_{DP_i}}$	<u>Radiation heat rate from vapor to dead rods</u> Initial decay power	0.000	0.000	Insignificant*	0.000	Insignificant*
Π_{19}	$\frac{h_{R,DR/d,i} A_{d,i} (T_{\max,DR} - T_{sat})}{Q_{DP_i}}$	<u>Radiation heat rate from dead rods to drops</u> Initial decay power	0.000	0.000	Insignificant*	0.000	Insignificant*
Π_{20}	$\frac{h_{I,i} A_d (T_{\max,v} - T_{sat})}{Q_{DP_i}}$	<u>Interfacial heat transfer rate</u> Initial decay power	0.43	0.43	1	0.43	1
Π_{21}	$\frac{h_{R,v/d,i} A_d (T_{\max,v} - T_{sat})}{Q_{DP_i}}$	<u>Radiation heat rate from vapor to drops</u> Initial decay power	0.000	0.000	Insignificant*	0.000	Insignificant*
Π_{22}	$\frac{W_i c_{p,i} (T_f - T_i)}{Q_{DP_i}}$	<u>Single phase fluid sensible energy</u> Initial decay power	0.144	0.144	1	0.144	1
Π_{23}	$\frac{W_o (h_s - h_g)}{Q_{DP_i}}$	<u>Exit mixture energy/time</u> Initial decay power	0.121	0.121	1	0.121	1

* - Both numbers are very small, so the ratio is insignificant

6.5 Calculations of Pi groups for the Rod Energy Equation

6.5.1 Introduction

The rod energy equation includes thirteen Pi groups (from Π_{24} to Π_{36}) defined earlier. The numerical values of these groups are now calculated for the RBHT facility. The reference conditions used in the calculation are obtained from the same FLECHT-SEASET experiment (Run 31504) used earlier and then applied to the geometry and materials for each case (RBHT, PWR and BWR).

The rod energy equation represents an energy balance at a given axial location within the dispersed flow film boiling region, far from the quench front at the time of the measured peak temperature. The conditions (temperature, H.T. coefficients etc.) are taken from FLECHT-SEASET (Run 31504) measured values at the time of PCT and at the PCT axial location. Since there are no data available for the dummy rods, their surface temperature is assumed equal to the housing temperature. The complete list of data and assumptions is given in Table 6-15.

6.5.2 Convection and Stored Energy Pi groups

These Pi groups are $\Pi_{24}, \Pi_{25}, \Pi_{26}, \Pi_{27}, \Pi_{28}, \Pi_{29}, \Pi_{30}, \Pi_{34}$. The values of the Pi groups are calculated for both the electric rod and the nuclear rod. The reference conditions and the input that is used in the calculation are tabulated in Table 6-15. Both types of rods are modeled as infinite cylinders. The temperature at the various locations such as centerline, surface, clad inside and clad outside surface are calculated simply by applying the concepts of conduction resistance for cylindrical geometries.

Table 6-15: Reference conditions for Rod Energy Equation Pi groups

Rod peak power, kW/m (kW/ft)	2.3 (0.7)
PCT time (sec)	125
PCT axial location, m (ft)	1.95 (6.5)
Clad temperature (PCT), T_{ci} °C (F)	1148.88 (2100)
Housing temperature, T_H °C (F)	426.66 (800)
Surface temperature, T_s °C (F)	426.66 (800)
Saturation temperature, T_{sat} °C (F)	130.55 (267)
Vapor temperature, T_v °C (F)	898.88 (1650)
Gap heat transfer coefficient, kW/m ² K (Btu/hr-ft ² -F)	
h_{gap} (Nuclear Rod)	5.678 (1000)
h_{gap} (Electrical Rod)	28.39 (5000)

To account for the correct heat transfer, based on the maximum temperature difference ($T_{CL} - T_{sat}$), the value of the heat transfer coefficient is taken to be $h = 56.78 \text{ W/m}^2\text{-K}$ ($10 \text{ Btu/hr-ft}^2\text{-F}$). This is again based on the same FLECHT-SEASET (Run 31504) data.

Also, to simulate the gap that exists between the inside of the clad and the fuel pellet or the boron nitride insulator, a gap heat transfer coefficient is used.

For electrical rods, $h_{gap} = 28.39 \text{ kW/m}^2\text{K}$ ($5000 \text{ Btu/hr-ft}^2\text{-F}$)
 For nuclear rods, $h_{gap} = 5.678 \text{ kW/m}^2\text{K}$ ($1000 \text{ Btu/hr-ft}^2\text{-F}$)

which are representative values for these rods

The heat generation rate per unit volume, Q_i''' is calculated from the kW/ft rating at peak location 2.3 kW/m (0.7 kW/ft) and the diameter of the fuel element, $D_f = 9.5 \text{ mm}$ ($0.374''$). We get $Q_i''' = 1.469 \times 10^8 \text{ W/m}^3$ ($4329012.6 \text{ Btu/hr-ft}^3$).

Material properties tabulated in Tables 6-10 and the dimensions of the electrical rod from Table 6-11 are used for the calculation of the Pi terms.

The fuel time constant τ_f and clad time constant τ_c are obtained by solving a double-lumped model for the rod. Three time constants are calculated from this model that represent respectively the fuel resistance (UO_2 or BN and Monel), the clad resistance and the film resistance. Results are reported in the following table 6-16:

Table 6-16: Comparison of Calculated Time Constants

Time constant (sec)	RBHT	PWR	BWR
Fuel, τ_f	0.55	3.99	5.98
Clad, τ_c	0.36	0.68	1.15
Film, τ_{film}	0.74	0.24	0.36

The time constant of the fuel τ_f and of the clad τ_c are used in groups Π_{24} and Π_{27} , respectively.

The calculation of the Π_{34} group defining direct contact heat transfer requires some explanation,

$$\Pi_{34} = \frac{h_{\ell w,i} A_{\ell w,i} (T_{co} - T_{sat})}{Q_i''' V_{fi}} = \frac{\text{Liquid contact HT rate}}{\text{Heat generation rate}}$$

To calculate the direct contact heat transfer for the dispersed droplet field, the Forsland

Rohsenow correlation is used as follows

$$q_{dcht}'' = (0.2)(1.276)(1 - \alpha_v)^{2/3} \left[\frac{g \rho_f \rho_g H_{fg}^* k^3}{(T_w - T_{sat}) \mu_g D_d} \right]^{1/4} (T_w - T_{sat}) \quad (6-116)$$

In the calculations, it is assumed that the liquid is saturated such that $H_{fg}^* = h_{fg}$.

The properties are evaluated at 60 psia and the calculations are performed for different void fractions and wall superheats. The droplet area is calculated assuming a uniform distribution of drops. Only drops within a diameter of the rod can interact. The number of drops is given by

$$N_d = \frac{6(1 - \bar{\alpha})}{\pi d^3} \quad (6-117)$$

With a mean void fraction value of 0.995, and a drop diameter of 0.04", the number of drops is calculated as

$$N_d = 9.104 \text{ drops/cm}^3 \text{ (149.2 drops/in}^3\text{)}$$

The drops (max) that can interact with the rod are those which are within one drop diameter of the rod surface.

$$\text{Rod diameter} = 9.5 \text{ mm (0.374")}$$

$$\text{Rod diameter} + \text{diameter of two drops} = 0.374" + 2(0.04") = 11.53 \text{ mm (0.454")}$$

$$\text{Area of the region occupied by two drops} = (22/7)(0.454^2 - 0.374^2) = 33.55 \text{ sq. mm (0.052 sq in.)}$$

$$\text{Subchannel area} = (\text{pitch})^2 - \text{area of rod} = 88.135 \text{ sq. mm (0.13661 sq in.)}$$

The area fraction of the drops that can hit the rod is the ratio of the area occupied by two drops to the subchannel area.

$$\text{Area fraction} = 0.052/0.13661 = 0.395$$

From the information of the area fraction and the number of drops per cubic inch, the resultant number of drops that can contact the wall is calculated as

$$(0.395)(149.2) = 59 \text{ drops.}$$

Since only one side of a drop contacts the rod, the total contact area is given as:

Total contact area = 0.5 (spherical area per drop)(Resultant number of drops) = 95.66 sq. mm (0.14828 sq in.)

Knowing all the values for the variables in equation 6-116, the heat flux is calculated for various values of $(T_w - T_{sat})$. From this, the heat transfer coefficient can also be calculated. For the Pi group calculation, the values of heat transfer coefficient, the contact area and the heat generation rate are known. The numerical value of the Pi group can be evaluated for various values of $(T_{co} - T_{sat})$, each time using the appropriate value of h. The value of Π_{34} tabulated in the result is for a temperature difference of 537.77°C (1000F.) The calculated Pi values are given below.

Table 6-17: Convection and Stored Energy Pi groups for Electrical/Nuclear rod

Π group	Electrical Rod	Nuclear Rod <i>PWR</i>
Π_{24}	0.965	1.180
Π_{25}	0.182	0.182
Π_{26}	1	1
Π_{27}	0.110	0.04
Π_{28}	0.016	0.016
Π_{29}	0.73	0.73
Π_{30}	0.73	0.73
Π_{34}	0.005	0.005

6.5.3 Thermal Radiation Heat Transfer Pi groups

The radiative heat transfer from the rod is expressed by the terms $\Pi_{31}, \Pi_{32}, \Pi_{33}, \Pi_{35}, \Pi_{36}$. The reference rod for which the energy balance is described, is assumed to be a rod in the central region of the bundle, specifically in the inner 3x3 sub-array. These Pi groups describe the radiative heat transfer from the hot rod to dummy rods, to housing, to liquid droplets, to vapor and to the nominal rods in the outer region of the bundle. Due to the housing, the outer region of the bundle will be at a lower temperature compared to the inner region. This will cause a radial temperature distribution across the bundle which will drive rod-to-rod radiative heat transfer from the center region. A detailed model to address this phenomena has been developed and is described in Section 7.

The same phenomenon exists for the Pi groups for the rod equation, as

$$\Pi_{31} = \frac{h_{R,r/s,i} A_{R,r/s,i} (T_{co} - T_s)}{Q_o''' V_{fi}} = \frac{Q_{r/s}}{Q_o''' V_{fi}} \quad (6-118)$$

$$\Pi_{32} = \frac{h_{R,r/H,i} A_{R,r/H,i} (T_{co} - T_H)}{Q_o''' V_{fi}} = \frac{Q_{r/H}}{Q_o''' V_{fi}} \quad (6-119)$$

$$\Pi_{33} = \frac{h_{R,hr/cr,i} A_{R,r/H,i} (T_{co,hr} - T_{co,cr})}{Q_o''' V_{fi}} = \frac{Q_{hr/cr}}{Q_o''' V_{fi}} \quad (6-120)$$

$$\Pi_{35} = \frac{h_{R,r/d,i} A_{R,r/d,i} (T_{co} - T_{sat})}{Q_o''' V_{fi}} = \frac{Q_{r/d}}{Q_o''' V_{fi}} \quad (6-121)$$

$$\Pi_{36} = \frac{h_{R,r/v,i} A_{R,r/v,i} (T_{co} - T_v)}{Q_o''' V_{fi}} = \frac{Q_{r/v}}{Q_o''' V_{fi}} \quad (6-122)$$

These dimensionless groups are calculated by solving the six node radiative network already discussed in the previous section. In this case, a different set of boundary conditions is used from previously discussed (Table 6-2).

The radiative heat transfer from the rod to the surfaces (unheated rods) is described by

$$\Pi_{31} = \frac{Q_{r/s}}{Q_o''' V_{fi}}$$

where $Q_{r/s}$ and $Q_o'''V_{fi}$ have both dimensions of heat rate per unit length. The heat rate $Q_{r/s}$ is the energy flowing from one of the hot rods (inner 3x3) to the dummy rods and the normalization factor $Q_o'''V_{fi}$ is based to the peak power location:

$$Q_o'''V_{fi} = 0.7 \text{ kW/ft} = 2296 \text{ W/m} \quad (6-123)$$

From the network solution

$$Q_{r/s} = Q_{13}$$

The heat rate is identically zero since the view factor from the inner 3x3 rods to the unheated rods at the corners is identically zero. As a consequence the resistance R_{12} becomes infinite, and

$$\Pi_{31} = 0.0$$

The same procedure is applied for the calculation of the next Pi group representing the direct radiative heat transfer from the rod to the housing

$$\Pi_{32} = \frac{Q_{r/H}}{Q_o'''V_{fi}}$$

where

$$Q_{r/H} = Q_{14}$$

which gives

$$\Pi_{32} = 0.0272$$

The radiative heat transfer from the hot rod to the cold rods (rod-to-rod) radiation is expressed by

$$\Pi_{33} = \frac{Q_{hr/cr}}{Q_o'''V_{fi}}$$

where

$$Q_{hr/cr} = Q_{12}$$

which gives

$$\Pi_{33} = 0.388$$

The heat rate from the hot rod to the droplet and the vapor is described respectively by

$$\Pi_{35} = \frac{Q_{r/d}}{Q_o^m V_{fi}}$$

$$\Pi_{36} = \frac{Q_{r/v}}{Q_o^m V_{fi}}$$

From the network, $Q_{r/d}$ and $Q_{r/v}$ are

$$Q_{r/d} = Q_{1l}$$

$$Q_{r/v} = Q_{1v}$$

the calculated result becomes

$$\Pi_{35} = 0.154$$

$$\Pi_{36} = 7.88e^{-4}$$

The results of the calculations are summarized in Table 6-18. As seen in the table, the rod-to-rod radiative heat transfer (hot rod to cold rod) is the largest contribution. This term can also be seen as an indirect path for radiative heat transfer from the inner rods to the housing. In fact the housing reduces the temperature of the external rods because of radiation heat transfer. This generates a radial temperature gradient among the rods which drives energy from the inner region to the outer region of the bundle. This effect is more prototypical for a BWR than a PWR fuel assembly due to the fuel channel used for BWRs, and will be discussed further.

This analysis overestimates the effect of the housing because the housing thermal resistance in the azimuthal direction is not considered since only one node is used to simulate the housing. To model this effect, the housing must be split in many separate surfaces with each surface thermally connected by azimuthal conductivity. This has been done in the more detailed COBRA-TF subchannel model described in Section 9. The COBRA-TF results indicate that the corners of the housing are at a lower temperature than the rest of the housing temperature predicted by the BUNDLE simple conduction model. In other words, for the same heat stored in the housing the more exposed portion of the housing surface will be at an higher temperature than predicted by a single surface model. This will reduce the heat removed by radiation from the heater rods.

6.5.4 Summary

The Pi groups obtained for the rod energy equation indicate that the significant terms are the convective heat transfer to the surrounding fluid, the radiation from hot rod to cold rod and radiation to entrained drops. Property differences between the electrical rod and the nuclear rod exist and hence the Pi groups involving the properties of the rods are different. One particular Pi group, Π_{24} , is about 20% higher for the nuclear rod. This is because of the low thermal conductivity of UO_2 and also due to the fact that at start up, a nuclear rod has very high amount of stored energy. The effect of this difference will be discussed in Section 7.

Table 6-18: Numerical Values of Pi Groups - Rod Energy Equation

Π_i	Definition	Ratio of	Value for RBHT	Value for PWR	<u>RBHT</u> PWR	Value for BWR	<u>RBHT</u> BWR
Π_{24}	$\frac{\rho_{f,i} c_{p,f,i} (T_{f,CL} - T_s)}{\tau_f Q''_{f,i}}$	<u>Stored energy/time</u> Initial heat generation rate	0.965	1.180	0.818	1.160	0.832
Π_{25}	$\frac{k_{f,i} (T_{f,CL} - T_s)}{R_f^2 Q''_{f,i}}$	<u>Clad heat Conduction rate</u> Initial heat generation rate	0.182	0.182	1.0	0.11	1.655
Π_{26}	1	<u>Initial power</u> Initial heat generation rate	1	1	1	1	1
Π_{27}	$\frac{\rho_{c,i} V_{c,i} c_{p,c,i} (T_{ci} - T_{co})}{V_{f,i} Q''_{f,i} \tau_c}$	<u>Clad stored energy/time</u> Heat generation rate	0.110	0.040	2.75	0.051	2.157
Π_{28}	$\frac{k_{c,i} V_{c,i} (T_{ci} - T_{co})}{V_{f,i} Q''_{f,i} R_o^2}$	<u>Clad conduction heat rate</u> Heat generation rate	0.016	0.016	1	0.009	1.778
Π_{29}	$\frac{h_{gap,i} A_{i,i} (T_s - T_{ci})}{V_{f,i} Q''_{f,i}}$	<u>Heat transfer rate from pellet to clad</u> Heat generation rate	0.73	0.73	1	0.565	1.292
Π_{30}	$\frac{h_{c,i} A_{c,i} (T_{co} - T_{sat})}{V_{f,i} Q''_{f,i}}$	<u>Convective HT rate</u> Heat generation rate	0.73	0.73	1	0.556	1.313
Π_{31}	$\frac{h_{R,r/s,i} A_{R,r/s,i} (T_{co} - T_s)}{V_{f,i} Q''_{f,i}}$	<u>Radiation HT rate to surfaces in bundle</u> Heat generation rate	0.00	0.235	0	0.336	0

Π_{32}	$\frac{h_{R,r/H,i} A_{R,r/H,i} (T_{co} - T_H)}{V_{f,i} Q''_i}$	<u>Radiation HT rate to housing</u> Heat generation rate	0.027	0	Does not exist as Π term for PWR is zero	0.030	0.9
Π_{33}	$\frac{h_{R,hr/cr,i} A_{R,hr/cr,i} (T_{co,hr} - T_{co,cr})}{V_{f,i} Q''_i}$	<u>Radiation HT rate from hot rods to cold rods</u> Heat generation rate	0.388	0.064	6.063	0.324	1.197
Π_{34}	$\frac{h_{lw,i} A_{lw,i} (T_{co} - T_{sat})}{V_{f,i} Q''_i}$	<u>Liquid contact HT rate</u> Heat generation rate	0.005	0.005	1	0.005	1
Π_{35}	$\frac{h_{R,r/d,i} A_{R,r/d,i} (T_{co} - T_{sat})}{V_{f,i} Q''_i}$	<u>Radiation HT rate to entrained drops</u> Fuel rod heat generation rate	0.154	0.159	0.969	0.259	0.595
Π_{36}	$\frac{h_{R,r/v,i} A_{R,r/v,i} (T_{co} - T_v)}{V_{f,i} Q''_i}$	<u>Radiation HT rate to vapor</u> Fuel rod heat generation rate	0.000	0.001	Insignificant*	0.00	Insignificant*

* - Both numbers are very small, so the ratio is insignificant.

6.6 Calculation of Pi groups for Flow Momentum Equation

The flow momentum equation Pi groups are calculated using the given inlet conditions of 40 psia, 140 F subcooling, and flooding rate (1 inch/sec) and flow area. The inlet is assumed to be single phase and the exit is dispersed two-phase mixture. The quench front is assumed to be at the 1.2 m (4 ft.) elevation and two grids are underwater, therefore, there are six grids in the two phase region. Hydraulic diameter is calculated based on the wetted perimeter and flow area. Based on this hydraulic diameter, the Reynolds number and the single phase friction factor ($f = 64/Re$) are calculated.

For two phase frictional pressure drop, all the two phase mixture is assumed to be liquid, so that two-phase multiplier can be used. The exit void fraction is taken to be 0.999. For an average quality of 50% and low pressure conditions, it is appropriate to assume an average two phase flow multiplier $\overline{\phi_{fo}^2}$, to be 100.

Table 6-19 shows numerical values for all the Pi groups for the fluid momentum equation.

Table 6-19: Fluid Momentum Π groups

Π group	Value
$\Pi_{37} = \Pi_{38} = \Pi_{39}$	$8.9e^{-6}$
Π_{40}	1
Π_{41}	0.002
Π_{10}	$9.5e^{-4}$
Π_{11}	$2.05e^{-4}$
Π_{44}	0.05

The only Pi group of significance is Π_{40} , which represents the liquid gravity head pressure drop. All other non dimensional groups are insignificant by comparison. This was expected since the differential pressure cells have been used to infer average void fraction in previous FLECHT and FLECHT-SEASET experiments because the fractional and acceleration effects are small.

The calculated Pi groups, along with their definitions are reported in Table 6-20.

Table 6-20: Numerical Values of Pi Groups - Fluid Momentum Equation

Π_i	Definition	Ratio of	Value for RBHT	Value for PWR	RBHT PWR	Value for BWR	RBHT BWR
$\Pi_{37} = \Pi_{38} = \Pi_{39}$	$\frac{W_i^2}{2\rho_i g A^2 L_T}$	<u>Velocity head</u> Gravity head	0.000	0.000	1 (Identical numbers, very close to zero)	0.000	1 (Identical numbers, very close to zero)
Π_{40}	1	<u>Maximum gravitational driving head</u> Total head	1	1	1	1	1
Π_{41}	$\frac{\rho_{v_s} \alpha_e}{\rho_i}$	<u>Vapor head</u> Total head	0.002	0.002	1	0.002	1
Π_{42}	$\frac{\rho_{f_s} (1 - \alpha_e)}{\rho_i}$	<u>Liquid head</u> Total head	0.000	0.000	1 (Identical numbers, very close to zero)	0.000	1 (Identical numbers, very close to zero)
Π_{43}	$\frac{W_i^2}{\rho_i g A^2 L_T} R_{f_{1\phi}}$	<u>Single phase resistance</u> Gravity head	0.000	0.000	1 (Identical numbers, very close to zero)	0.000	1 (Identical numbers, very close to zero)
Π_{44}	$\frac{W_i^2}{\rho_i g_c A^2 L_T} R_{f_{2\phi}}$	<u>Two phase resistance</u> Gravity head	0.050	0.048	1.042	0.048	1.042

6.7 Calculation of PWR and BWR Pi groups

6.7.1 Introduction

Pi groups calculated for the RBHT test facility, a PWR and BWR assembly are given in Tables 6-14, 6-18 and 6-20. The values obtained were compared, and distortions due to scaling identified. Using this approach, it can be seen whether or not the RBHT facility replicated prototypic behavior. The closer the values of the Pi group are for the test facility and the PWR or the BWR, the more similar is the behavior. The Pi groups which are not dependent on the material properties but only on the fluid conditions should be similar. Those Pi groups, which are a function of the material properties, will be different for the test facility and the PWR or the BWR, since the material properties are different.

Table 6-3 compares the different Pi groups for the test and a PWR fuel assembly and indicates possible test distortions relative to the fuel assembly being modeled. These comparisons indicate that many of the Pi terms are preserved since the rod bundle geometry models that of a PWR fuel assembly, and the initial conditions are preserved in the tests relative to the reactor. However, there is no housing in the PWR fuel assembly. So to ensure similarity, the Pi groups which represent the heat transfer processes associated with the housing must be small relative to the other transport terms in Equation 6-26.

Similarly Table 6-4 compares the Pi groups for the test facility to the Pi groups for the BWR fuel assembly. Since the BWR assembly has a channel surrounding the fuel rods, the same terms and Pi groups derived for the Rod Bundle Test Facility are also present for the BWR fuel assembly. The terms can have different magnitudes since the materials are different between the test and the BWR fuel assembly.

6.7.2 Calculation of Pi groups for PWR

The Pi groups for the fluid energy, which represent the flow energy, energy storage, convection to rods, housing, grids and dummy rods were evaluated for a PWR. Firstly, there is no housing for a PWR, hence the convection heat transfer from the vapor to the housing is zero. Those Pi groups which are dependent only on the flow conditions and independent of the material properties, will be the same for the test facility and the PWR, since the geometry, including the dimensions of rods, grids etc for the test facility and the PWR are the same.

Therefore, the fluid energy storage, flow energy, and convection Pi groups are all identical for the PWR. Thus, the only Pi groups that will be different are the quench terms and those involving radiation heat transfer.

The PWR quench energy groups Π_3 , Π_4 , Π_k and Π_{κ} are calculated using the same method as for the RBHT facility, however, the PWR core material properties and geometry are used (Zircaloy, UO_2 etc.). Note that in this case the housing is not present and the scaling group describing the quench of the housing is zero by definition. The calculated values are reported in Table 6-14.

The thermal radiation Pi groups for the PWR are calculated with a modified version of the RADNET computer program to account for the typical Westinghouse 17x17 rod bundle geometry. In a PWR, the housing is not present and only portion of the core section is considered. The situation assumed in the calculation is that of a hot assembly surrounded by eight colder assemblies as depicted in Figure 6-5. To reduce the size of the problem, this core portion(nine assemblies) is assumed to be 90 degrees symmetric. Moreover because of the geometry, radiation from the hot assembly cannot penetrate beyond seven rows into the cold rods. This reduces the problem to a 15x15 array. Thimbles location are described in the same Figure 6-5. At this point the VUEFAC subroutine of the MOXY code is used to calculate the single rod-to-rod view factors matrix and these values are combined to produce the global view factors. The node surface areas, are calculated in the computer program RADNET, as described in Appendix B.1.

To simulate the absence of the housing in a PWR core, the resistances from each node to node 4 in the network are set to a very large number (practically infinite). Then the same node temperatures for the RBHT facility are applied at the network external nodes and the program is solved for the radiosity in the other nodes. Finally, following the same procedure utilized for the RBHT case, the PWR fluid energy equation Pi groups for radiation heat transfer are calculated.

The numerical values for PWR Pi groups for the radiation terms for the fluid energy and rod energy equations are shown in Tables 6-14 and 6-18.

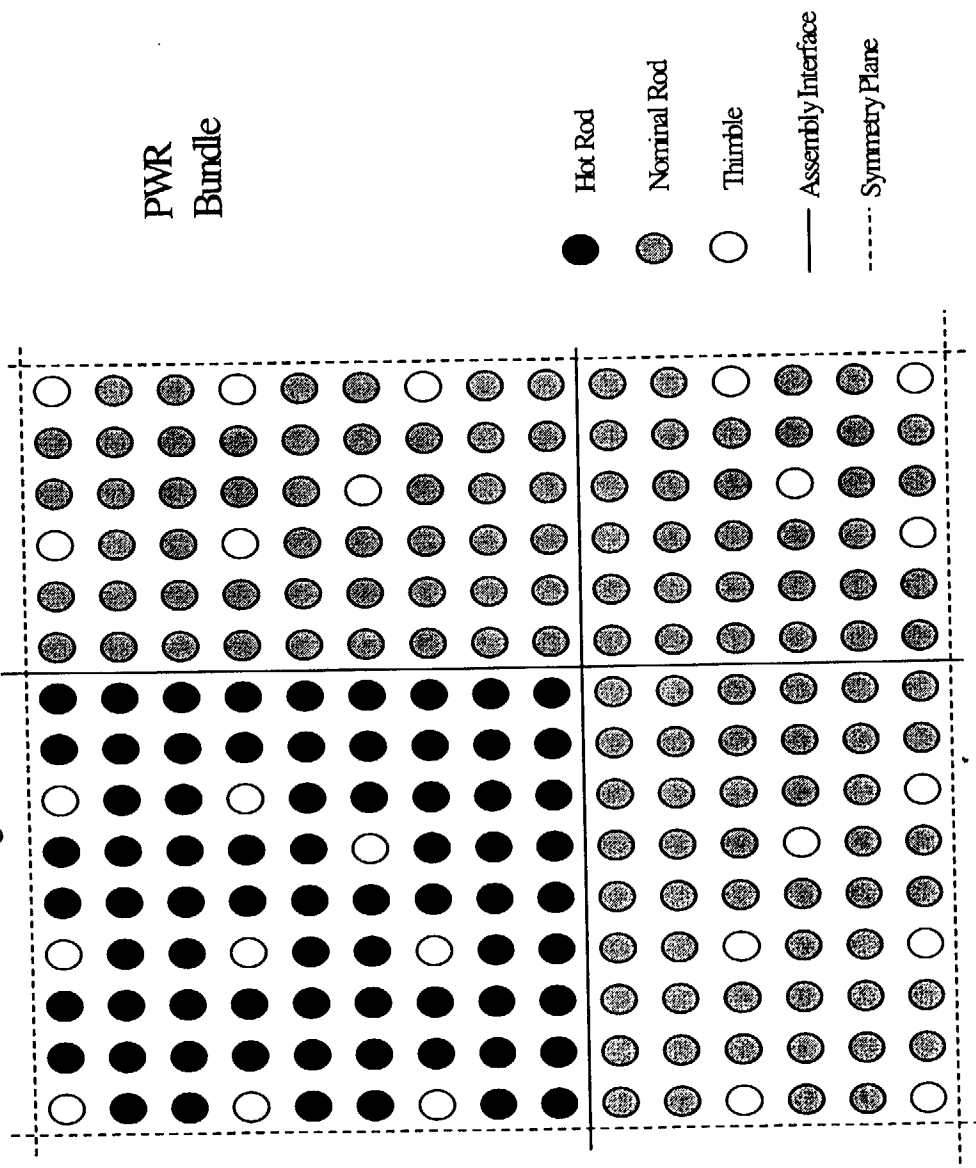
Similar to the RBHT, the fluid momentum Pi groups are calculated for the PWR and results are reported in Table 6-20.

The Pi group for the interfacial heat transfer will be the same for the test facility, PWR and BWR. Comparing these terms to that for the test facility, minor differences can be seen. The spacer grids used in the test are prototypical, so the form loss term will be the same for both the plant and the test. The frictional term, however, can be different since in the test there is a housing which adds additional wetted perimeter such that the hydraulic diameter is smaller for the same flow area. The smaller hydraulic diameter results in a lower Reynolds number for the same flow condition and hence a higher friction factor, but the differences in the values are quite small. The emissivity of Inconel 600 is slightly lower than Zircaloy and this causes some differences in radiation terms.

6.7.3 Calculation of Pi groups for BWR

The Pi groups for the fluid energy, which represent the flow energy, energy storage, convection to rods, housing, grids and dead rods have been evaluated for a BWR. Since the BWR fuel assembly is surrounded by a channel, which acts as a housing, the Pi groups related to the housing are not zero as in a PWR. It should be noted that the Pi groups which are dependent only on the flow conditions and independent of the material properties and geometry are the same for the RBHT facility and the BWR fuel assembly.

Figure 6-5: PWR Bundle Lumping Approach



In the fluid energy equation, based on the above, it is evident that the Pi groups representing the fluid energy storage terms and, the flow energy terms, Π_1 , Π_2 , Π_7 , Π_{22} and Π_{23} , will be the same as that of the test facility, as they depend only on the flow conditions. The interfacial heat transfer term, (Π_{20}) will also be the same as it depends only on the fluid condition and the number of drops. The Pi groups for the convection to rod, housing, grid and dead rod will be different because of a different rod diameter for a BWR fuel rod.

The stored energy and convection terms for the rod energy equation Pi groups for BWR are somewhat different because the dimensions of the rod is different for a BWR compared to a PWR. Also the time constants for the cladding and the fuel are higher for a BWR. These Pi groups are presented in Tables 6-14 and 6-18.

The BWR quench energy groups are calculated by the same method used for the RBHT facility, using BWR core material properties and geometry (Zircaloy, UO_2 etc.). For simplicity, the same T_{\min} is assumed in the calculation for both Zircaloy and Inconel. Note that in this case the housing is represented by the channel walls. The quench energy Pi groups for the BWR are shown in Table 6-14.

To calculate the thermal radiation Pi groups for the BWR, the RADNET computer program was modified to account for the different bundle geometry typical of a typical GE 8x8 rod bundle. In this case the housing is represented by the channel walls. The situation assumed in the calculation is a 4x4 hot assembly surrounded by two rows of colder assembly as depicted in Figure 6-6. The cold surfaces are the two water rod in the center of the channel. The VUEFAC subroutine of the MOXY code is used to calculate the single rod-to-rod view factors matrix and then by combining properly these values, the global view factors and node surface area are calculated in the RADNET computer program, as described in Appendix B.1 for the RBHT facility.

The same nodes temperature used for the RBHT facility are applied at the network external nodes and the program solves for the radiosity in the other nodes. Finally, following the same procedure utilized for the RBHT case, we calculate the BWR fluid energy equation Pi groups for the radiation heat transfer. The numerical values are reported in Tables 6-14 and 6-18.

The Pi groups for the fluid momentum equation for the BWR will be the same as that of a PWR, based on the conditions of flooding rate of 1 inch/sec.

6.8 Conclusions

The fluid energy equation, the rod energy equation and the bundle fluid momentum equations have been developed for the Rod Bundle Heat Transfer test facility. These equations were made dimensionless using the initial and boundary conditions such that dimensionless Pi groups were developed to examine similitude between the Rod Bundle Heat Transfer test facility and a PWR and a BWR fuel assembly. From the scaling analysis, it is found that the presence of a test housing leads to extra Pi groups for this structure relative to a PWR fuel assembly, thereby indicating that distortion in the test is possible.

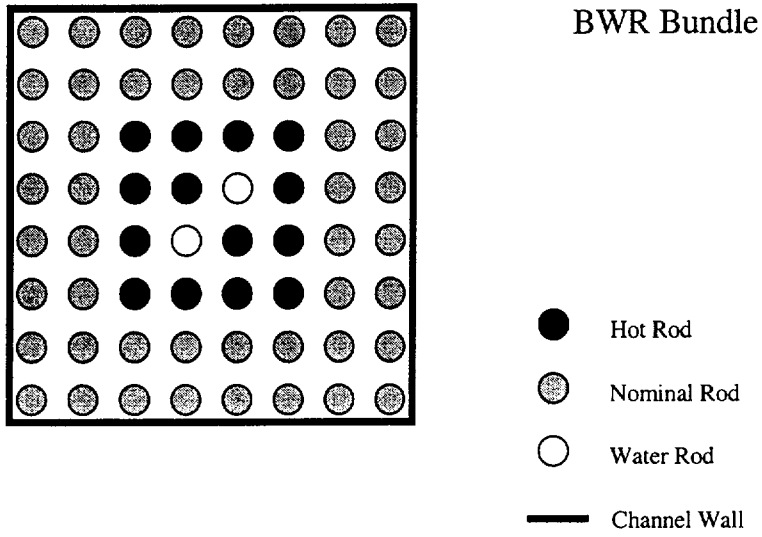
The test facility is actually a closer representation to a BWR fuel assembly which also has a Zircaloy channel or shroud surrounding the fuel rods. Therefore, for code modeling and validation purposes, the effect of the test housing must be modeled including the rod-to-rod and rod-to-housing radiation heat transfer. The housing effects must also be considered in the analysis of the test data to determine effect of radiation.

The housing had a less important effect on the fluid momentum equation since it only affected the hydraulic diameter and resulting fluid Reynolds number and friction factor such that the frictional component of the fluid pressure drop would be somewhat larger than a PWR fuel assembly. Since the majority of the pressure drop in the bundle is due to the spacer grid form losses, and the elevation head and since the prototypical grids are used in the test bundle, the hydraulic distortion is negligible.

There also can be some difference in the PWR/BWR Pi groups relative to the test due to the material differences as seen in Tables 6-14, 6-18 and 6-20. These effects are relatively small and can be accounted for in the analysis of the data.

Comparisons of the derived Pi groups for the test and a PWR and a BWR fuel assembly indicate that if prototypical fluid conditions are used in the tests, and the bundle geometry is retained, there is a very strong similarity between the bundle and the PWR and BWR fuel assemblies and the data should be applicable to either reactor fuel assembly type.

Figure 6-6: BWR Bundle Lumping Approach



6.9 References

- 6-1 Larson, T. K., et al, "Scaling Criteria and Assessment of Semi-scale Mod-3 Scaling for Small-Break Loss of Coolant Transients," EGG-SEMI-5121, (1980).
- 6-2 Ishii, M. and I. Kataoka, "Scaling Criteria for LWRs under Single-Phase and Two-Phase Natural Circulation," Proc. Joint ANS/NRC Meeting on Basic Thermal-Hydraulic Mechanisms in LWR Analysis, NUREG/CP-0043, Bethesda, Md (1982).
- 6-3 Zuber, N., "An Integrated Structure and Scaling Methodology for Severe Accident Analysis, Appendix D, A Hierarchical Two-Tiered Scaling Analysis", NUREG/CR-5809, (1991).
- 6-4 Wulff, W., "Scaling of Thermal Hydraulic Systems," Nuclear Engr. and Design, Vol 163, pgs. 359-395, (1996).
- 6-5 Zuber, N., "Presentation at March 28, 1997 ACRS Thermal Hydraulic Phenomena Subcommittee Meeting, Rockville, Md.
- 6-6 Reyes, J. R., Hochreiter, L. E. and L. Lau, "AP600 Low Pressure Integral systems Test at Oregon State University, Facility Scaling Report," WCAP-14270, (1995).
- 6-7 Brown, W. L., Hochreiter, L. E. and M. J. Loftus, "AP600 Scaling and PIRT Closure Report", WCAP-14727, (1997).
- 6-8 Lee, N., Wong, S., Yeh, H.C. and L. E. Hochreiter, "PWR FLECHT-SEASET Unblocked Bundle Forced and Gravity Reflood Task Data Evaluation and Analysis Report," NUREG/CR-2256 (1981).
- 6-9 Mohr, C. L. et al., "Prototypic Thermal-Hydraulic Experiment in NRU to simulate Loss-of-Coolant Accidents," NUREG/CR-1882 (1981).
- 6-10 Kreith, F. and M. S. Bohn, "Principles of Heat Transfer," Fourth Edition, Harper and Row Publishers, New York, (1986).
- 6-11 Evans, D.R., "The MOXY Core Heat Transfer Program: View Factor Model Improvements," RE-E-77-114, (1977).
- 6-12 Collier, J. G. and J. R. Thome, "Convective Boiling and Condensation," Oxford Science Publications, Oxford, (1994)
- 6-13 "An Integrated Structure and Scaling Methodology for Severe Accident Technical Issue Resolution," NRC Research, NUREG/CR - 5809 (Nov 1991).

6-14 Lewis, E. E., "Nuclear Power Reactor Safety," John Wiley & Sons, New York, (1977)

6.10 Nomenclature

A	area, m ²
Bi	Biot number (dimensionless)
c	specific heat, J/kg-K
D	diameter, m
e	specific internal energy, J/kg
f	friction factor
Fo	Fourier number (dimensionless)
g	acceleration due to gravity, m/s ²
g _c	gravitational constant (32.17 lbf-ft/lbf-s ²)
h	enthalpy, J/kg
h	heat transfer coefficient, W/m ² -K
J	radiosity, W/m ²
k	thermal conductivity, W/m-K
K	loss coefficient
L	length, m
m	number of grids in two phase region (Eq. 6-78)
n	number of grids in single phase region (Eq. 6-78)
Nu	Nusselt number (dimensionless)
p	rod pitch, m
P	pressure, N/m ²
Q	heat energy, W
R	radius, m
R	resistance (used in radiation network) (Eq. 6-102)
Re	Reynolds number (dimensionless)
t	time, sec
T	temperature, K
u	velocity, m/s
V	volume, m ³
W	mass flow rate, kg/s
z	elevation, m

Subscripts:

B	bundle
c	cladding
ci	cladding inside surface
co	cladding outside surface
cr	cold rod

c	convection (Usually with heat transfer coefficient)
CL	centerline
d	drops
dcht	direct contact heat transfer
DP	decay power
DR	dead rods
DR/d	dead rods to drops
DR/v	dead rods to vapor
e	exit
f	fluid
f	fuel
FB	film boiling
g	grid
gap	gap in the nuclear fuel rod
g/d	grid to drops
g/v	grid to vapor
hr	hot rod
H	housing
H/d	housing to drops
H/v	housing to vapor
i	reference case
i	inlet
I	Interfacial
<i>l</i>	liquid
lw	liquid contact
m	mixture
min	minimum
max	maximum
p	constant pressure
q	quench
r	rod
r/d	rod to drops
r/v	rod to vapor
s	surface
s	superheated
sat	saturated
t	test
T	total
v	vapor
v/d	vapor to drops
1ϕ	single phase
2ϕ	two phase

Greek Symbols:

α	void fraction
α	thermal diffusivity
μ	kinematic viscosity
Π	non dimensional 'pi' group
ρ	density
τ	time constant
Δ	increment

Superscripts:

'	per unit length
"	per unit volume
*	non dimensional variable
-	average
$\overline{\phi}_{fo}^2$	two phase flow multiplier
R_f	total frictional and form resistance
E_b	black body emissive power

7. SECOND TIER SCALING FOR THE ROD BUNDLE HEAT TRANSFER TEST FACILITY.

7.1 Introduction

Following the two-tier scaling methodology approach, Section 6 examined the "Top Down" scaling of the Rod Bundle Heat Transfer (RBHT) test facility relative to a PWR fuel assembly as well as a BWR fuel assembly. The individual Pi groups were calculated from the normalized conservation equations for the test facility, a PWR fuel assembly and a BWR fuel assembly. The calculations indicated which terms in the conservation equations were dominant for each configuration. The ratio of the Pi group calculations for the test and either the PWR or BWR fuel assembly indicated where the test facility had possible scaling distortions. The distortions were larger for the representation of the PWR fuel assembly by the RBHT test facility as compared to a BWR fuel assembly since there is no fuel assembly channel in the PWR fuel assembly, as compared to the test facility, while the BWR fuel assembly contains a fuel channel.

The top down scaling analysis indicated three areas where scaling distortion could exist in the RBHT test facility relative to a PWR or BWR fuel assembly. They are:

1. The presence of the housing which can act as a radiation and convection heat sink for the fluid and heater rods, as well as a heat source to the fluid as the housing quenches. The housing also changes the hydraulic diameter of the outer subchannels slightly such that there is lower flow in the outer subchannels, and correspondingly higher flow in the center of the bundle. However, this effect is small.
2. The material differences between the electrical heater rods and the nuclear rods which include a gap between the fuel pellet and the cladding
3. The material differences in the cladding which can affect the T_{\min} value and hence the quenching rate of the heater rods verses nuclear rods. Also included in this difference are the local effects of the surface, including roughness and oxide layer.

The bottom-up scaling effort has been performed specifically to examine these differences so that identified distortions can be assessed and methods found to account for or minimize their effects in the testing, data reduction, and data analysis. In the bottom-up scaling approach, analysis was performed to determine the radiation heat transfer effects of the test section housing relative to an infinite size rod bundle. These calculations would tend to over-emphasize the distortion of the test relative to a PWR fuel assembly. The BWR fuel assembly channel is similar to that of the RBHT facility so the distortion is less.

Calculations were also performed modeling a fuel rod, with its properties and the fuel-pellet gap as well as the electrical heater rod, to determine the heat released at quench as well as the stored energy effects and maximum temperatures and radial temperature distributions.

The differences in cladding material on the value of T_{\min} were assessed by comparing Inconel and Zircaloy cladding quench data from different tests. These comparisons indicated that Zircaloy quenches at a higher temperature relative to stainless steel or Inconel cladding.

The analysis and data comparisons for each of the identified areas of distortion are given in the remainder of this Section.

7.2 Housing effects and studies

7.2.1 Introduction

One of the main distortions of the RBHT facility compared to a PWR fuel assembly is the presence of the housing, which represents a heat sink for radiative heat transfer from the rods. The housing can also be a heat source for the fluid later into the transient because of the release of its stored energy during the quench time period.

To address housing effects in more detail, a single rod-to-rod, rod-to-housing model based on the MOXY computer⁽⁷⁻¹⁾ program was developed. MOXY was used to calculate the view factors matrix while a new program was written, called BUNDLE, to calculate the combined conduction-convection-radiation heat transfer in a cross section of the rod bundle. The BUNDLE program considers a cross section with each rod simulated individually, as well as the housing.

The VUEFAC subroutine was extracted from the MOXY computer program and included in BUNDLE to calculate the view factors matrix. The program calculates the temperature field in the bundle cross section during the reflood transient. The model solves thermal conduction in the rods and the housing, convection heat transfer to the fluid and radiative heat transfer among the rods and the housing surfaces. Convection to the fluid is simulated by assigning the time history of the heat transfer coefficient estimated from the FLECHT-SEASET Run 31504 test data⁽⁷⁻²⁾, as shown in Figure 7-1. In addition when the temperature in hottest rod falls below T_{\min} , the heat transfer coefficient is set to a very large value $5.678 \text{ kW/m}^2\text{K}$ ($1000 \text{ Btu/hr-ft}^2\text{-F}$) to force all the structures to quench at that time.

The radiative heat transfer to the droplets and to the vapor is neglected in the BUNDLE program while fluid is assumed transparent to the radiation. The thermal radiation heat transfer between the surfaces and the fluid (steam and droplets) is considered in the simplified lumped parameter approach using the RADNET computer program described in Section 6.4.4. More details of the model as well as the computer program list can be found in Appendices C.1 and C.2. The base case was a 7×7 bundle with four zero power (dummy) rods in the corner of the array. The other parameters are given in Table 7-1.

Table 7.1 Input data

rod power (kW/rod)	5.0 kW/rod
power radial distribution	uniform
wall surface emissivity	0.8
bundle heat losses (h_{out}) [btu / hr ft ² F]	0.0 (0)
fluid convection heat transfer coefficient (h_{in})	see Figure 7-1
initial temperature dummy rods [F]	450.0 (232.22°C)
initial temperature power rods [F]	1600.0 (871.11°C)
initial (pre-heating) temperature [F]	450.0 (232.22°C)
fluid temperature [F]	268.0 (T_{sat}) (147.5°C)

The heat transfer coefficient at the inside surface of the housing is assumed equal to the convective heat transfer coefficient used for the heater rods and is based on FLETCH-SEASET Test data.

7.2.2 Results

Figure 7-2 shows the clad temperature of the center rod, the inner 3x3 and 5x5 array averages, the housing and cold (dummy) rods surface temperature. The PCT temperature is reached at about 50 seconds while the maximum housing temperature is reached later in time at about 200 seconds. At about 250 seconds the clad temperature at the hottest rod falls below T_{min} and all structures are quenched. Note that the quenching time of the housing is larger than that for the other structures. Figures 7-3 show the heat rate (W/m) release from the rods to the housing and the heat released from the housing to the fluid. The heat transfer rate is very high when the housing quenches. Figure 7-4 shows the same results with an expanded y-axis. The maximum heat transfer rate from the rods to the housing is about 25% of the heat generated in the bundle. The housing releases energy to the fluid early in transient by convection to the steam and later to the mixture during the quench time.

The heat transfer from the rods to the fluid, particularly from the outer rods, can be a two-step process in which the energy first passes to the housing via radiation and then to the fluid by convection. This is described by Figure 7-4 which shows that the radiative heat rate from the rods to the housing reaches its maximum value of 24 kW/m at about 35 seconds, then decreases almost linearly to 2 kW/m at about 245 seconds, when quench occurs. In the same time period, the convective heat rate from the housing to the fluid rise from nearly 0 to about 15 kW/m. Then the remaining energy stored in the housing is released during the quench period which last about 20-30 seconds. During quenching, the convective heat rate from the housing to the fluid increases to 400 kW/m.

Note that the temperature gradient which develops radially across the bundle as a consequence of the presence of the housing is overestimated by these calculations because of the assumptions

used. In reality, thermal radiation from the rods to the fluid (droplets and vapor) will tend to reduce the temperature of the inner rods, therefore, the heat transfer to the external rods and the housing will be lower than the calculated value. Another effect is the convective heat transfer coefficient, which is assumed uniform in the calculation. In reality, the convective heat transfer coefficient will be higher in the center region of the bundle. Again, this effect will reduce the temperature gradient across the bundle.

Quasi steady-state calculations were carried out for the FLECHT 15x15 bundle using a radiative network ⁽⁷⁻³⁾ approach similar to the one described in Section 6. In this case the radiative heat transfer from the inner rods to the housing was estimated to be 10% to 20% of the convective heat transfer depending on the flow conditions. Note that the FLECHT bundle was larger than the 7x7 RBHT bundle.

Sensitivity studies were performed to the base case (Table 7-1) to optimize the facility designing by reducing the scaling bias where possible, as follows:

- a) bundle size (3x3, 5x5, 7x7,.....,17x17,infinite)
- b) housing thickness
- c) housing pre-heating
- d) surfaces emissivity
- e) radial power distribution
- f) dummy rods (cold-surfaces) contribution

Results are summarized in the following and presented in Figures 7-5 through 7-10.

a) Bundle size

The calculation of the clad temperature for an infinite array with a constant radial power distribution results in a rod-to-rod temperature gradient which is zero since radiative heat transfer does not take place and the clad temperature is determined only by the fluid convection. An indication of the radiative heat transfer contribution for a finite array is the difference between the average clad temperature in the central rods sub-array as calculated for a finite size bundle and the same value calculated for an infinite size bundle. The selected sub-array is the inner 3x3 rods and the temperature drop defined is $\Delta T_{\infty} = T_{\infty} - T_{3 \times 3}$. This temperature difference represents the facility distortion when compared to the temperature expected when the same boundary condition are applied in a real PWR core which is essentially an infinite array.

Figure 7-5 shows the value of ΔT_{∞} for different bundle sizes (5x5, 7x7, 9x9 and 11x11). The time at which the quench is occurring is earlier in the finite bundle respect to the infinite bundle case. As a consequence, the significant clad temperature drop which is experience during the quench is earlier than in the small bundle size. This effect is indicated in Figure 7-5, which shows the difference between the clad temperature in the hypothetical infinite bundle and the clad temperature in the finite size bundle. Figure 7-5 shows that the quench time is anticipated of about 17 seconds in 5x5 bundle, of about 7-8 seconds in the 7x7 bundle and of smaller value for larger bundle sizes.

Before the quenching, the maximum temperature distortion is reached between 150 and 200 seconds into the transient, depending on the bundle size. For the 7x7 bundle, a maximum value of 250°F (138°C) is predicted, the maximum distortion decreases to 150°F (83°C) for a 9x9 bundle and to 100°F (55.6°C) for a 11x11 bundle. For the 5x5 bundle size the maximum temperature distortion is up to 400°F (222.4°C) which is much larger than the 250°F (138°C) maximum temperature distortion experienced in a 7x7 bundle. In conclusion when compared to the infinite bundle array the 7x7 bundle is good compromise when low costs and low scaling biases are both a concern in the facility design. A Large bundle will provide a more prototypic behavior with a reduced temperature bias but the costs addition due to the additional rods increases dramatically.

b) Housing thickness

The housing is both a heat sink and a heat source during the reflood transient, and represents a bias which should be minimized by reducing its thickness to a minimum. The housing is a heat sink for the thermal radiation from the external rods and is an heat source to the fluid as the quench front approaches, as seen in Figure 7-4. The housing heat release is very large during quenching. A ¼ inches (6.35 mm) thick housing was chosen to provide enough strength for the facility operation. To quantify the effect of the housing thermal inertia, two sensitivity cases were run with $\frac{3}{16}$ and ¼ inches (6.35 – 4.76 mm) thick housing. Results (Figure 7-6) show that in this range the solution is insensitive to the housing thickness. In conclusion the variation of the housing thermal inertia is negligible in the thickness range of interest.

c) Housing preheating

To reduce the rod temperature drop introduced by the presence of the housing, the housing could be pre-heated before the reflood begins to reduce the radiative heat transfer between the rods and the housing during the early part of the reflood. An optimum preheating temperature value will exist. A high temperature reduces the radiative transfer between rods and housing; however, it increases the metal heat release to the fluid during quenching. The base case considered an initial housing temperature of 450 °F (250°C) while the sensitivity case assumed an initial housing temperature of 1000°F (556°C). Results are shown in Figure 7-7: the temperature drop ΔT_{∞} for the center 3x3 array is lower for higher pre-heating temperature, 1000°F (556°C), but the difference between the two cases is less than 40°F, indicating that initial heating has a weak effect.

d) Surface emissivity

Some uncertainty exists in surface emissivity, which is a function of surface conditions (roughness, oxidation etc.). Emissivity, in turn, affects radiative heat transfer. For oxidized Inconel-600 the literature provides emissivity values ranging from 0.7 and 0.9. A sensitivity analysis was performed to address this effect. Figure 7-8 shows that the temperature uncertainty introduced by the emissivity uncertainty is less than 20°F.

e) Axial power distribution

The base case considers a uniform radial profile with zero power in the four corner rods. The possibility of increasing the peripheral rods to provide a "shield" to rod-to-housing heat transfer was investigated. A 20% increase in power was applied to the external rods while keeping the same (5.0 kW/rod) power in the interior rods (i.e. the total power in the bundle increases by about 9%). Figure 7-9 shows that the maximum value of ΔT_{∞} decreases of about 20°F.

f) Effect of the corner dummy rods

The effect of the dummy rods in the four corners of the bundle is shown in Figure 7-10. The calculation is based on the same rod power (5.0 kW/rod) and the total power of the bundle is the same of the previous sensitivity case (9% greater than the base case). The effect of the dummy rods is to decrease ΔT_{∞} by about 10°F. This is a secondary effect to the radiative heat transfer from the inner rods in the bundle. The conclusion from the six sensitivity studies is that the parameter of most importance is bundle size. A large gain (~50%) occurs in increasing the bundle size from 5x5 to 7x7. Further gains are made by increasing the bundle size to 11x11, however, the facility cost would increase accordingly by approximately a factor of four. The other parametric variations are small by comparison.

7.3 Material differences

7.3.1 Introduction

Another issue which arose from the scaling analysis is the rod material differences. The electrical heater rods use Inconel-600 instead of Zircaloy for the clad and Boron Nitride instead of Uranium Dioxide. The electric power is generated only in an annulus area inside the rod where the heating element, Monel K-500 is located. Another difference is the gap conductance which is assumed to be 5679 W/m²K (1000 Btu/hr-ft²-F) for a nuclear rod and 28385 W/m²K (5000 Btu/hr-ft²-F) for the electrical rod.

A detailed analysis was performed to quantify the transient temperature response distortion of an electrical rod when compared with a nuclear rod.

The BUNDLE computer program was used to simulate a transient conduction problem for a single rod. The radiation heat transfer is turned off for this case. The transient was basically a step change in the convection heat transfer coefficient while keeping constant rod power and fluid temperature. The step change was applied after a steady-state was reached where the surface temperature is assumed to be at T_{\min} . This transient can be a simplified view of the quench process. Consistently with section 6, T_{\min} was set to 550°C (1022°F). The initial convective heat transfer coefficient is calculated assuming a steady state condition where the rod surface temperature is exactly at T_{\min} . The conditions of the transient are given in Table 7-2.

Table 7-2: Input data

Rod power (kW/rod)	0.7 kW/ft
Fluid Temperature	131 C (267°F)
Initial H.T.C.	183.4 W/m ² K (32.3 Btu/hr-ft ² -F)
Final H.T.C.	5679 W/m ² K (1000 Btu/hr-ft ² -F)
Initial T _{clad} = T _{min}	550 C (1022°F)
Conductivity of UO ₂	2.4 W/mK (1.4 Btu/hr-ft-F)
Conductivity of BN	85.9 W/mK (49.6 Btu/hr-ft-F)
Gap Conductance Nuclear	5679 W/m ² K (1000 Btu/hr-ft ² -F)
Gap Conductance Electrical	28385 W/m ² K (5000 Btu/hr-ft ² -F)

7.3.2 Rod comparison

Figure 7-11 shows the temperature profile at the initial steady state for both the heater rod and the nuclear rod with a clad surface temperature of 550°C (1022°F). The difference in the profiles is because of conductivity: UO₂ is about a factor 20 lower than the BN/Monel conductivity; therefore, the nuclear rod has a higher centerline temperature than the electric rod for the same clad surface temperature.

An additional contribution to the above difference is the gap conductance which larger for the heater rod by approximately a factor 5. This effect is shown in Figure 7-12.

The top-down analysis indicated that the stored energy in the fuel region is comparable between the nuclear rod and heater rod. On the other hand, more energy is stored in the Inconel cladding than Zircaloy cladding so that the total amount of stored energy is somewhat larger for the heater rod. The larger amount of energy which resides in the cladding of the heater rod is released quickly during quenching, as shown in Figure 7-13. Figure 7-14 shows the amount of stored energy released during the transient. This value was calculated integrating over time the power released detracted by the power generated as:

$$E_{quench} = \int_0^t (q(t) - q_o) dt$$

where

$q(t)$ = power released to the fluid

q_o = rod power (0.7 kw/ft)

t_o = initiation of quench

Figure 7-14 shows that the electrical rod releases a larger amount of energy more quickly. The time constant for the energy release is consistent with that calculated with a simple double-lumped approach, described in Section 6.

7.4 Surface properties differences

The surface properties which can affect the reflood behavior are the wall surface emissivity and the factors that determine minimum film boiling temperature T_{min} .

The Zircaloy surface emissivity can be slightly higher than the Inconel-600 even though the uncertainty in its real value is sometimes larger than the difference between the two materials. The wall emissivity depends on many factors such as temperature and oxidation of the surface. The effect of the wall emissivity on the rod-to-rod and rod-to-housing radiative heat transfer was addressed by the sensitivity analysis presented in Section 7.2.

Figure 7-15 shows the distribution ⁽⁷⁻⁶⁾ of experimental rewet temperatures based on Westinghouse G-1 and G-2 blowdown experiments ^(7-7, 7-8). A mean value of 536°C (998°F) was found. Prototypic thermal hydraulic experiments ⁽⁷⁻⁹⁾ for Zircaloy cladding indicate an average value of 575°C (1068°F). Zircaloy will quench at higher temperature than stainless steel or Inconel.

7.5 Scaling Conclusions

The three areas where scaling distortion could exist between the RBHT test facility and a PWR or BWR fuel assembly were indicated during the first tier scaling analysis described in Section 6, namely . Section 7 presented the bottoms-up scaling analysis and addressed these distortions in more detail.

During the early part of reflood, housing acts as both a radiation and convection heat sink for the fluid and heater rods, whereas with the approach of the quench front, it acts as a heat source. The presence of the housing causes a radial temperature distribution across the bundle which in turn drives energy from the inner portion of the bundle to the housing. As a result, during the transient the temperature in the inner region of the RBHT bundle is lower than the temperature in an ideal case.

The effect of the housing is less important for a large bundle since the inner region is shielded by the outer region of the bundle. Sensitivity analyses were performed to quantify the housing distortion for different bundle sizes from 5x5 to 11x11 arrays. The distortion decreases significantly when the bundle size is increased from 5x5 to 7x7 while for further increases the distortion reduction is progressively less and less significant. A 7x7 bundle size is a reasonable compromise between cost and scaling distortion. For a 7x7 array, the maximum temperature distortion to the inner 3x3 rod array with respect to an infinite (no-housing) bundle is about 121 C (250 F).

Sensitivity studies were performed to evaluate the effects of housing thickness, housing initial temperature, emissivity, radial power distribution and dummy rods contribution. These were found to be of second order importance. Their effect on the temperature in the center region is 28°C (50°F) at most.

The material differences between the electrical heater rods and the nuclear rod, which also includes a gap between the fuel pellet and the cladding, is the second major facility distortion. The analysis shows that the quench time can be affected by material properties. The stored energy is 15% larger in the heater rod compared with the nuclear rod. The amount of energy in the fuel region is similar. The difference resides in the Inconel cladding of the heater rod. The conductivity of the "fuel" region of the electrical rod is 20 times higher than the nuclear rod. Therefore, if we assume the same heat transfer coefficient at the quench front, the stored energy is released more rapidly in the heater rod versus the nuclear rod. This introduces a bias in the experiments which must be determined. This bias will be lower than predicted by this simplified analysis. In fact if more energy is released to a given volume of liquid, the heat transfer coefficient will decrease and this will in turn reduce the heat release rate in the electric rod.

In addition differences of the cladding material on the value of T_{\min} were assessed by comparing Inconel and Zircaloy cladding quench data from different tests. These comparisons indicated that there is a difference. The Zircaloy cladding will quench at a higher temperature relative to stainless steel or Inconel cladding.

7-6 References

- 7-1 - Evans, D. R., "The MOXY Core Heat Transfer Program: View Factor Model Improvements", RE-E-77-114, February 1977.
- 7-2 - Lee, N., Wong, S., Yeh, H.C. and Hochreiter., L.E. - "PWR FLECHT-SEASET Unblocked Bundle, forced and gravity reflood task. Data evaluation and analysis report". - WCAP-9891, November 1981.
- 7-3 - Yao, S.C., Dodge, C. and Hochreiter, L.E., "A simple Method for Calculating Radiative Heat Transfer in Rod Bundles With Droplets and vapors as Absorbing Media" - (Technical Note), J. Heat Transfer 101, ASME, 736 (1979)
- 7-4 - Sun, K.H., et al., "Calculation of combined radiation and convection heat transfer in rod bundles under emergency cooling conditions", - J. Heat Transfer 98, ASME, 4141-420 (1976)
- 7-5 - Kreith, F. and Bohn, M.S. - "Principles of Heat Transfer (Fourth Edition)" - Harper & Row, Publishers Inc., New York, 1986.
- 7-6 - Zhang J., Bajorek S. M., Kemper R M., Hochreiter L. E., "WCOBRA-TRAC Analysis of ORNL High Flow Rod Bundle Film Boiling Tests", National Heat Transfer Conference, ANS-HTC- Vol. 10, Baltimore, Maryland (1997).
- 7-7 - Cunningham, J. P., et al., "ECCS Heat Transfer Experiments with Upper Head Injection," WCAP-8100, Vols 1 & 2, October 1974 and January 1975.
- 7-8- Andreycheck, T. S., et al., "Blowdown Experiments with Upper Head Injection in G-2 17x17 Rod Array Facility," WCAP-8582, Vols 1 & 2, Jan. 1976 and Aug. 1976.
- 7-9 - Mohr, C. L., at al., "Prototypic Thermal Hydraulic Experiments in NRU to simulate LOCA", NUREG-CR-1882.

Figure 7-1
Convective Heat Transfer Coefficient (FLECHT-SEASET Run 31504)

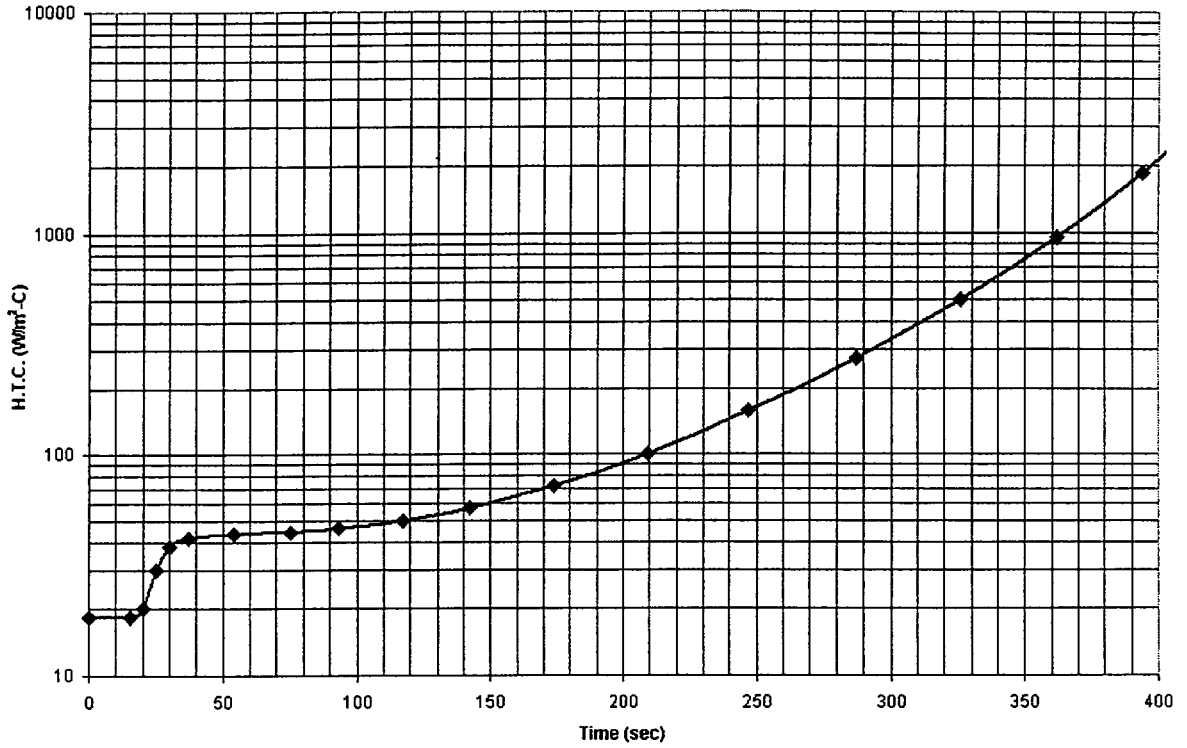


Figure 7-2
Wall surface temperature in the 7x7 bundle (base case)

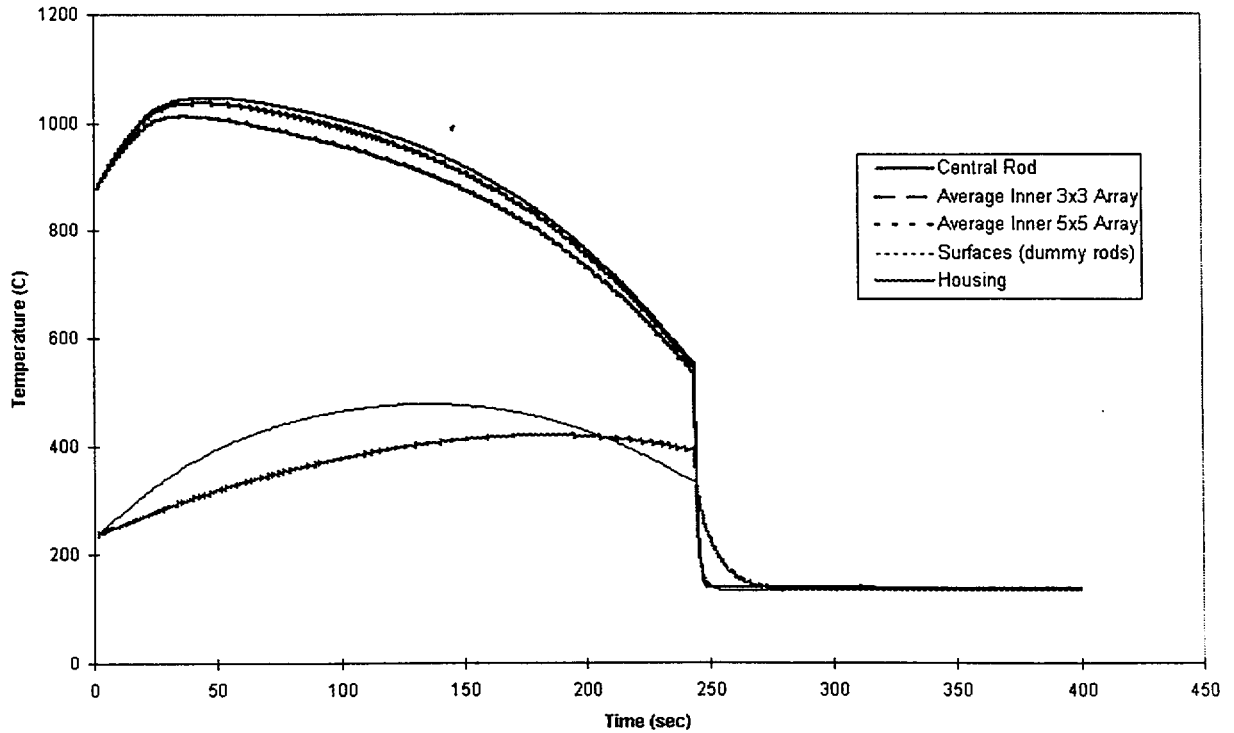


Figure 7-3
Heat rate to and from the housing in the 7x7 bundle (base case)
(Bundle Linear Power = 103000 W/m)

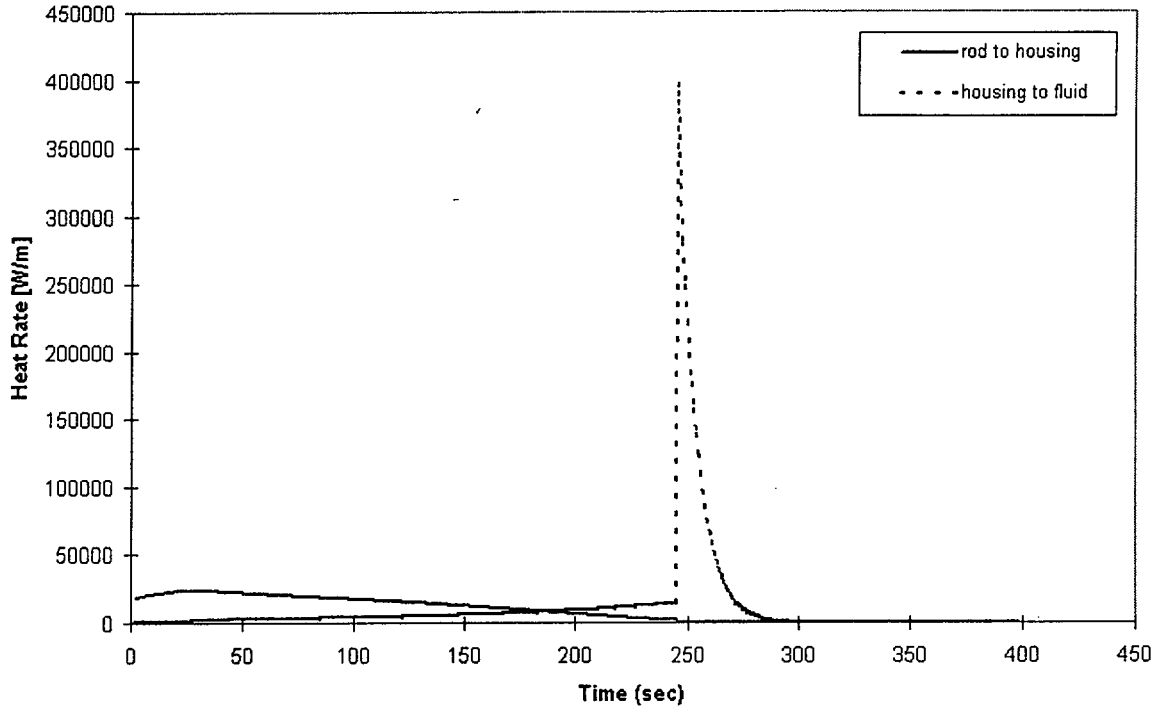


Figure 7-4
Heat rate to and from the housing in the 7x7 bundle (base case)
(Bundle Linear Power = 103000 W/m)

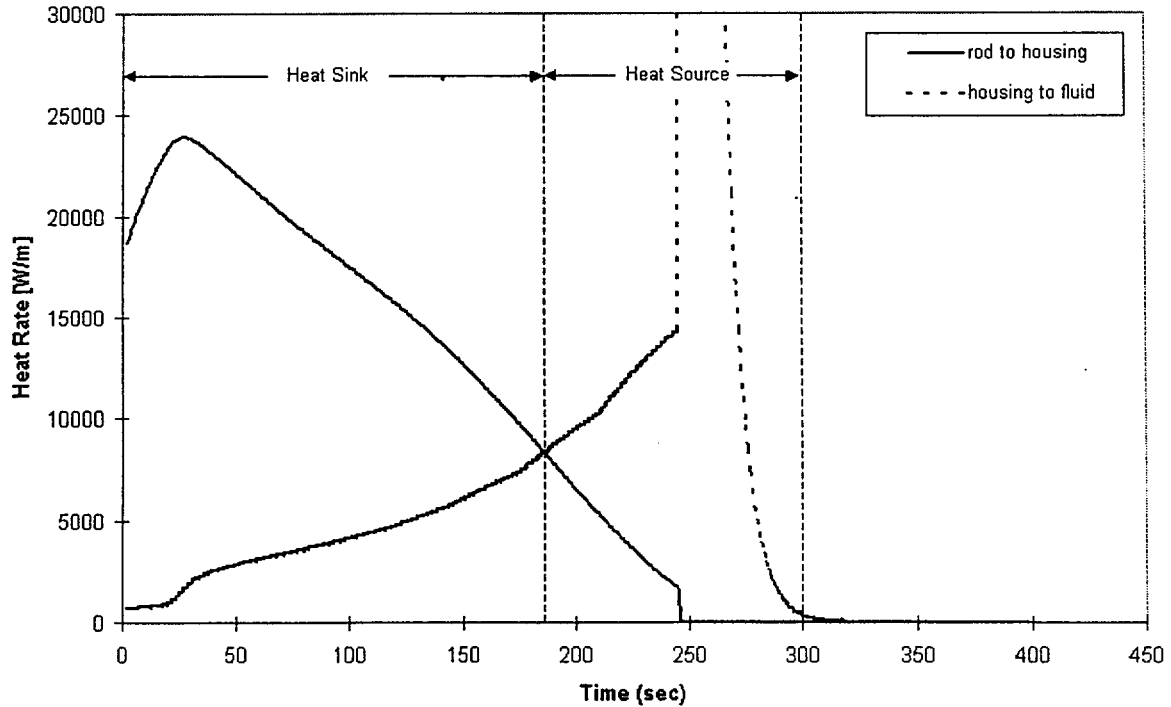


Figure 7-5
Clad temperature drop in the inner 3x3 array because of radiative heat transfer in a finite size bundle array

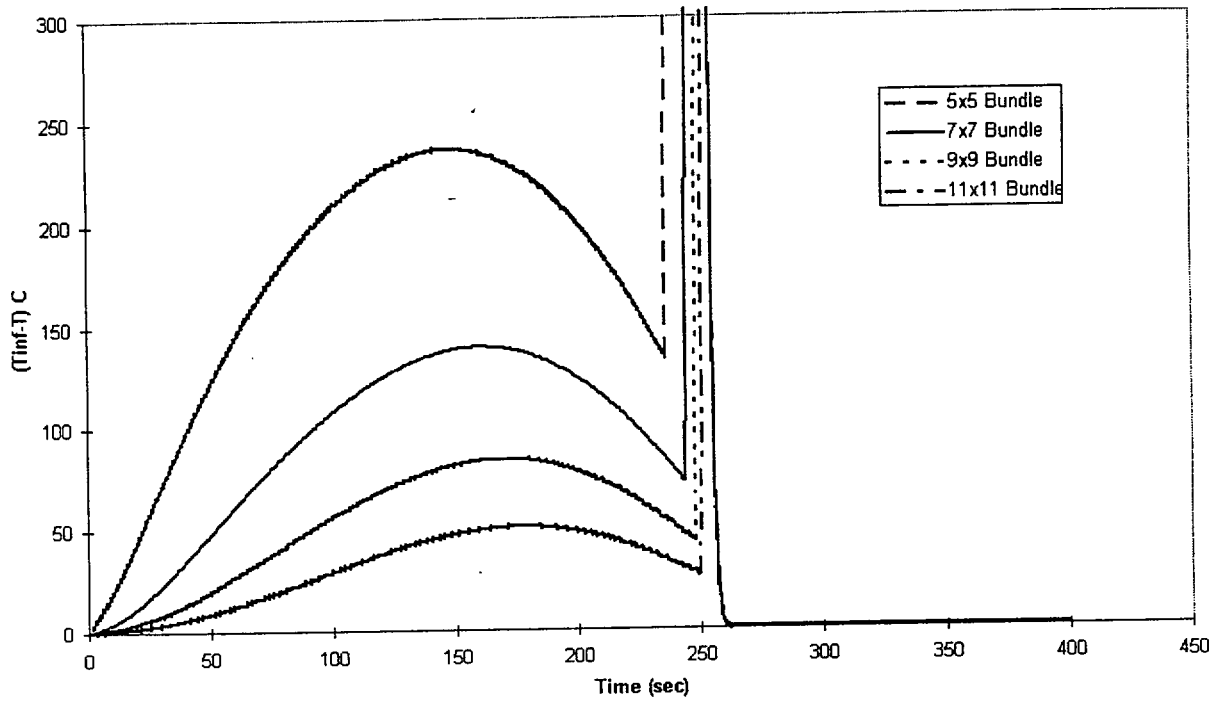


Figure 7-6
Inner 3x3 rod array clad temperature bias in RBHT bundle
Housing thickness sensitivity

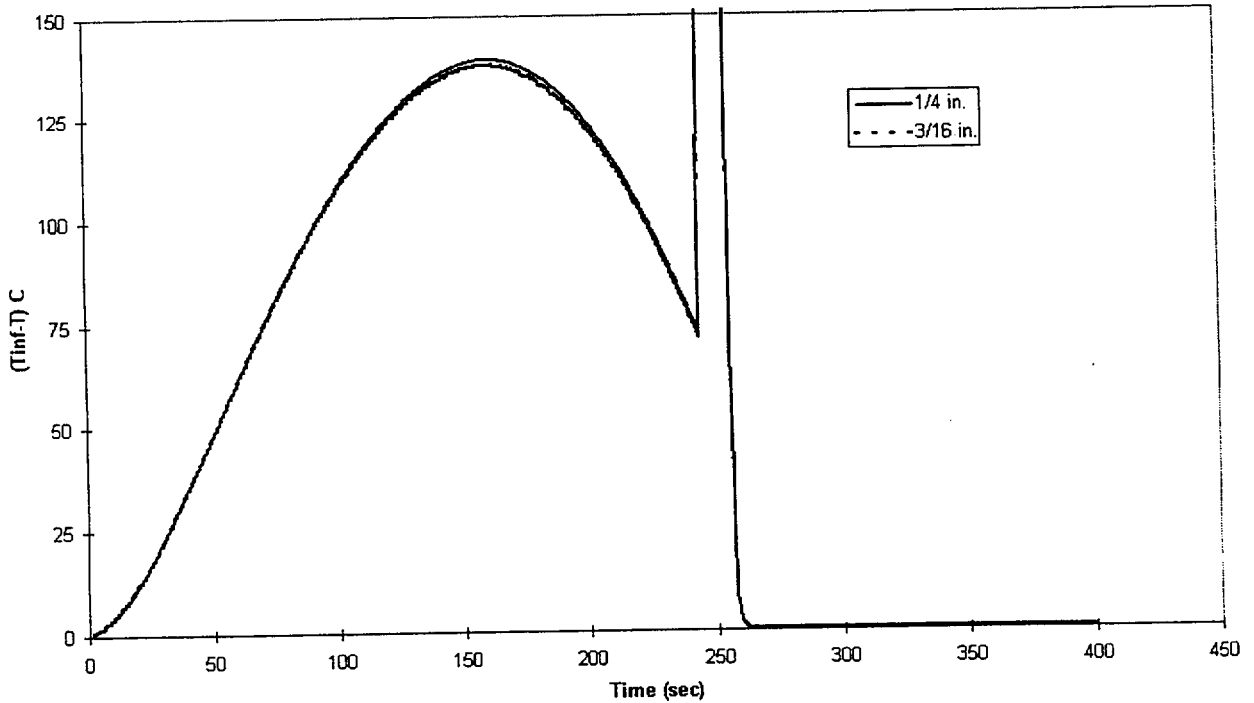


Figure 7-7
Inner 3x3 rod array clad temperature bias in RBHT bundle
Housing initial (pre-heating) temperature sensitivity

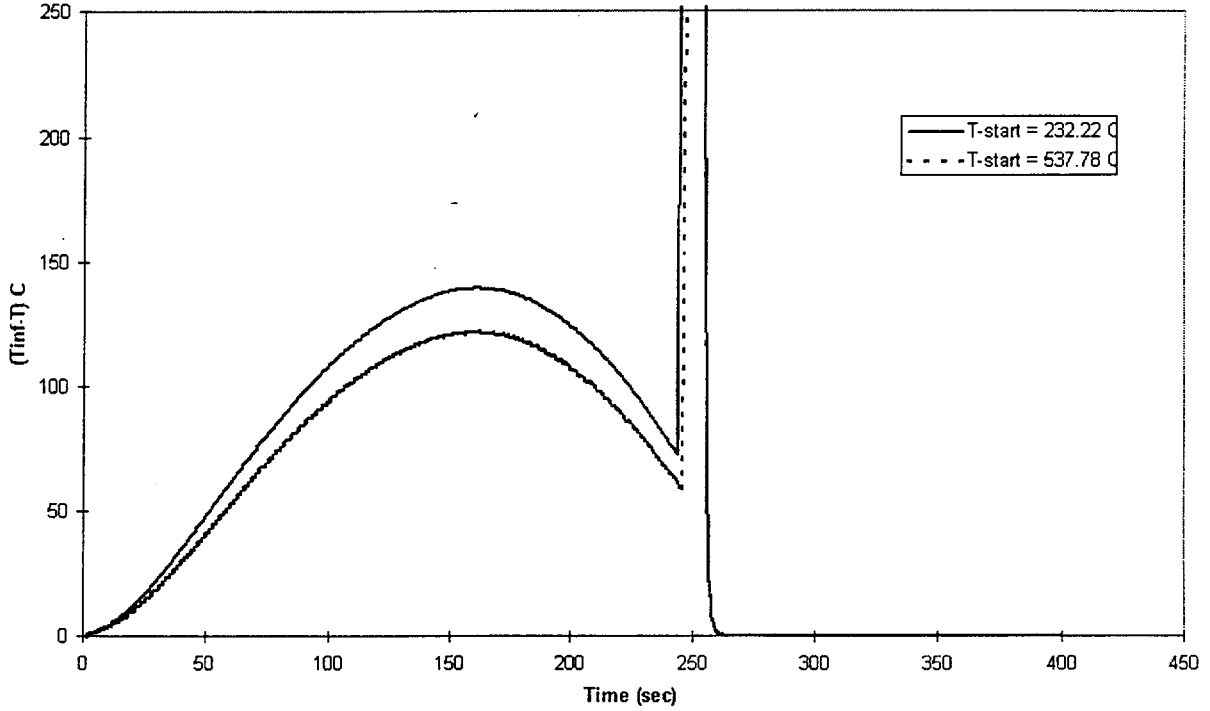


Figure 7-8
Inner 3x3 rod array clad temperature bias in RBHT bundle
Wall emissivity sensitivity

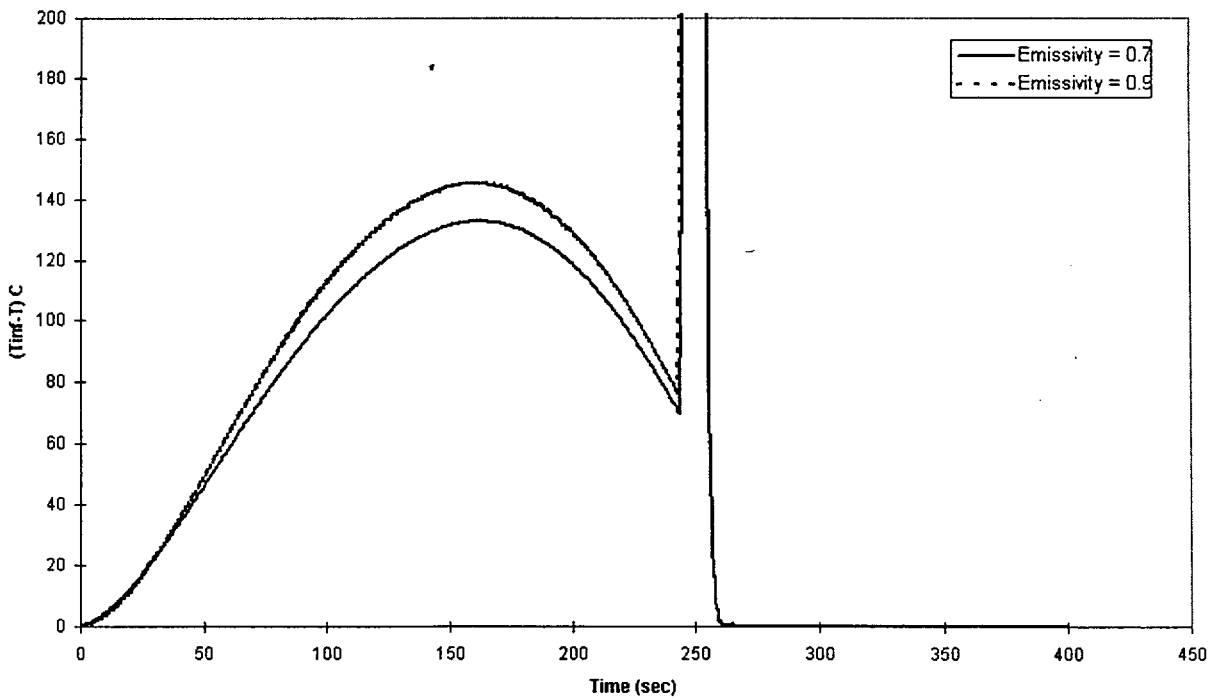


Figure 7-9
Inner 3x3 rod array clad temperature bias in RBHT bundle
Radial power distribution sensitivity

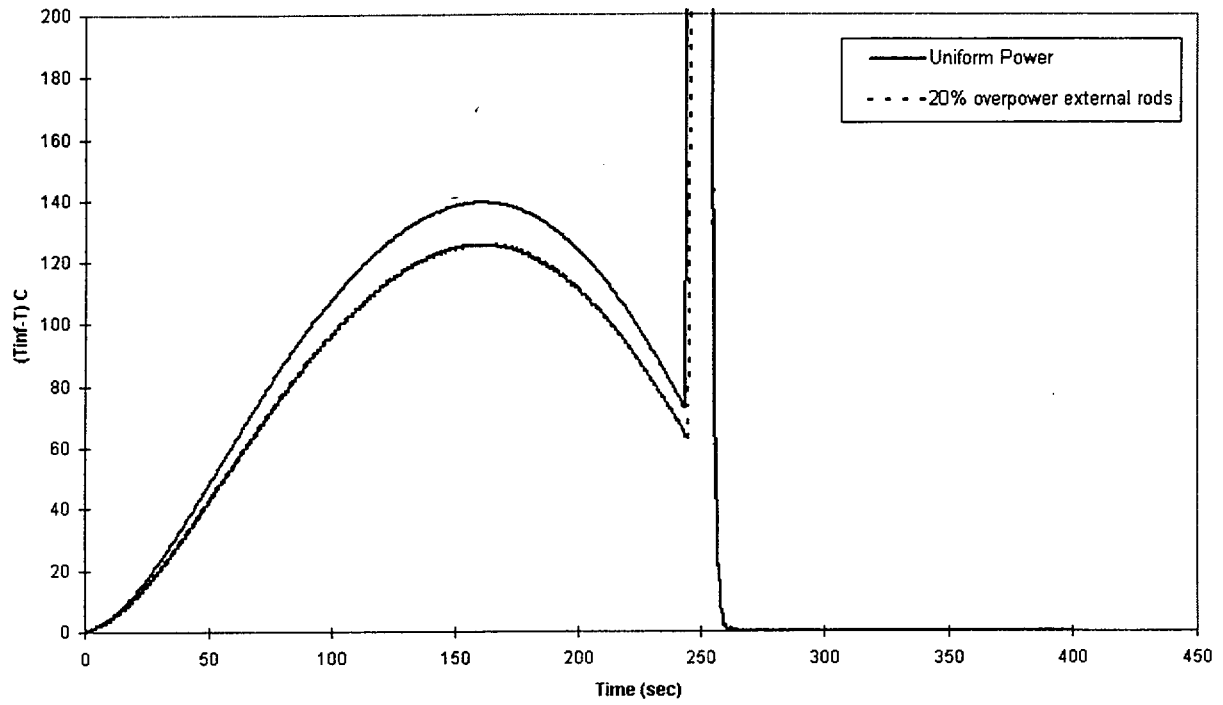


Figure 7-10
Inner 3x3 rod array clad temperature bias in RBHT bundle
Dummy rods effect

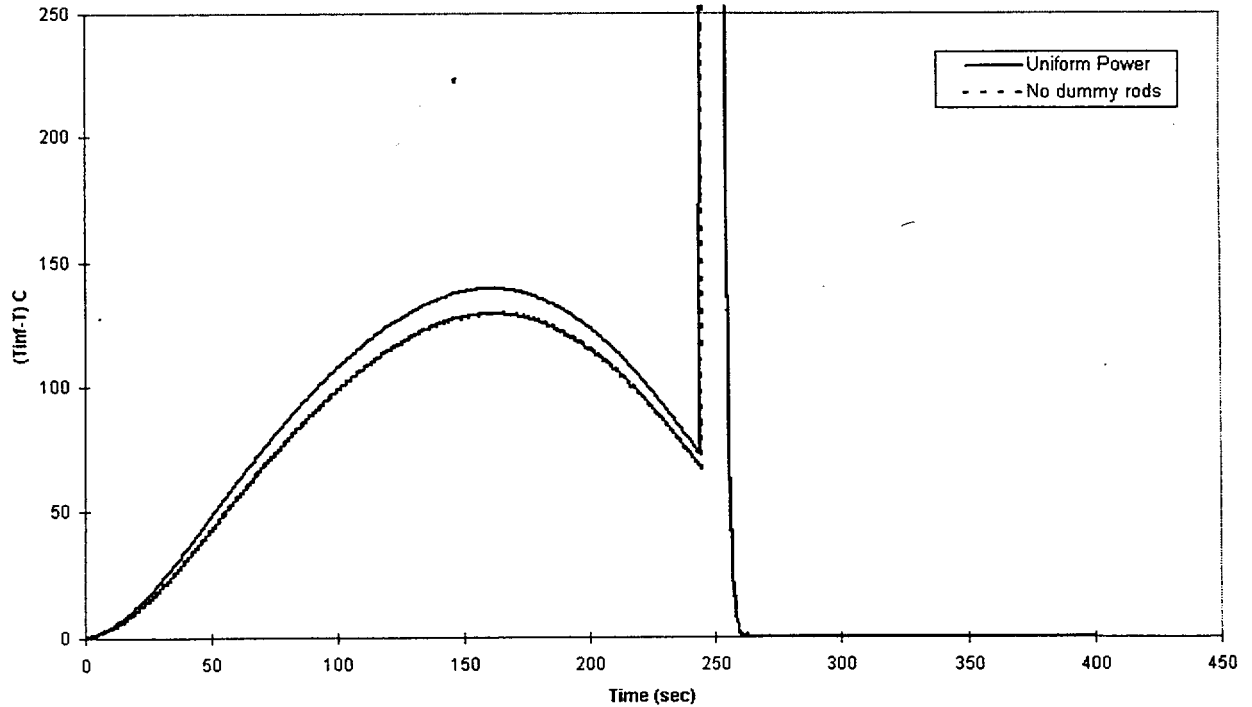


Figure 7-11
Steady-State Temperature Profile

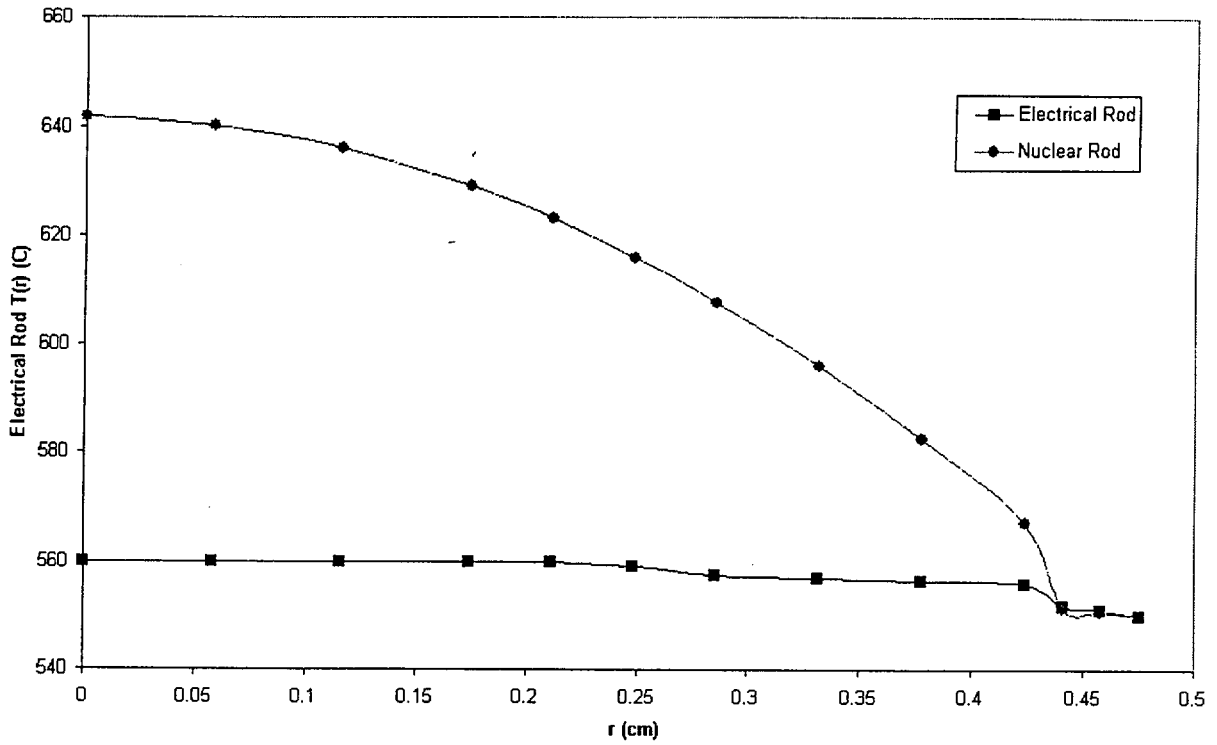


Figure 7-12
Electrical Rod Steady-State Temperature Profile Gap resistance sensitivity

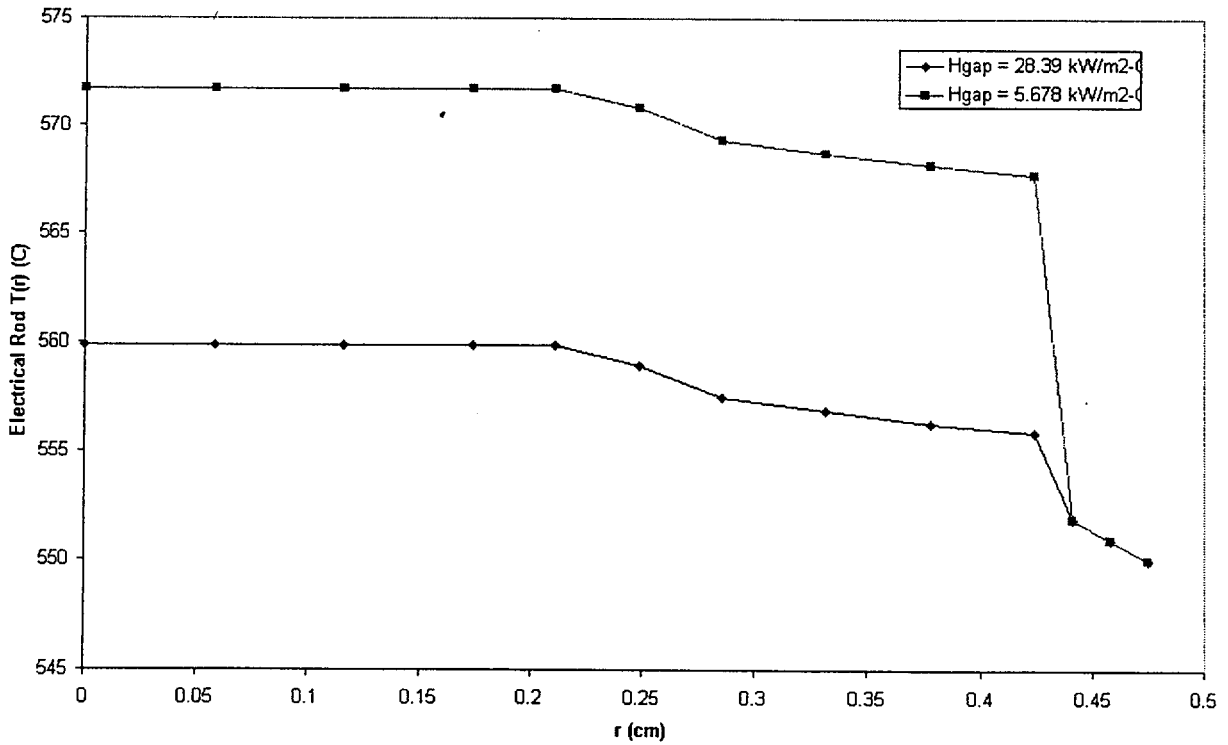


Figure 7-13
Rod Quenching

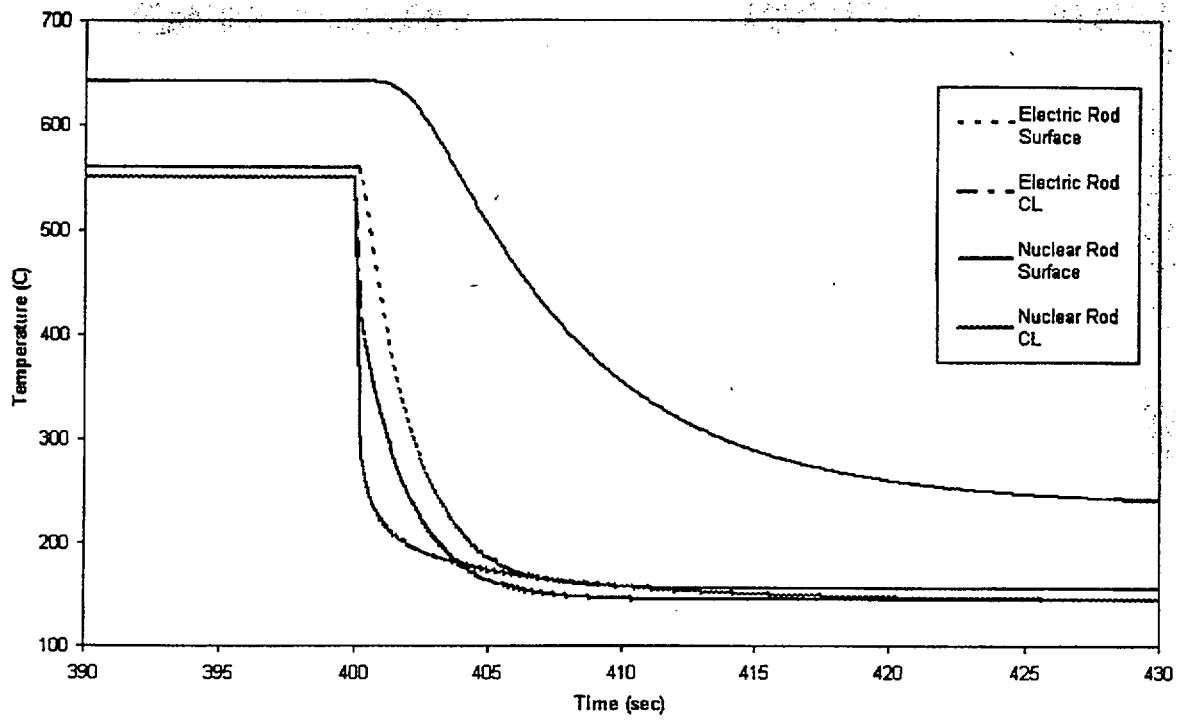


Figure 7-14
Rod Quench Energy Release

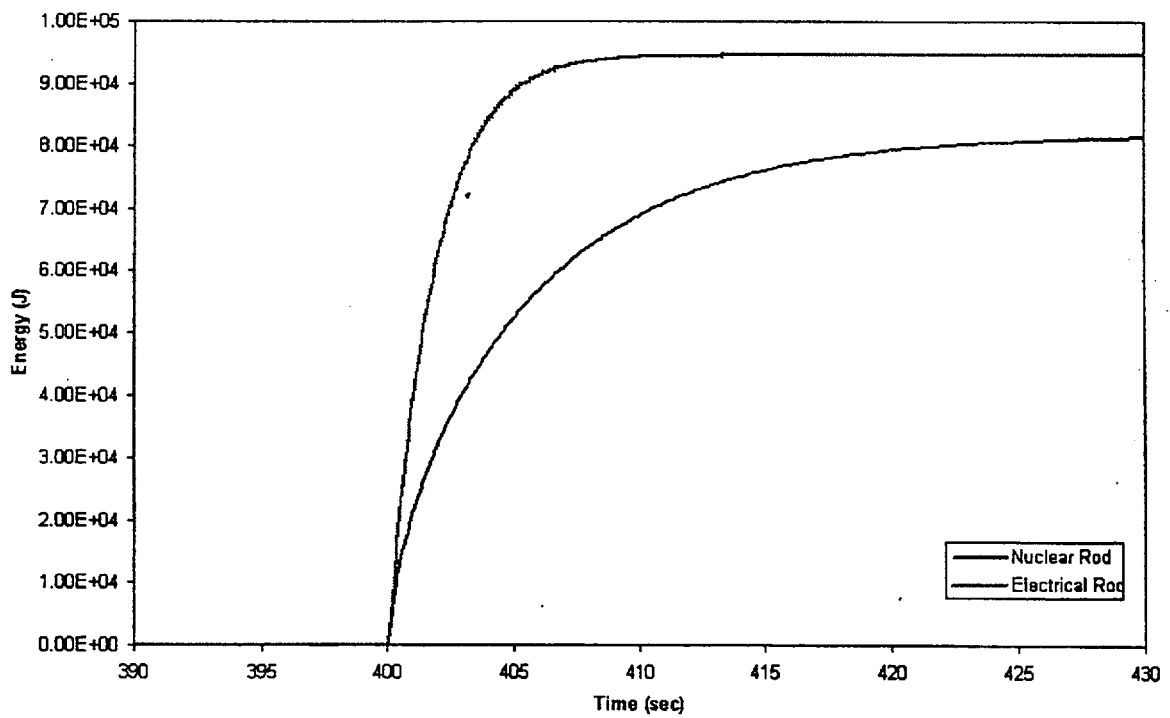


Figure 7-15
Distribution of Measured Rewet Temperatures During Westinghouse G-1 and G-2 Blowdown Rod Bundle Experiments

